

NAVAL POSTGRADUATE SCHOOL

Monterey, California

AD-A205 255



THESIS

MODELING THE BEHAVIOR OF THE
LINEARLY TAPERED SLOT ANTENNA

by

Thomas P. Kelly

December 1988

Thesis Advisor: Ramakrishna Janaswamy

Approved for public release; distribution is unlimited

DTIC
ELECTE
MAR 14 1989
S H D

10 3 14 028

UNCLASSIFIED

SECURITY CLASSIFICATION OF THIS PAGE

ADA205255

REPORT DOCUMENTATION PAGE				Form Approved OMB No. 0704-0188	
1a REPORT SECURITY CLASSIFICATION UNCLASSIFIED			1b RESTRICTIVE MARKINGS		
2a SECURITY CLASSIFICATION AUTHORITY			3 DISTRIBUTION AVAILABILITY OF REPORT Approved for public release; distribution is unlimited		
2b DECLASSIFICATION/DOWNGRADING SCHEDULE					
4 PERFORMING ORGANIZATION REPORT NUMBER(S)			5 MONITORING ORGANIZATION REPORT NUMBER(S)		
6a NAME OF PERFORMING ORGANIZATION Naval Postgraduate School		6b OFFICE SYMBOL (if applicable) 62	7a NAME OF MONITORING ORGANIZATION Naval Postgraduate School		
6c ADDRESS (City, State, and ZIP Code) Monterey, California 39943-5000			7b ADDRESS (City, State, and ZIP Code) Monterey, California 93943-5000		
8a NAME OF FUNDING SPONSORING ORGANIZATION		8b OFFICE SYMBOL (if applicable)	9 PROCUREMENT INSTRUMENT IDENTIFICATION NUMBER		
8c ADDRESS (City, State, and ZIP Code)			10 SOURCE OF FUNDING NUMBERS		
			PROGRAM ELEMENT NO	PROJECT NO	TASK NO
					WORK UNIT ACCESSION NO
11 TITLE (Include Security Classification) MODELING THE BEHAVIOR OF THE LINEARLY TAPERED SLOT ANTENNA					
12 PERSONAL AUTHOR(S) KELLY, Thomas P.					
13a TYPE OF REPORT Master's Thesis		13b TIME COVERED FROM _____ TO _____		14 DATE OF REPORT (Year, Month, Day) 1988 December	
15 PAGE COUNT 142					
16 SUPPLEMENTARY NOTES The views expressed in this thesis are those of the author and do not reflect the official policy or position of the Department of Defense or the US Government					
17 COSATI CODES			18 SUBJECT TERMS (Continue on reverse if necessary and identify by block number)		
FIELD	GROUP	SUB-GROUP	LTSA; Flare Angle; Substrate; Dielectrical;		
			Antenna; Planar Antenna; Radiation Pattern;		
			Moment Method; The Linearly Tapered Slot Antenna		
19 ABSTRACT (Continue on reverse if necessary and identify by block number) The Linearly Tapered Slot Antenna (LTSA) had been investigated and developed experimentally; its applications have primarily been based on empirical designs. An accurate theoretical model based on Moment Methods (MM) is developed here to study the radiation characteristics of the LTSA. Using the MM solutions to the reaction integral equation, this thesis presents an analysis to model and explain the LTSA behavior. The effects of variable design parameters on radiation patterns are studied. Discussion is augmented by relating predicted radiation patterns to calculated current distributions on the antenna surface. Conclusions are made regarding optimum designs for the LTSA. Relevant observations are made concerning the extensive computational tasks and the computer resources required for the MM model.					
20 DISTRIBUTION AVAILABILITY OF ABSTRACT <input checked="" type="checkbox"/> UNCLASSIFIED UNLIMITED <input type="checkbox"/> SAME AS RPT <input type="checkbox"/> DTIC USERS			21 ABSTRACT SECURITY CLASSIFICATION UNCLASSIFIED		
22a NAME OF RESPONSIBLE INDIVIDUAL JANASWAMY, R.			22b TELEPHONE (Include Area Code) 408-646-3217		22c OFFICE SYMBOL 62Js

DD Form 1473, JUN 86

Previous editions are obsolete

S/N 0102-LF-014-0005

SECURITY CLASSIFICATION OF THIS PAGE

UNCLASSIFIED

Approved for public release; distribution is unlimited

Modeling the Behavior of the
Linearly Tapered Slot Antenna

by

Thomas P. Kelly
Major, United States Army
A.A.S., Delaware Technical and Community College, 1971
B.S., United States Military Academy, 1976

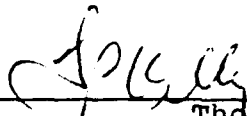
Submitted in partial fulfillment of the
requirements for the degree of

MASTER OF SCIENCE IN ELECTRICAL ENGINEERING

from the

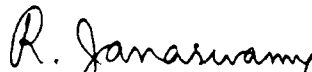
NAVAL POSTGRADUATE SCHOOL
December 1988

Author:



Thomas P. Kelly

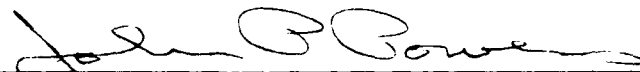
Approved by:



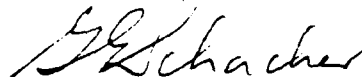
Ramakrishna Janaswamy, Thesis Advisor



Michael A. Morgan, Second Reader



John P. Powers, Chairman, Department of
Electrical and Computer Engineering



Gordon E. Schacher
Dean of Science and Engineering

ABSTRACT

The Linearly Tapered Slot Antenna (LTSA) had been investigated and developed experimentally; its applications have primarily been based on empirical designs. An accurate theoretical model based on Moment Methods (MM) is developed here to study the radiation characteristics of the LTSA. Using the MM solutions to the reaction integral equation, this thesis presents an analysis to model and explain the LTSA behavior. The effects of variable design parameters on radiation patterns are studied. Discussion is augmented by relating predicted radiation patterns to calculated current distributions on the antenna surface. Conclusions are made regarding optimum designs for the LTSA. Relevant observations are made concerning the extensive computational tasks and the computer resources required for the MM model.

Accession For	
NTIS GRA&I	<input checked="" type="checkbox"/>
DTIC TAB	<input type="checkbox"/>
Unannounced	<input type="checkbox"/>
Justification	
By	
Distribution/	
Availability Codes	
Dist	Avail and/or Special
A-1	

TABLE OF CONTENTS

I. INTRODUCTION.....	1
II. THE MOMENT METHOD.....	4
III. LTSA MODEL.....	25
IV. PREDICTED PATTERN BEHAVIORS.....	39
V. CONCLUSIONS OF MODELING STUDY.....	57
APPENDIX A LTSA RADIATION PATTERNS.....	60
APPENDIX B LTSA RADIATION CHARACTERISTICS AS FUNCTIONS OF THE LENGTH AND HEIGHT.....	86
APPENDIX C LTSA CURRENT DISTRIBUTION.....	96
LIST OF REFERENCES.....	136
INITIAL DISTRIBUTION LIST.....	137

I. INTRODUCTION

The many practical advantages of the Linearly Tapered Slot Antenna (LTSA) are based on its low cost, light weight and relative simplicity. Specific designs of LTSA arrays have been implemented for millimeter wave imaging systems and more applications are inevitable. However, since the refinement of an accurate theoretical model has lagged its development, LTSA uses have been based on empirical designs.

Based on the proven Moment Methods (MM) model, developed by Janaswamy [Ref. 1], this paper presents an analysis of the LTSA radiation pattern. The model permits a parametric study of the antenna. The physical antenna variables used in the LTSA modeling are illustrated in Figure 1.1.

Since the method of this research is the MM model, a general review of MM and a specific discussion of the LTSA model are included in Chapters 2 and 3 respectively. It is intended that these chapters address both the accuracy of MM as well as the limitations, particularly with respect to solution by computer. By way of examples, Chapter 2 is demonstrative of the solution by the Moment Method. The MM concept is then advanced in Chapter 3 to explain how the reaction integral equation is solved in the LTSA model. Chapter 3 further serves to discuss the model in terms of computer tasking considerations and approximations which

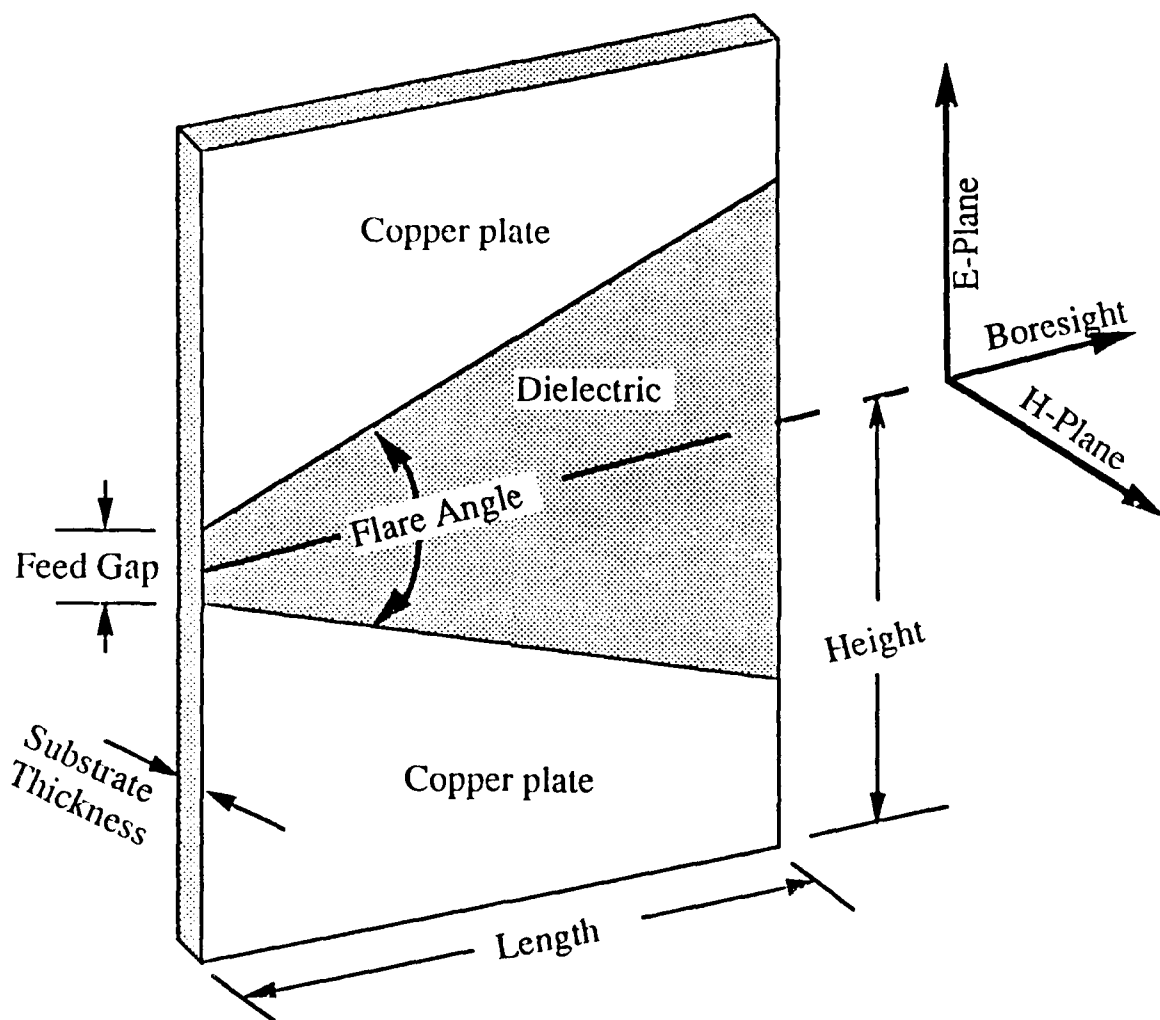


Figure 1.1 Oblique View of the LTSA

alleviate computational burden with little or no sacrifice in accuracy.

Chapter 4 focuses on the LTSA modeling results and analyzes the observed effects of changing beamwidths and sidelobe suppression in the E- and H-planes. Of particular interest are the pattern changes which result from various combinations of antenna length and height, but effects of changing other design parameters are likewise investigated. Corresponding to the radiation pattern changes, surface current distributions are used to explain some phenomena which appear to synergistically create the different patterns. (Appendix C contains current distribution graphs for the respective radiation patterns illustrated in Appendix A).

Conclusions are summarized in Chapter 5. The thrust therein is to provide a credible spectrum of design considerations for the LTSA. It is fully expected that this work has provided the necessary data and rationale for relevant interpolation as well as extrapolation. Moreover, the methods used in this study may well serve similar studies of other antennas and scatterers.

II. THE MOMENT METHOD

A. CONCEPT

Although the Moment Method (MM) is a widely used technique in solving electromagnetics problems, only the advances in computer technology of recent years enable the cost-effective use of MM to pursue such rigorous solutions. Specifically, a linear operator equation with an unknown function is solved by expanding the unknown function and casting it into a system of linear equations which is then solved by known techniques. The thrust of MM is to maintain the exactness of the original equation and to solve it numerically or by other means. This is normally done at the expense of additional computer central processing unit (CPU) time. However, MM generally provides a more accurate solution in comparison to other techniques which reduce and approximate equations solely to minimize the computational effort.

The prescription for solving a problem by MM is best illustrated by an example. Two such examples are chosen for this purpose. The first problem is to solve for $f(x)$ in the Fredholm integral equation of the first kind

$$\int_0^1 f(x) \cos(xy) dx = (1 - \cos y) / y^2. \quad (2.1)$$

The exact solution to the above equation is

$$f(x) = 1-x, \quad 0 < x < 1. \quad (2.2)$$

While exploring this elementary problem in detail, it is intended to demonstrate the MM technique and to highlight both its potential advantages as well as its shortcomings. The second sample problem is to solve for the current distribution, $I(z')$ on a short dipole using Pocklington's integral equation [Ref. 2:p. 307]:

$$\frac{1}{j\omega\epsilon_0} \int_{-L/2}^{L/2} I(z') \left[\frac{\partial^2 \psi(z, z')}{\partial z^2} + \beta^2(z, z') \right] dz' = -E_z^i(z). \quad (2.3)$$

The development and analysis of this equation can be found in most antenna text books and only the application of MM is of current interest.

B. SOLUTION OF THE FREDHOLM INTEGRAL EQUATION

In solving the Fredholm integral equation, the analytical approach is somewhat awkward. However, MM is used with principles of linearity and superposition to reduce the functional equation to a matrix equation of the form $[A][x] = [B]$ [Ref. 3]. Then known techniques are used to determine a unique solution for $[x] = [A]^{-1}[B]$. Equation 2.1 in terms of a linear operator, L , is written as

$$L(f) = g \quad (2.4)$$

where,

$$L = \int_0^1 \cos(xy) dx \quad (2.5)$$

$$g = (1 - \cos y) / y^2. \quad (2.6)$$

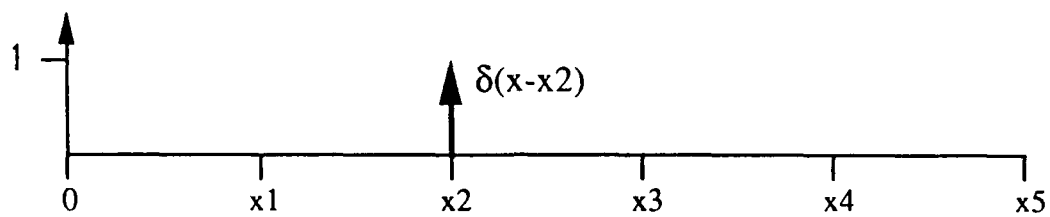
The first step is to expand f into a set of basis functions, $\{f_1, f_2 \dots f_N\}$. N determines the size of matrix to be used and implies both the degree of accuracy and the required computational time. The selection of f_n is more crucial and should be selected to approximate the expected behavior of $f(x)$. Figure 2.1 shows typical functions with which to represent f , where $N = 5$ and

$$f = \sum_{n=1}^N a_n f_n. \quad (2.7)$$

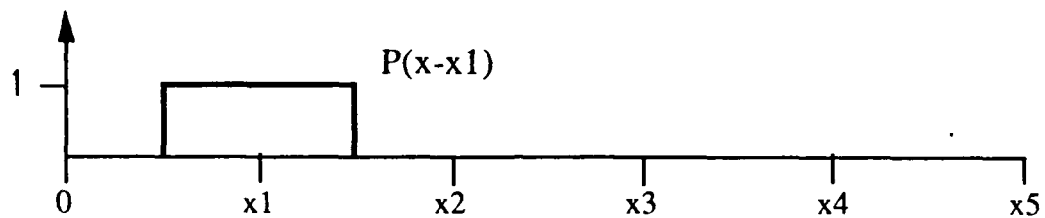
The problem reduces to solving for "best fit" coefficients, a_n for each f_n . Substituting equation (2.7) into (2.4) yields

$$\sum_{n=1}^N a_n \cdot L(f_n) = g. \quad (2.8)$$

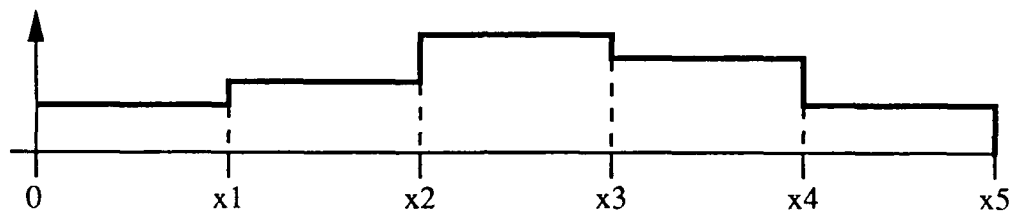
There are now essentially N unknowns, and the number of linearly independent equations must also equal N for a unique solution. This is achieved by selecting a set of weighting functions, $\{w_1, w_2 \dots w_N\}$ in the range of L and equating the weighted averages of equation (2.8) for each w_n ,



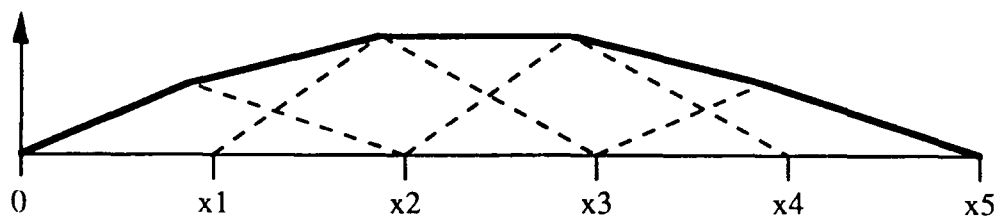
(a) Dirac delta function



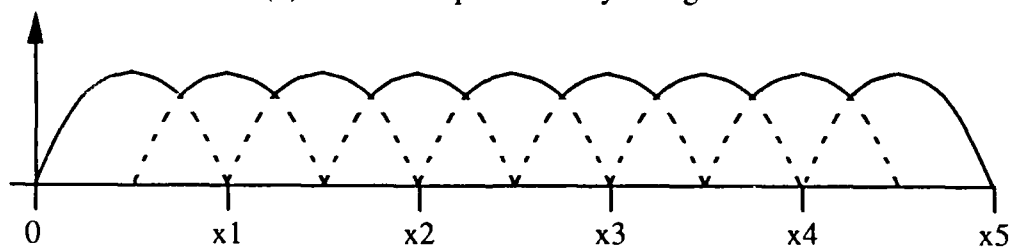
(b) Pulse function



(c) Step approximation



(d) Function represented by triangles



(e) Piecewise sinusoid function

Figure 2.1 Typical Basis Functions.

$$\sum_{n=1}^N a_n \langle w_m, L(f_n) \rangle = \langle w_m, g \rangle. \quad (2.9)$$

Here $\langle \rangle$ denotes the inner product, defined as

$$\langle f, g \rangle \equiv \int_0^1 f(x) g(x) dx. \quad (2.10)$$

For M equations and N unknowns, equations (2.9) is expressed as

$$[l_{mn}][a_n] = [g_m] \quad (2.11)$$

where,

$$[l_{mn}] = \begin{bmatrix} \langle w_1, Lf_1 \rangle & \langle w_1, Lf_2 \rangle & \dots & \langle w_1, Lf_N \rangle \\ \langle w_2, Lf_1 \rangle & \langle w_2, Lf_2 \rangle & \dots & \\ \vdots & & & \\ \langle w_M, Lf_1 \rangle & \dots & \dots & \langle w_M, Lf_N \rangle \end{bmatrix} \quad (2.12)$$

$$[a_n] = [a_1, a_2 \dots a_N]^T \quad (2.13)$$

$$[g_m] = [g_1, g_2 \dots g_M]^T. \quad (2.14)$$

Thus, the unknown coefficients are determined by

$$[a_n] = [l_{mn}]^{-1}[g_m]. \quad (2.15)$$

A point not to casually dismiss is the selection of weighting functions. It is essential that both f_n and w_n be linearly independent sets and that the resulting "l" matrix

have an inverse and be well conditioned. The infinite possibilities for f_n and w_n allow considerable latitude to accommodate (a) the degree of accuracy desired, (b) ease of computation and (c) an acceptable size matrix for inversion. Choices for w_n should be generally based on these criteria while selections of f_n are to help approximate the expected or assumed behavior $f(x)$.

For illustrative purposes, the above Fredholm integral equation is solved with N pulse functions as basis functions. The pulse function $P(x)$ is defined as

$$P(x) = \begin{cases} 1 & |x| < 1/2N \\ 0 & |x| > 1/2N \end{cases} \quad (2.16)$$

Thus, a linear combination of

$$f_n = P(x - x_n) \quad (2.17)$$

gives a step approximation to $f(x)$.

Similarly, N weighting functions are chosen as Dirac delta functions:

$$w_m = \delta(x - x_m), \quad (2.18)$$

with x_m taken as the midpoint of each subinterval. This choice of weighting functions is also known as the point-matching technique. Physically this choice implies that the original integral equation (2.1) is now imposed at the discrete points x_m (the locations of the delta functions),

rather than in the continuous interval, $0 < x < 1$. These selections serve primarily to easily demonstrate the computations rather than to faithfully reproduce $f(x)$. Figure 2.2 shows a pictorial representation of the basis and weighting functions.

For a manageable demonstration, set $N=M=3$. The Fredholm integral equation (2.1) is expressed in the form of equation (2.9):

$$\begin{aligned} & \sum_{n=1}^3 a_n \cdot \langle \delta(y-x_m), \int_0^1 P(x-x_n) \cos(xy) dx \rangle \\ & = \langle \delta(y-x_m), (1-\cos/y^2) \rangle \end{aligned} \quad (2.19)$$

where the inner product is computed using dummy variable, y . Therefore, from equation (2.12), each matrix element

$$\begin{aligned} l_{mn} &= \int_0^1 \delta(y-x_m) \int_0^1 P(x-x_n) \cos(xy) dx dy \\ &= \int_0^1 \delta(y-x_m) \int_{(n-1)/3}^{n/3} \cos(xy) dx dy \\ &= \int_{(n-1)/3}^{n/3} \cos(x \cdot x_m) dx \end{aligned}$$

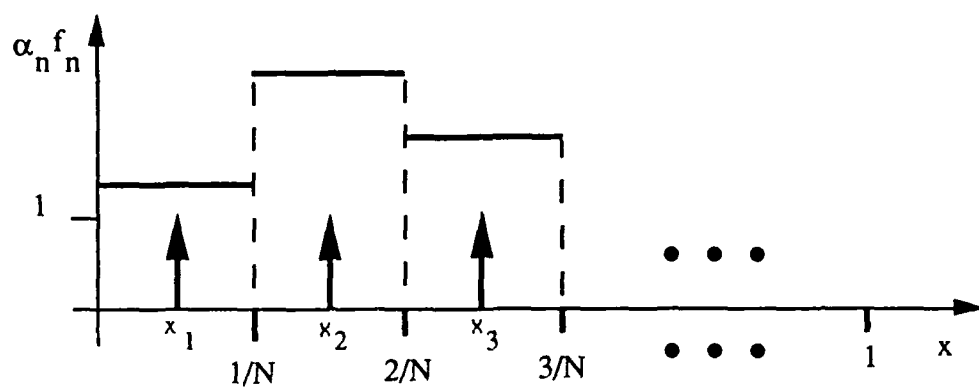


Figure 2.2 Pulse Basis Functions to Represent $f(x)$, with Delta Test Functions Enforced at x_m .

$$= \frac{1}{x_m} \left[\sin \frac{nx_m}{3} - \sin \frac{(n-1)x_m}{3} \right]. \quad (2.20)$$

In the same manner,

$$g_m = \int_0^1 \delta(y-x_m) \left[\frac{1 - \cos y}{y^2} \right] dy = \frac{1 - \cos x_m}{x_m^2}. \quad (2.21)$$

Solving equations (2.20), (2.21) and (2.15) yields

$$[l_{mn}] = \begin{bmatrix} .3332 & .3321 & .3301 \\ .3318 & .3226 & .3045 \\ .3291 & .3038 & .2553 \end{bmatrix} \quad (2.22)$$

$$[g_m] = [.4988 \quad .4897 \quad .4717]^T \quad (2.23)$$

$$[a_n] = [.8319 \quad .5647 \quad .1034]^T. \quad (2.24)$$

This solution is depicted with the exact solution ($f(x) = 1-x$) in Figure 2.3.

Figure 2.3 seems to suggest that the accuracy of the numerical solution may be improved by increasing the number of basis functions. While this may be true in general, it needs a high degree of precision to actually achieve it. For a given N , the percent error is less if the precision is increased. Conversely, for a given precision, increasing N eventually results in an increase in percent error. The accuracy will also be affected by moving the matching point,

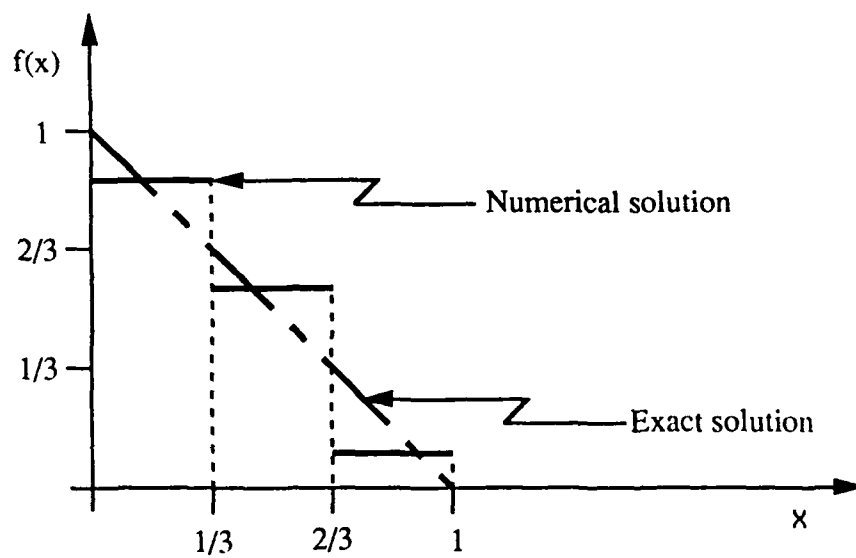


Figure 2.3 Numerical (by MM) and Exact Solutions for the Fredholm Integral Equation.

i.e., by shifting the weighting functions $\delta(x-x_m)$ within the corresponding subinterval

$$\frac{m-1}{N} < x_m < \frac{m}{N}. \quad (2.25)$$

In another approach known as Galerkin's technique, the set of weighting functions is the same as the set of basis functions, i.e., $w_n = f_n$. This results in a symmetric $N \times N$ matrix and reduces the required number of computations needed for filling the matrix.

Reviewing a few different MM solutions to the Fredholm integral provides greater insight. Various MM approaches and results are itemized in Table 2.1. For this problem and the limited trials indicated, a few conclusions are made:

- * The noticeably low value of N is the largest which can be used before the matrix becomes ill-conditioned. This is attributable to the available limits of precision in the mantissa.
- * Use of Galerkin's technique does not appear to have a dominant effect on accuracy.
- * Selection of apparently suitable basis functions does not guarantee convergence, since any N too large may result in an ill-conditioned matrix.
- * Shifting the weighting functions in the point matching technique does not significantly affect the solution for $[a_n]$.

The ambiguous tone of these conclusions alludes to the obvious point that few solutions offer the neatness of $f(x) = 1-x$. What is to be gleaned from this example is that there are limitations to the MM process. No exact guidelines exist

TABLE 2.1 REPRESENTATIVE SELECTIONS OF BASIS AND WEIGHTING FUNCTIONS TO SOLVE THE FREDHOLM INTEGRAL.

Basis Function	Weighting Function	N	Precision	Solution $[a_n]^T$
Pulse	Dirac Delta enforced @ center of sub-interval	3	Single	[.8319 .5647 .1034]
Pulse	Dirac Delta enforced @ left of subinterval	3	Single	[.8343 .5611 .1046]
Pulse	Dirac Delta enforced @ left of subinterval	5	Double	[.9622 .6283 .5167 .3288 .0641]
Pulse	Pulse Galerkin	3	Single	[.8449 .5451 .1101]
Pulse	Pulse Galerkin	3	Double	[.8379 .5557 .1064]
Powers of x ($x^0, x^1 \dots$ x^{N-1})	Dirac Delta enforced @ $x_m = (2m-1)/N$	3	Single	[.9778 -.8841 .1072]
Powers of x ($x^0, x^1 \dots$ x^{N-1})	Dirac Delta enforced @ $x_m = (2m-1)/N$	2	Single	[.9991 -.9881]
Powers of x ($x^0, x^1 \dots$ x^{N-1})	Powers of x (Galerkin) @ $x_m = (2m-1)/N$	2	Single	[.9974 -.9946]

for the best choice of expansion and weighting functions for a given integral equation. In spite of this shortcoming, MM is much more useful in solving an integral equation, particularly when it cannot be solved in a closed-form, e.g., $A \cdot \cos(wt)$. This point is reinforced in the next example.

C. SOLVING FOR CURRENT DISTRIBUTION ON A DIPOLE

Consider now an electromagnetics application of MM to solve for current distribution on a linear dipole. The motivation for finding current distribution on any antenna is to eventually solve for the radiation pattern and/or the input impedance. Since this is the idea of the LTSA model specifically discussed in Chapter 3, an example of MM to solve the Pocklington integral equation is worthwhile.

Using the conventional assumptions for thin wire antennas and illustrations of Figure 2.4, the problem statement is to solve for the current, $I(z')$ on a short dipole with length, $L = .1\lambda_0$ and radius, $a = .005\lambda_0$. Assume a 1 volt center-fed excitation.

In a simpler form, equation (2.2) is written as

$$\frac{1}{j\omega\epsilon_0} \int_{-L/2}^{L/2} I(z') K(z, z') dz' = -E_z^i \quad (2.26)$$

where the kernel,

$$K(z, z') = \frac{\partial^2 \psi(z, z')}{\partial z^2} + \beta^2 \psi(z, z') \quad (2.27)$$

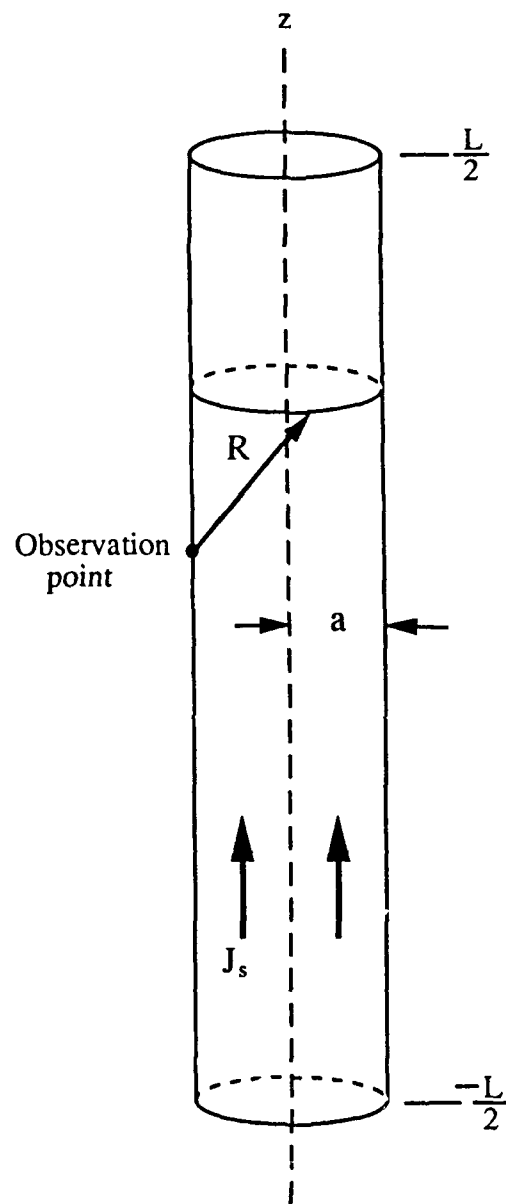


Figure 2.4 Linear Dipole Illustrated as a Wire With Surface Current Density J_s and Observation Point on the Surface.

and the free space Green's function is

$$\psi(z, z') = \frac{e^{-j\beta R}}{4\pi R}. \quad (2.28)$$

Equation (2.25) is expanded and simplified for integration:

$$K(z, z') = \frac{e^{-j\beta R}}{4\pi R^3} [(1 + j\beta R)(2R^2 - 3a^2) + a^2\beta^2 R^2]. \quad (2.29)$$

It is readily apparent that the required complex integration is best done numerically and is well-suited for a modest computer program. However, for present purposes only, the MM concept and results need be explained.

Following the same procedure as in the previous example, the steps are simple: (a) expand $I(z')$ in a set of basis functions; (b) obtain linear equations by weighting functions and computing inner products; and (c) use matrix algebra to solve for the unknown coefficients of the basis functions.

For simplicity sake, $N=5$ is chosen to limit the matrix dimensions. For interpretive convenience, $I(z')$ is approximated by a series of pulse functions (see Figure 2.5):

$$I(z') = \sum_{n=1}^5 I_n F_n(z') \quad (2.30)$$

where I_n is a complex unknown number and

$$F_n(z') = \begin{cases} 1 & \text{for } z' \text{ in } z'_n \\ 0 & \text{elsewhere.} \end{cases} \quad (2.31)$$

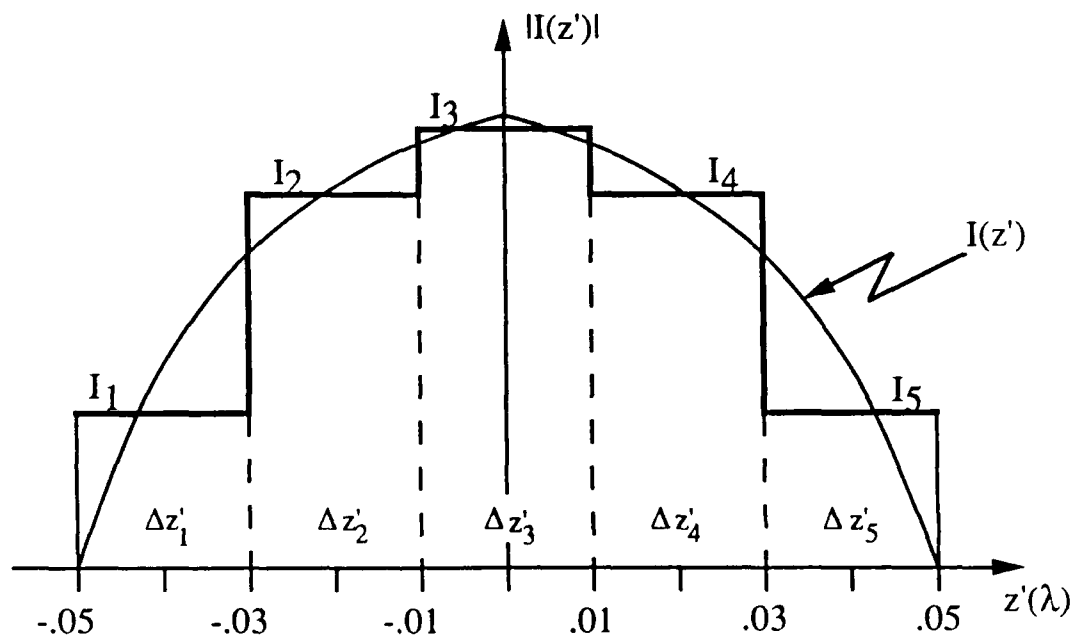


Figure 2.5 "Staircase" Approximation to an Actual Current Distribution.

Substituting equation (2.30) into (2.26) yields

$$\frac{1}{j\omega\epsilon_0} \sum_{n=1}^5 I_n \int_{-L/2}^{L/2} F_n(z') K(z, z') dz' \approx - \frac{i}{z} E(z). \quad (2.32)$$

Selection of weighting functions is influenced by the desire to make computations simple. Therefore, the point-matching technique is used. The weighting functions are

$$w_m(z) = \delta(z - z_m). \quad (2.33)$$

Taking the inner products in equation (2.32) produces

$$\frac{1}{j\omega\epsilon_0} \sum_{n=1}^5 I_n \int_{-L/2}^{L/2} F_n(z') K(z_m, z') dz' \approx - \frac{i}{z} E(z_m). \quad (2.34)$$

The subscript, m , is considered the match point index because it is associated with the observation point at which the m^{th} equation is valid. The source point index, n , is so called because it refers to the field from the current on the n^{th} segment. For mathematical convenience, the locations of enforcement are at the centers of each segment. (It is important to recognize that while mathematically simple, point matching actually relaxes the boundary conditions

$$\frac{i}{z} E + \frac{s}{z} E = 0 \quad (2.35)$$

between selected points. Such simplification should be questioned before hastily using this technique in other antenna problems).

Equation (2.34) is solved as a matrix equation:

$$[Z_{mn}][I_n] = [V_m] \quad (2.36)$$

where

$$Z_{mn} = \frac{1}{j\omega\epsilon_0} \int_{(n-1)L/2}^{nL/2} F_n(z') K(z_m, z') dz' \quad (2.37)$$

$$V_m = -E \frac{1}{z}(z_m). \quad (2.38)$$

Note the mathematical convenience of (2.36) which is analogous (but not equivalent) to Kirchhoff's network equations. Because of the analogy, however, $[Z_{mn}]$, $[I_n]$ and $[V_m]$ are respectively referred to as generalized impedance, current and voltage matrices.

Before solving equation (2.36), $[V_m]$ must be defined for the given problem. Source modeling is a subject worthy of exploration beyond this study [Ref. 2]. Two most popular versions are (a) the delta gap generator that corresponds to feeding by an ideal voltage source and (b) a magnetic frill generator that corresponds to feeding by a coax cable from a ground plane. Here, a 1 volt center fed excitation, when modeled with a frill generator and weighted with delta testing functions, results in

$$[V_m] = \begin{bmatrix} 0.502 & \angle -179.69^\circ \\ 3.248 & \angle -179.95^\circ \\ 70.55 & \angle -179.99^\circ \\ 3.248 & \angle -179.95^\circ \\ .502 & \angle -179.69^\circ \end{bmatrix}. \quad (2.39)$$

The above choice of uniform segmentation of the wire results in an impedance matrix that is Toeplitz symmetric. (In a Toeplitz matrix, $Z_{mn} = Z_{1, |m-n|+1}$ for $m \geq 2, n \geq 1$.) Thus, the first column (identical to the first row) is all that is needed to fill Z_{mn} .

$$[Z_{m1}] = 10^2 \cdot \begin{bmatrix} 679.2 & \angle 90.01^\circ \\ 292.4 & \angle -90.03^\circ \\ 33.01 & \angle -90.27^\circ \\ 9.74 & \angle -90.01^\circ \\ 4.24 & \angle -92.08^\circ \end{bmatrix}. \quad (2.40)$$

Solving (2.36) for $[I_n]$ yields

$$[I_n] = 10^3 \cdot \begin{bmatrix} .81 & \angle 89.54^\circ \\ 1.54 & \angle 89.64^\circ \\ 2.44 & \angle 89.75^\circ \\ 1.54 & \angle 89.64^\circ \\ .81 & \angle 89.54^\circ \end{bmatrix}. \quad (2.41)$$

The solution for $[I_n]$ is consistent with expected results. The current distribution is generally triangular. The input impedance is largely capacitive with a real part less than 2 ohms. Nevertheless, a more accurate solution for $[I_n]$ is obtainable with a larger N . Figure 2.6 shows how a

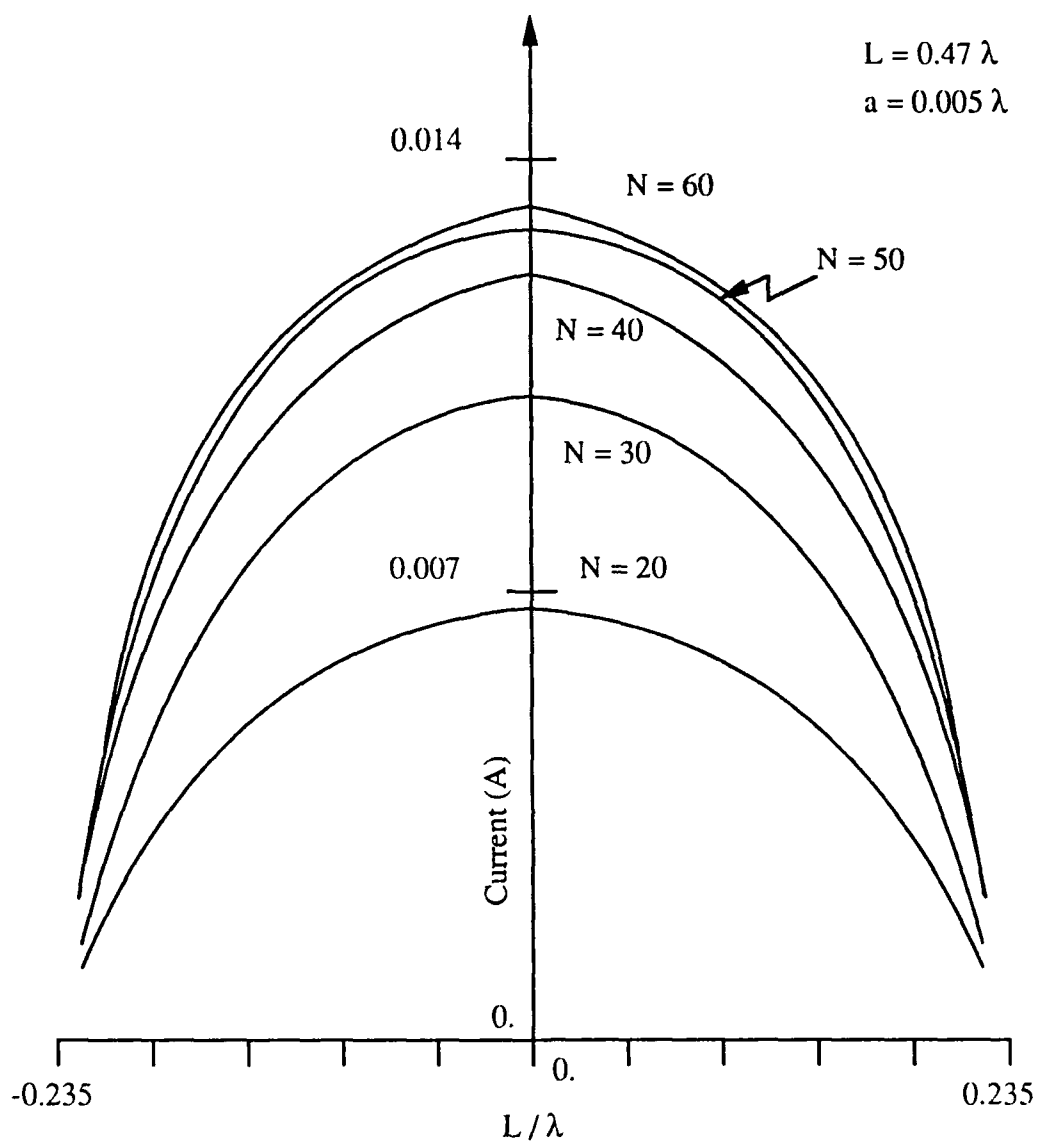


Figure 2.6 Current Distributions on a Half-wave Dipole for Various Numbers of Basis Functions and a Unit Volt Source [Ref. 2: p.314].

solution for $[I_n]$ converges by increasing N in a similar problem [Ref. 2:p. 314].

The purpose of this example has been to demonstrate the MM application to a simple antenna problem. It is necessary to qualify its obvious merit by a few key points which generally apply to all MM problems.

- * The matrix dimension N (number of expansion modes) must be taken sufficiently large to get a convergent result but not so large as to cause numerical instability.
- * Small numerical errors due to round-off or truncation usually have catastrophic effects if they cause apparent singularities or ill-conditioning in the matrix.
- * Choice of appropriate basis functions not only improves the accuracy but reduces the matrix size needed for a convergent solution. In the case of a short dipole, the expected triangular current distribution suggests that piecewise linear or triangle basis functions should give a better representation of $I(z')$.
- * Galerkin's technique, (chosen expansion and weighting functions are the same) is computationally convenient on a computer but does little to affect accuracy. If pulse-pulse Galerkin method is used on the dipole example, convergence is achieved with a different N .

III. LTSA MODEL

In order to examine the various parametric effects of LTSA design on radiation patterns, a valid antenna model is required. While LTSA applications are primarily based on empirical designs, recently published works have advanced the necessary theory to describe the LTSA behavior. Among them is a paper by Janaswamy [Ref. 1]. His model enables the prediction of pattern behavior which agrees closely with LTSA experimental results. It is Janaswamy's MM model, algorithmic steps and Fortran programs which are used in this study. Accordingly, this chapter summarizes the purpose and process of this new model.

Analogous to the linear dipole example, the immediate objective is to solve for the current distribution on the surface of the antenna for a given excitation. The current is determined by solving the reaction integral equation which states that [Ref. 1]

$$\iint_S (J^s \cdot R^T - M^s \cdot H^T) ds = - \iiint_V (J^i \cdot E^T - M^i \cdot H^T) dv \quad (3.1)$$

where (E^T, H^T) is the free space field of an electric test source J^T placed on the surface S . (J^i, M^i) are the impressed sources (excitation) bounded by volume V . (J^s, M^s) represent the unknown total surface currents on the antenna. Using the

concept of surface impedance, the currents J^s and M^s can be related as

$$M_s = Z_s J_s \times n. \quad (3.2)$$

The surface impedance concept is useful in simplifying an otherwise difficult case of the dielectric supported antenna. We recognize that $M_s \equiv 0$ on perfect conductors (air dielectric). However, on dielectric supported antennas, the presence of the thin dielectric slab is treated by means of the surface impedance Z_s . The surface impedance Z_s is a function of the relative dielectric constant and the substrate thickness in wavelengths (See Table 3.1). According to equation (3.2), a non-zero value of Z_s results in additional electric surface currents. In either case, equation (3.1) is solved for the single unknown J^s .

The MM approach begins with selection of expansion modes (synonymous with basis functions) used to model J^s . Besides choosing appropriate functions, this step has other significant implications which first demand consideration. The number of modes should be as small as possible to reduce computation time but large enough to insure convergent results for the radiation pattern. To that end, one helpful simplification is to reconsider the antenna structure. Both the number of expanded unknowns in

$$J^s = \sum_{n=1}^N I_n J_n, \quad (3.3)$$

**TABLE 3.1 SURFACE IMPEDANCES FOR TYPICAL DIELECTRIC
SUPPORTED LTSA (INDUCTIVE REACTANCE, OHMS)**

Substrate Thicknes $d(\lambda_0)$:	Relative Dielectric Constant, ϵ_r :				
	1.04	2.33	3.5	6.0	10.5
.01	11.86	11.88	11.90	11.94	12.01
.015	17.82	17.89	17.95	18.09	18.34
.021	25.02	25.21	25.39	25.78	26.51
.025	29.86	30.19	30.49	31.16	32.46
.030	35.97	36.54	37.08	38.29	40.73
.040	48.44	49.84	51.20	54.43	61.65
.050	61.33	64.22	67.13	74.55	94.28

and the computation time are reduced considerably when the trapezoidal plates of Figure 3.1a are modeled with uniformly rectangular patches as shown in Figure 3.1b. This segmentation allows overlapping surface dipoles to represent each J_n as current flow along either principal direction of the plates. Accordingly, Figure 3.1c represents the geometric approximation for each plate where the feed gap is denoted as $2W_f$. (This is valid for flare angle 2α less than 40° .)

If the number of segments along H and L are N_H and N_L , respectively, the number of modes per plate is

$$N_P = N_L(N_H-1) + N_H(N_L-1). \quad (3.4)$$

As the two plates comprising the antenna surface are identical, they both have the same number of modes. Including one mode to represent the feed dipole, the total number of modes on the structure is

$$N = 2N_P + 1. \quad (3.5)$$

Selection of functions to represent each mode are illustrated in Figure 3.2 where the assumed direction of current flow is along the z axis. For each surface dipole, the current is represented by the Piecewise Sinusoid (PWS) in the z direction and constant along the y direction.

Using the representations of Figures 3.1 and 3.2, a three dimensional view of current is obtained by examining two cross-section views. Figure 3.3a depicts Cut AA, which is

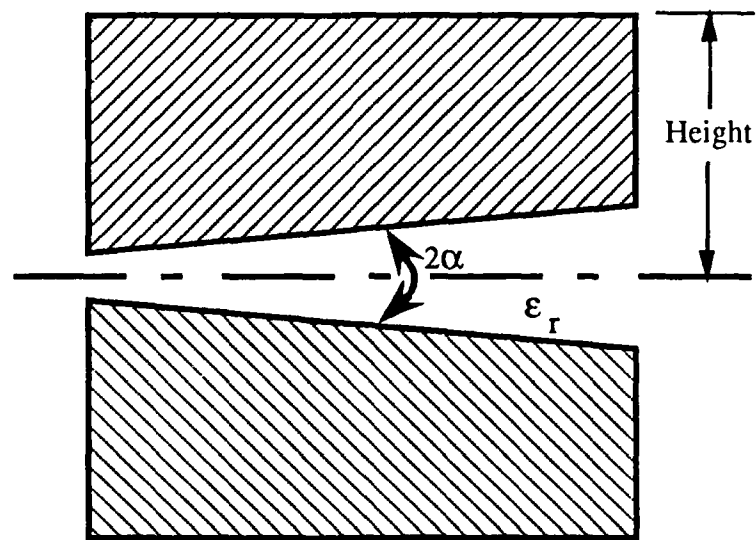


Figure 3.1a LTSA Surface Geometry.

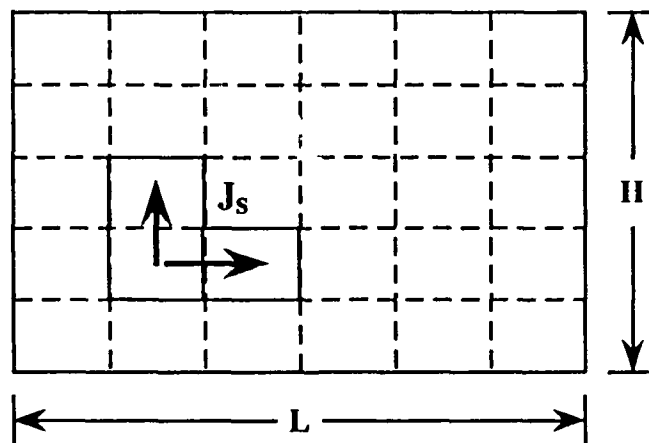


Figure 3.1b Surface Dipoles Overlapping on Rectangular Patches.

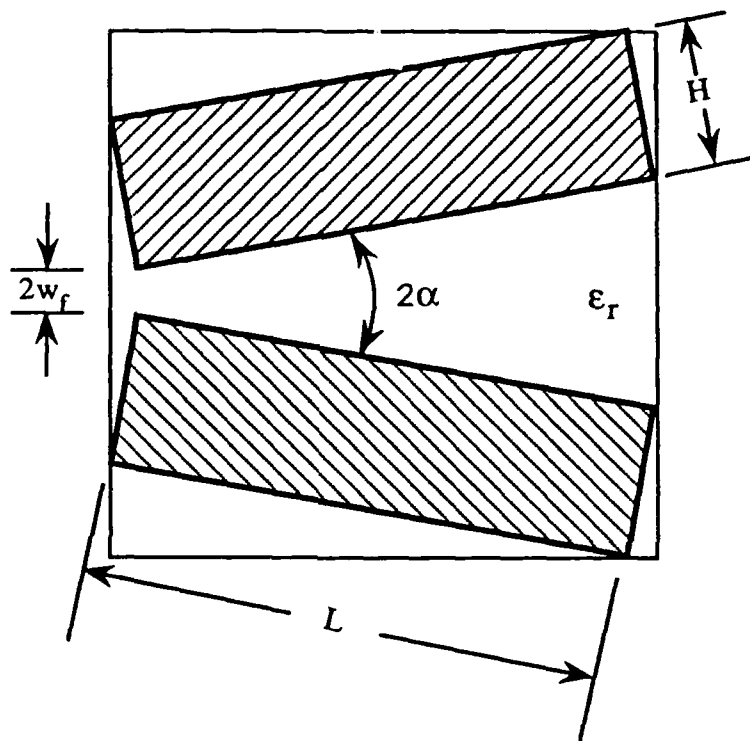


Figure 3.1c Equivalent LTSA Geometry for Modeling.

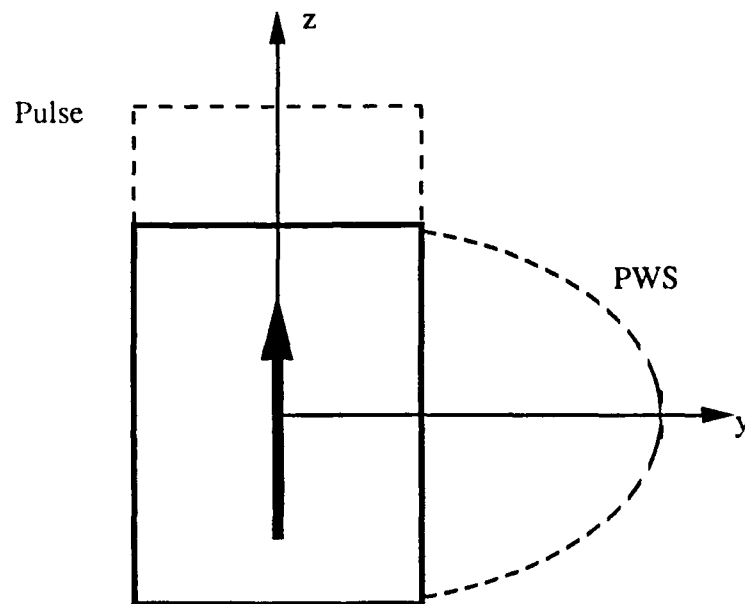


Figure 3.2 Surface Dipole Representation for Each Mode.

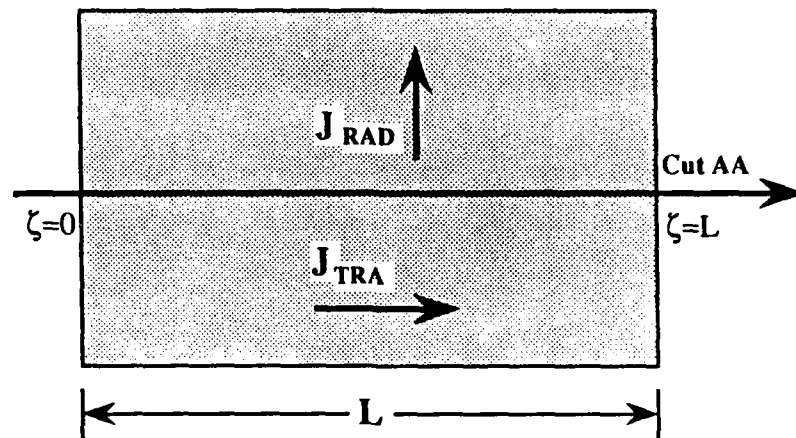


Figure 3.3a Cross Section of Current Distribution Along the Length Dimension of the Plate (Cut AA).

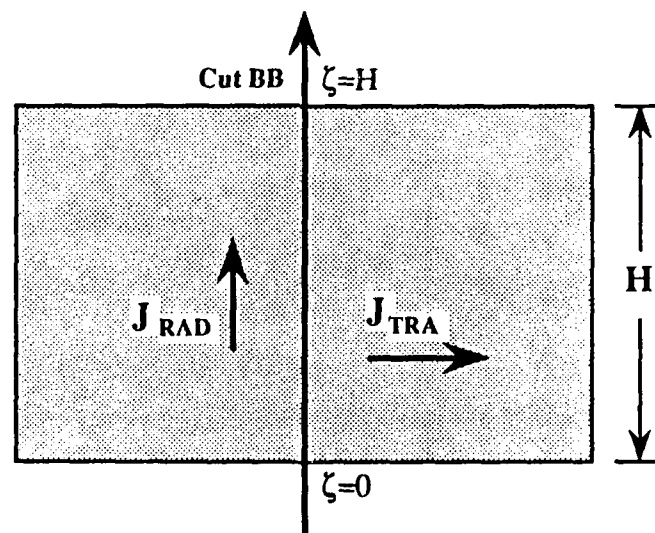


Figure 3.3b Cross Section of Current Distribution Along the Height Dimension of the Plate (Cut BB).

used to portray current behavior along the length dimension. Similarly, Figure 3.3b is Cut BB, which provides a view of current behavior along the height. Consequently, current is analyzed using two separate plots of J_{TRA} and J_{RAD} as seen in Appendix C.

The test modes (weighting functions) for J^T are chosen identical to the expansion modes for J^e , hence the method is Galerkin. Although other choices are possible, PWS Galerkin is best suited in the MM procedure for scattering problems in free space and is proved to be satisfactory in this model.

Having formulated the MM strategy, equation (3.1) is solved by substituting (3.2), (3.3) and using the familiar form

$$[Z_{mn}][J_n] = [V_m] \quad (3.6)$$

where

$$Z_{mn} = Z_s \iint_n J_n \cdot J_m^T ds - \iint_n J \cdot E_m^T ds \quad (3.7)$$

and

$$V_m = \iiint_v (J^i \cdot E_m^T - M^i \cdot H_m^T) dv. \quad (3.8)$$

Here, Z_{mn} represents the mutual impedance between the m^{th} testing mode (weighting function) and the n^{th} expansion mode (basis function) and can be termed the inner product, $\langle J_n, E_m^T \rangle$. The complete discussion of equation (3.7) need not

be expanded here but two aspects of Z_{mn} are significant in this LTSA model.

- * Janaswamy treats the cases of parallel and non-parallel dipoles with different algorithms and uses closed form expressions where appropriate. In concert with the problem symmetry, his approach improves computational efficiency.
- * Filling the impedance matrix is a time consuming task. Table 3.2 provides typical CPU times required to fill and perform LU decomposition on such a matrix. Owing to aforementioned symmetry, matrices require only dimension N' , where $N' = N_p + 1$. Therefore the matrix $[Z_{mn}]$ has $(N')^2$ elements. The preponderance of LTSA modeling problems requires $N' > 130$, for which a virtual memory of 1500 Kilobytes is recommended. For N' greater than 200, 2 Megabytes of memory are necessary.

As suggested in the dipole example, increasing N improves the approximation of the current distribution. However, practical consideration of the required computer resources dictates a limit for N . Janaswamy has demonstrated that convergent results are obtained for the radiation pattern when the LTSA height and length are partitioned into four to five segments per wavelength. This criteria was used throughout the modeling study.

It is worth mentioning that an accurate LTSA input impedance can be calculated only if convergence is achieved in the solution for $[I_n]$. Because an even larger N is required, this task is not undertaken.

The matrix $[V_m]$ in equation (3.3) is determined by the type of excitation used in the model. In the present model, a delta gap generator is used, corresponding to a transmitting antenna. By reciprocity, the solution is also

TABLE 3.2 TYPICAL CPU TIME AND STORAGE REQUIREMENTS FOR THE
IMPEDANCE MATRIX OF THE LTSA MODEL (USING VS
FORTRAN AND IBM 3033)

Segments per Plate		Dimensions of Matrix		CPU Time in Minutes	Matrix Stor- age in Bytes (Formatted File)
N _r	N _{tr}	N	N'		
15	2	87	44	8.0	16K
20	2	117	59	14.4	280K
25	2	147	74	22.6	440K
15	5	261	131	71.5	1.4M
23	6	495	248	245.	4.9M

valid for the receiving case. This choice results in V_m equal to zero, except at the source segment where it is unity. Due to the plate corners which would cause undue fringing around the feed gap, the normal direct connection is not used. Instead, the generator is superimposed on a strip dipole centered across the feed gap, as depicted in Figure 3.4. The feed dipole length and width are $2L_d$ and $2W_d$ respectively. Results of this study show that the far-fields are relatively insensitive to changes in the feed dipole dimensions (See Figure 3.5). The apparent H-plane behavior change shown in Figure 3.5b is attributable to the fact that only one expansion mode is used for the source. Figures A.1 through A.4 further demonstrate more vividly that these effects are insignificant.

In summary of the purpose and process of the LTSA model, the MM technique provides an approximation of the current distribution which is subsequently used to compute the far-field radiation pattern. A point worth emphasis is the criterion of choosing four to five segments per wavelength in either principal direction of the plate. While this is not enough to obtain convergent results for current distribution, it is quite accurate for the radiation pattern. Moreover, this model provides predicted patterns well corroborated by empirical results. Thus, the only apparent limits on its effectiveness are established by the computer resources available.

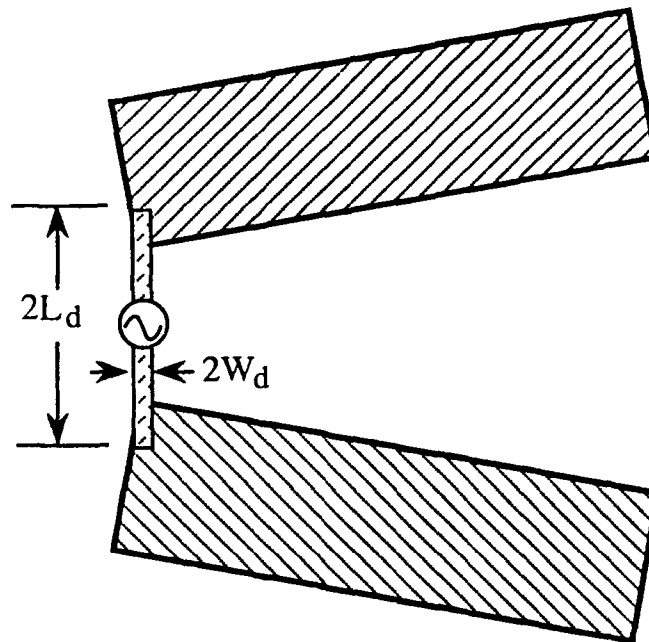


Figure 3.4 Source Model of Unit Volt Excitation on a Surface Dipole Placed across the Feed Gap.

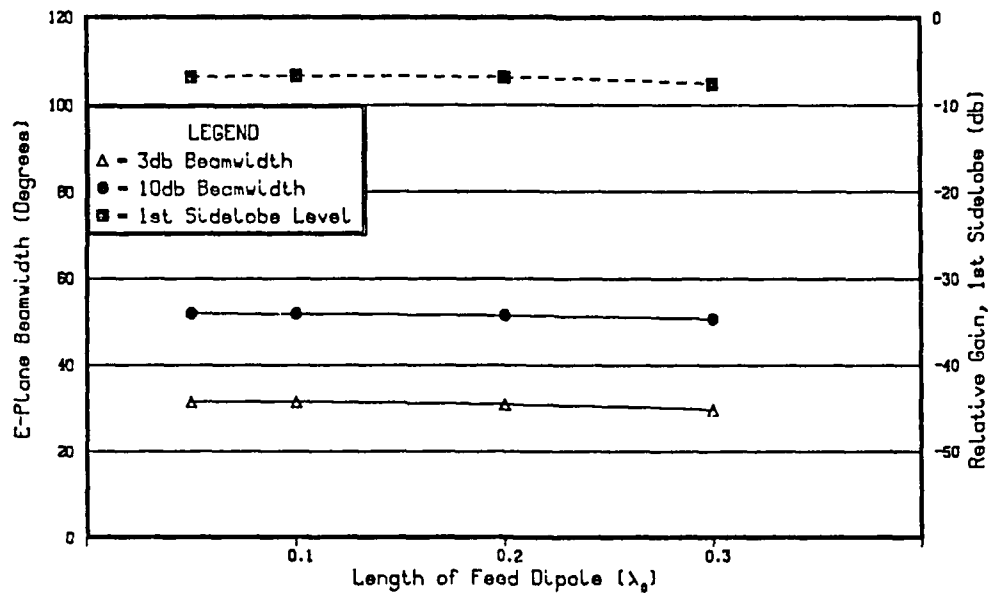


Figure 3.5a E-Plane Effects of Dipole Modeling.

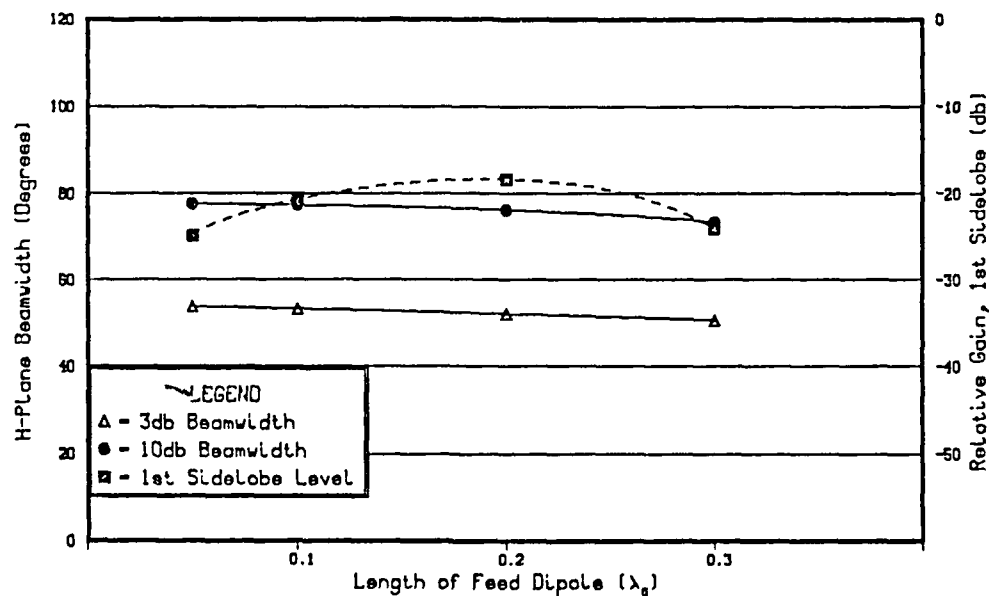


Figure 3.5b H-Plane Effects of Dipole Modeling.

IV. PREDICTED PATTERN BEHAVIORS

A. BACKGROUND

The theoretical model provides the opportunity to develop specific parametric analysis of the LTSA. Heretofore, these analyses have only been experimentally performed. Therefore, the ability to accurately predict radiation pattern behavior is a significant step in the LTSA design methodology.

Before the correlation of behavior changes to design changes can yield useful results, a validated set of design parameters is necessary. For reference and comparison purposes, the following LTSA design parameters are used:

- * Length, $L = 3.0\lambda_0$
- * Height, $H = 0.9\lambda_0$
- * Feed point gap, $2W_f = .02\lambda_0$
- * Flare angle, $2\alpha = 12^\circ$
- * Substrate dielectric constant, $\epsilon_r = 2.33$
- * Substrate thickness, $d = .021\lambda_0$.

The predicted radiation pattern for the reference data is shown in Figure 4.1.

The modeled behavior corresponds very well to experimental results obtained with this specific design [Ref. 1]. Hence, the investigation of LTSA behavior proceeds by varying one design parameter at a time and observing the attendant effects on the radiation patterns. This technique

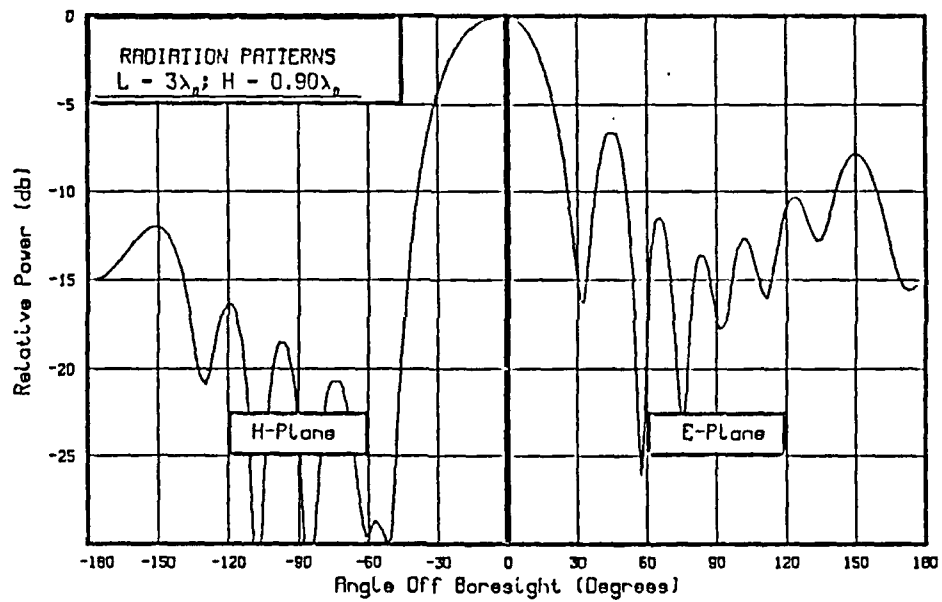


Figure 4.1 Predicted Patterns for a Known Empirical Design.

is well illustrated in Appendix A which contains radiation pattern comparisons for the designs modeled in this study.

A more succinct analysis is obtained by describing the main beam and sidelobe properties with three attributes for each plane. They are:

- * Half-power or 3 db beamwidths (HP_E, HP_H)
- * 10 db beamwidth,
- * Level of first sidelobe relative to main beam.

Together these attributes indicate the directivity of the antenna and provide a basis with which to compare antenna designs. The equation used to approximate the directivity of the LTSA is

$$D = 52,525 / (HP_E HP_H) \quad (4.1)$$

where HP_E and HP_H are in degrees and a smooth elliptical main beam cross-section is assumed [Ref. 2:p. 396].

B. LENGTH OF THE LTSA

It has been demonstrated by earlier theory and experiment, that for LTSA lengths (L) of three to ten wavelengths, narrower beamwidths are obtained by increasing L [Ref. 4]. Based on known behavior of antennas such as the Vee dipole and horn antennas, this is a reasonable expectation. However, results obtained with the present model are accurate enough to offer more specific observations.

Radiation patterns for $L = 3\lambda_0$, $4\lambda_0$ and $5\lambda_0$ have been computed for heights (H) of $.25\lambda_0$ to $1.5\lambda_0$. (See Figures A.5 through A.16). A synopsis of significant findings concerning length is deduced from Figure 4.2. For a nominal height of one wavelength, radiation pattern characteristics are plotted as a function of length.

As L is increased the progressive decrease in beamwidth is evident in both the E and H planes. Since the directivity is inversely proportional to the beamwidths' product, the improvement between $L = 3\lambda_0$ ($HP_E = 35^\circ$, $HP_H = 45^\circ$) and $L = 5\lambda_0$ ($HP_E = 21^\circ$, $HP_H = 37^\circ$) is approximately 3 db.

Also noteworthy is the concurrent sidelobe reduction which is most apparent in the H-plane. Although Figure 4.2 shows only the relative gain of the first sidelobe, review of Figures A.11 and A.12 indicates that the main beam is well-formed and that there are no sidelobe anomalies. Suppression of the E-plane sidelobes below -10 db is achieved with $L > 4\lambda_0$.

Figures B.1 through B.6 demonstrate that the observed trends for changing L are consistent for several heights ($.25\lambda_0 - 1.5\lambda_0$). Thus, a further interpretation regarding length is worth consideration. To compute an actual antenna gain, the input reflection coefficient or the input impedance is required. However, design for a particular directivity can be accomplished with equation (4.1).

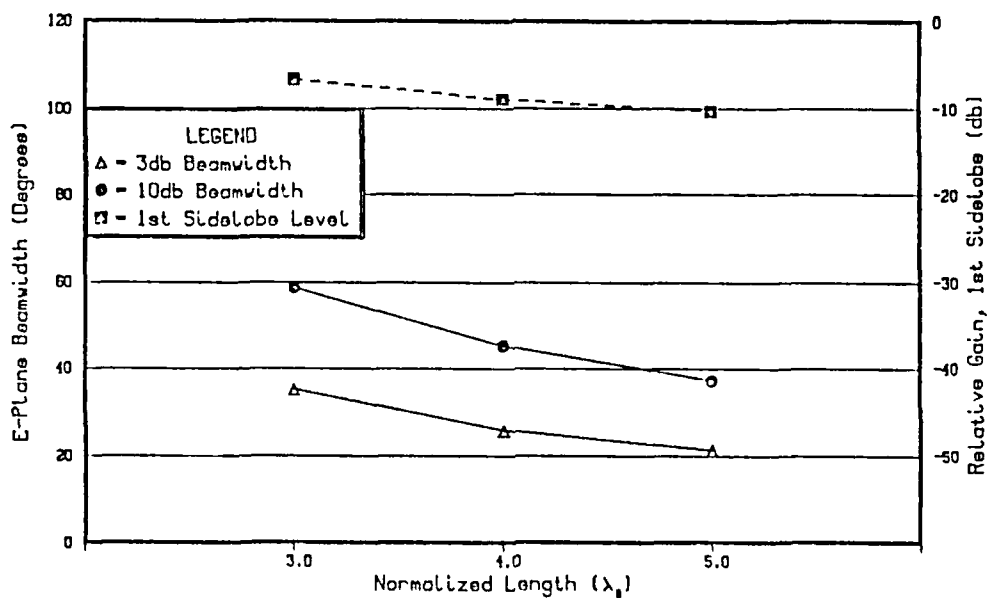


Figure 4.2a E-Plane Effects of Changing L ; $H = 1.00\lambda_0$.

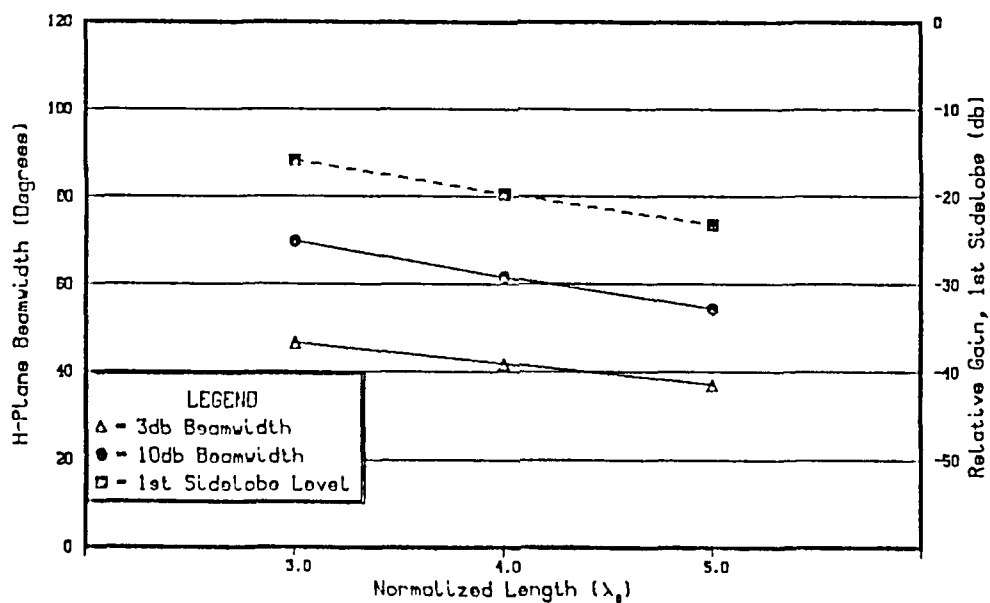


Figure 4.2b H-Plane Effects of Changing L ; $H = 1.00\lambda_0$.

For example, if a directivity of 17 db is required, the $HP_E \cdot HP_H$ product must be less than 1048. Figure 4.2 indicates at $L = 4\lambda_0$ that $HP_E \approx 25^\circ$ and $HP_H \approx 41^\circ$. It is apparent that a nominal antenna length of $4\lambda_0$ is at least a good starting point for this design.

C. LTSA HEIGHT

Earlier theory for the LTSA had only been developed for large height ($H \leq 3\lambda_0$). Experiments with an air dielectric LTSA ($L = 7.2\lambda_0$) showed that a progressively narrower E-plane beamwidth is obtained when it was shortened to $1.5\lambda_0$, but that at $.75\lambda_0$, the HP_E broadened once again [Ref. 5]. This apparent resonant effect appears in modeling a shorter antenna ($L = 4\lambda_0$) as depicted in Figure 4.3a. When $H \approx 1.25\lambda_0$, there is a distinct narrowing of HP_E . Compared to $H = 1.5\lambda_0$, this represents a directivity increase of about 2 db. For H decreasing below $1\lambda_0$, the HP_E tapers to less than 20° at $H = .25\lambda_0$.

In the H-plane the cited experiments showed a broadening of HP_H for decreasing height. This is consistent with the predicted behavior shown in Figure 4.3b. However, as H is reduced below $.75\lambda_0$, HP_H decreases and the 10 db beamwidth virtually disappears. Figure A.22 shows the emergence of large sidelobes at $H = .25\lambda_0$, while Figure A.23 demonstrates that the beam is not well formed at $H = .50\lambda_0$. These effects are also observed at $L = 3\lambda_0$ (Figure B.7) and $L = 5\lambda_0$ (Figure B.9).

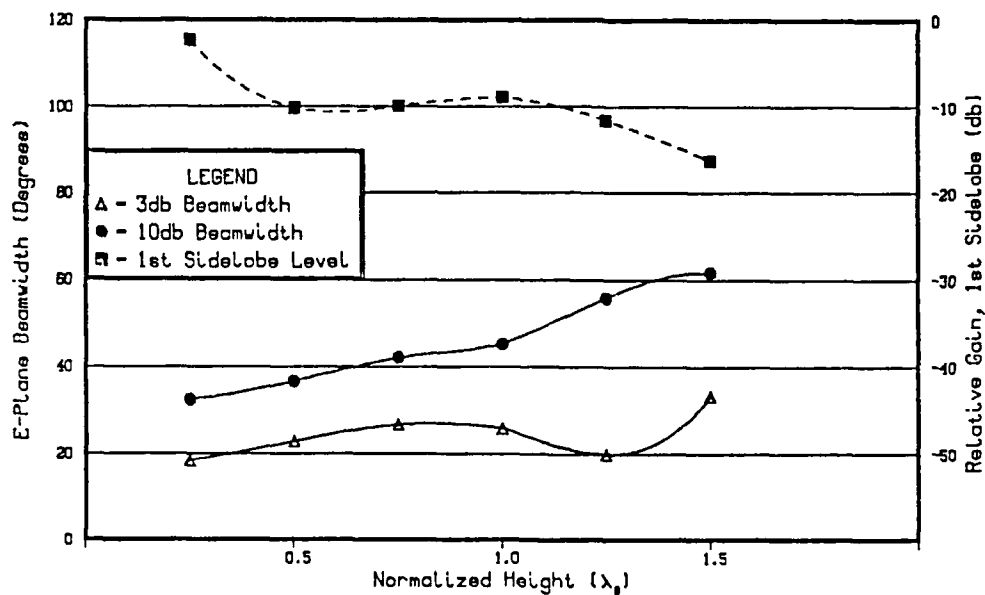


Figure 4.3a E-Plane Effects of Changing H; $L = 4\lambda_0$.

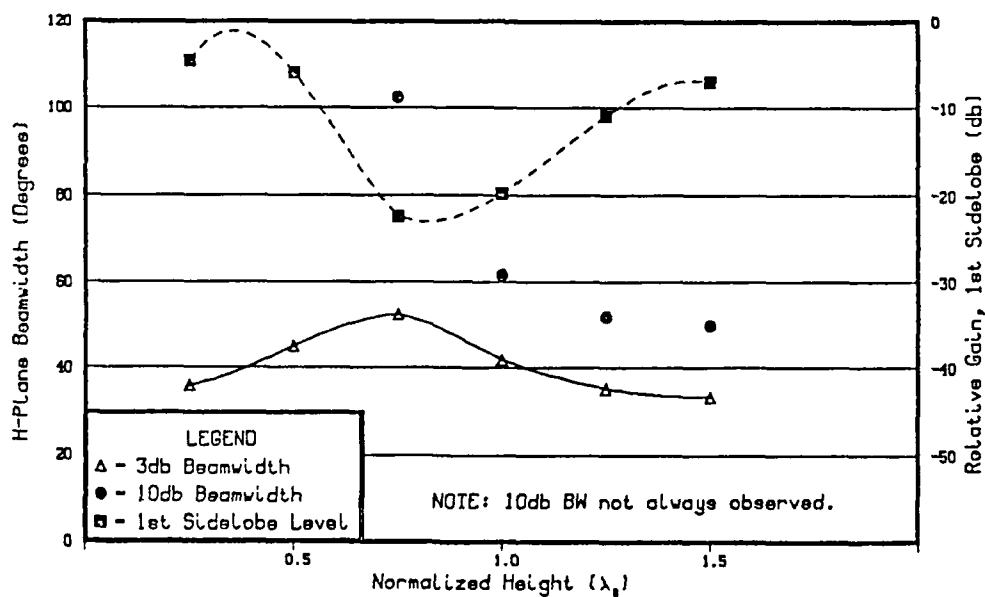


Figure 4.3b H-Plane Effects of Changing H; $L = 4\lambda_0$.

In essence, both theory and experiment suggest that an optimum H/λ_0 may exist in a range which depends on L/λ_0 . For example, Figures A.20 and A.21 show that a range of optimum height appears very narrow - about $1\lambda_0$. On the other hand, for $L = 5\lambda_0$, Figures A.30 and A.31 indicate a relatively broad range of optimum H between $1.0\lambda_0$ and $1.5\lambda_0$.

It is necessary to qualify implications of a so-called optimum. In this study, dimension multiples of $\lambda_0/4$ are used for L and H. Consequently, the interpolation of data points must be judicious. It is especially significant as the relative contributions of other fixed design parameters may change the radiation pattern with synergistic effect.

Due to the noted pattern behavior attributed to changes in height and length, a possible relationship to the length/height ratio (L/H) is explored in Figure 4.4. No discernible affirmation or refutation is immediately evident. Consider $L/H = 4$ for the three modeled antenna lengths. The characteristics of these designs are shown in Table 4.1. These comparative results generally show that a given L/H ratio does not directly determine the radiation patterns. It is reasonable to conclude that L/λ_0 and H/λ_0 independently contribute to the LTSA behavior.

D. FLARE ANGLE

The effects of changing LTSA flare angle (2α) are experienced in two competing phenomena. Consider first that increasing the flare angle in similar traveling wave antennas

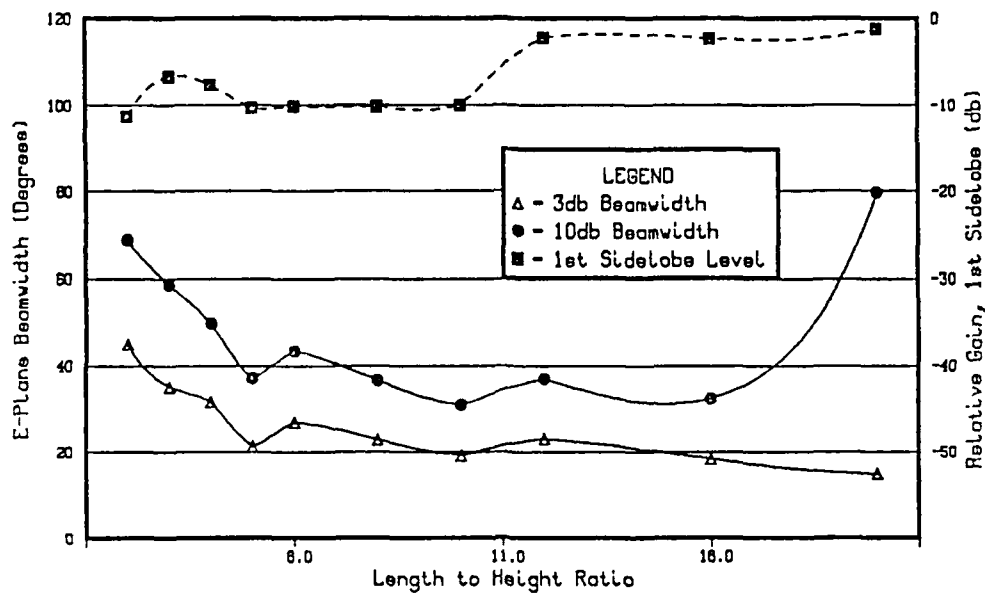


Figure 4.4a E-Plane Effects of Changing the L/H Ratio.

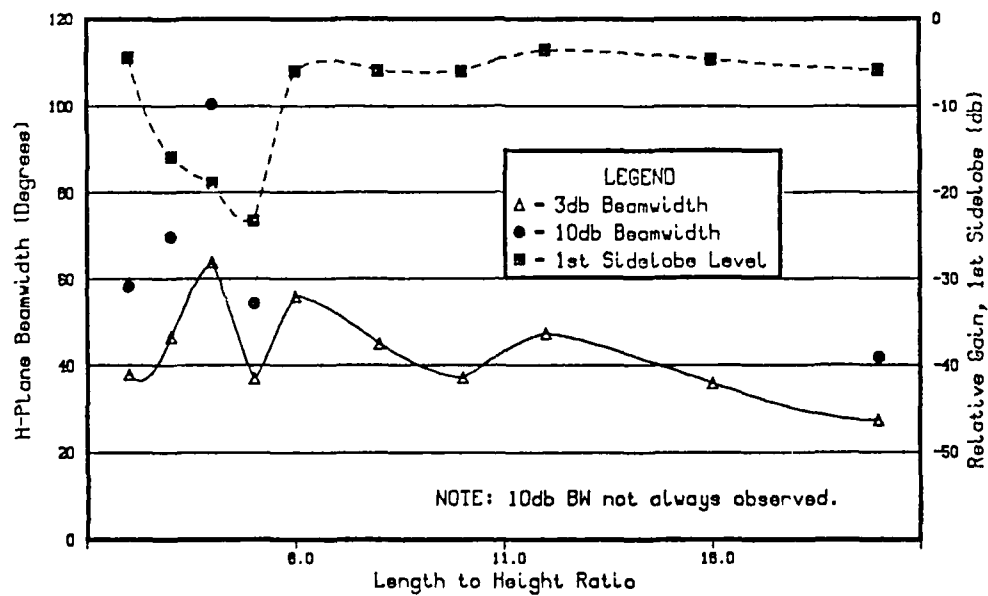


Figure 4.4b H-Plane Effects of Changing the L/H Ratio.

TABLE 4.1 PATTERN BEHAVIOR FOR DESIGNS WITH $L/H = 4$.

L λ_0	H λ_0	HP_E	HP_H	10 db _E BEAMWIDTH	10 db _H BEAMWIDTH	1st Sidelobe E(db) H(db)		Directivity (db)
3	.75	30°	62°	50°	100°	-8	-12	11.5
4	1.0	25°	41°	45°	61°	-9	-19	14.0
5	1.25	18°	31°	36°	47°	-17	-20	16.7

has demonstrated that HP_E is proportional to $1/2a$ and that HP_H is generally insensitive to flare angle changes [Ref. 6]. These results are justified in part by analogy to aperture antennas in which narrower beamwidths are obtained by increasing the aperture size. The second effect for increasing $2a$ is a broader beamwidth which results from an increased phase velocity. This is explained by noting that the fields between the plates are weakened as the plates move farther apart. The phase velocity relates inversely to the energy stored in the fields. Therefore, as the flare angle increases, the slow-wave effect supporting a narrow beam is reduced and the beam widens.

The net effects of these two dynamic factors are summarized in Figure 4.5. It is evident that below 21° the beamwidths are insensitive to flare angle. This contrasts with at least two separate experiments for the fin line LTSA which showed HP_H unaffected by a , but also proved that HP_E is proportional to $1/2a$ [Refs. 6 and 7]. Another departure from empirical studies is the absence of beam symmetry in the predicted patterns. It should be noted that in experiments, the beam symmetry appeared in narrow ranges of flare angle and only for longer antenna lengths. In general, the relative contributions of the cited competing factors seem to offset one another in modeling below 21° .

Above 21° , HP_E increases, possibly due to the phase velocity effect dominating the illumination mechanism. In the H-plane there is a concurrent decrease in HP_H . This may be attributed

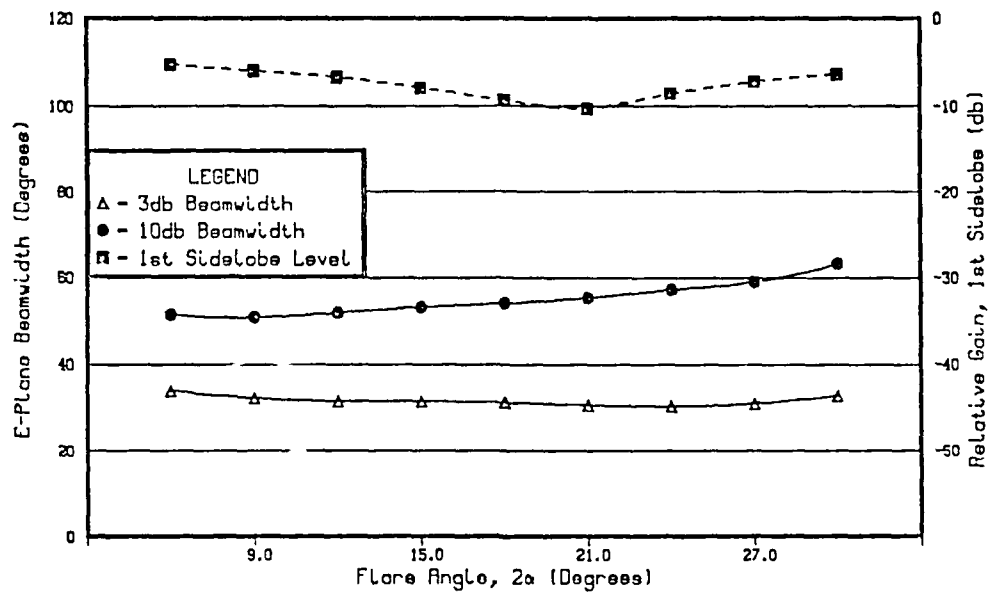


Figure 4.5a E-Plane Effects of Changing Flare angle, 2α .

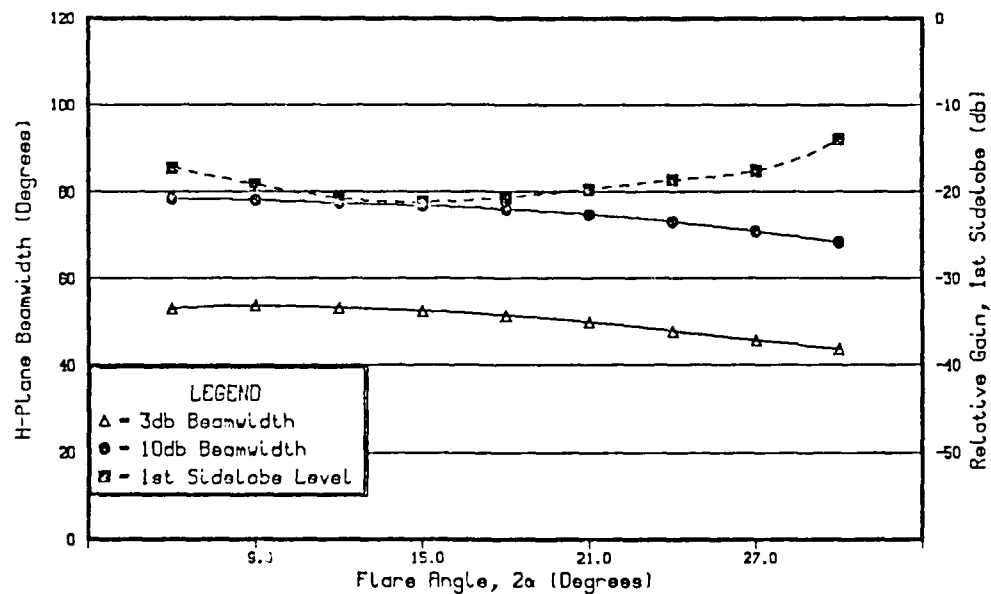


Figure 4.5b H-Plane Effects of Changing Flare Angle, 2α .

to larger current components which move perpendicular to the H-plane as the flare angle increases. Figures C.1 and C.23-C.30 show the modeled current distributions for respective flare angles. Using Janaswamy's model, surface impedance does not change and the current distribution appears to change only slightly as a function of flare angle. However, to resolve this question in further detail requires more accurate modeling of the current distribution.

As a matter for design consideration, the radiation patterns for different flare angles are plotted in Figures A.32-A.39. Although these designs have approximately equal directivity, the high sidelobes are not necessarily acceptable. For this reason (as Figure 4.5 also indicates) a range of flare angles between 19° and 22° appears to be best, given the same set of other design parameters.

E. SUBSTRATE FACTORS

As discussed previously, the plates are treated as imperfect conductors in the dielectric supported antenna. The surface impedance is a function of dielectric thickness (d) and the relative permittivity (ϵ_r). A modest range of dielectric designs were modeled and the respective predicted radiation patterns are presented in Figures A.40-A.48.

It is first noted that increasing " d " noticeably reduces the large E-plane backlobe and slightly increases the relative gain of the H-plane backlobe. This is a point of interest because

backlobes are a minor disagreement between the LTSA experimental and theoretical models. The predicted results suggest that the discrepancy is due to the manner in which Janaswamy's model approximates the effects of the dielectric substrate [Ref. 1].

The LTSA behavior as a function of substrate thickness is characterized in Figure 4.6. It is observed that the first sidelobes increase slightly with d . The E-plane first sidelobe is relatively large.

The primary effect of increasing d is the HP_H improvement. Between $d = .01\lambda_0$ and $.05\lambda_0$, HP_H decreases by more than 30%. The E-plane beam is equally well-formed but it appears unaffected except where it suddenly narrows by 30% between $d = .04\lambda_0$ and $.05\lambda_0$. Approximately 2.2 db improvement in directivity is achieved by increasing d from $.021\lambda_0$ to $.05\lambda_0$.

The noted behavior is supported by theory which allows that a dielectric material typically slows the currents in an endfire producing surface wave antenna. As the phase velocity decreases a corresponding narrower beam width is produced. The concurrent increase in current is noted by comparisons among Figure C.1 and C.31-C.36. Coincident with the cited HP_E decrease, Figures C.35c and C.36c show that the transmission mode current at the outer edge along H does not taper off as noted in most other modeled designs. Because the calculated current distribution is not accurate, it cannot be ascertained if this is a meaningful observation or a numerical aberration.

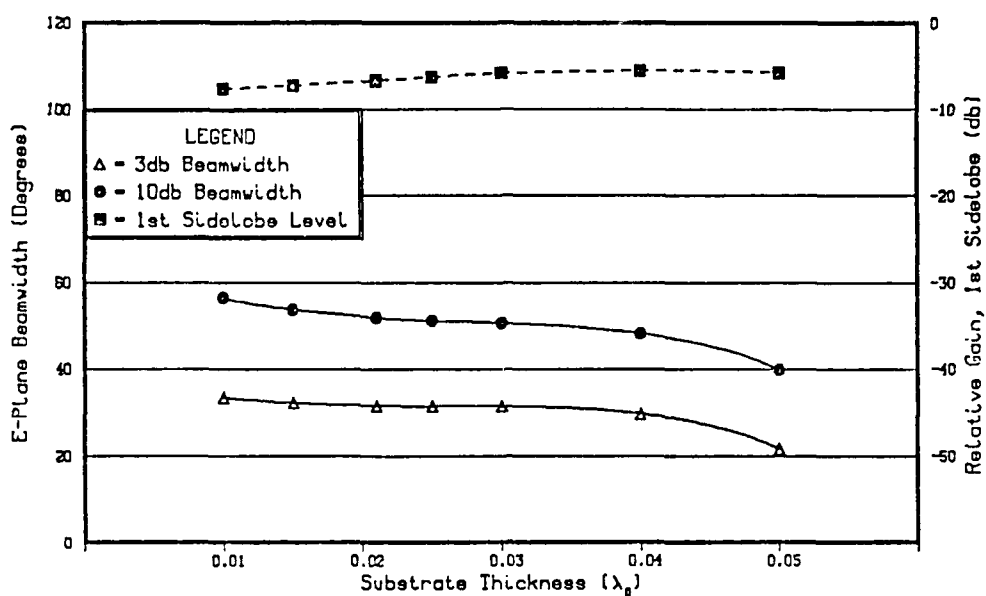


Figure 4.6a E-Plane Effects of Changing Substrate Thickness.

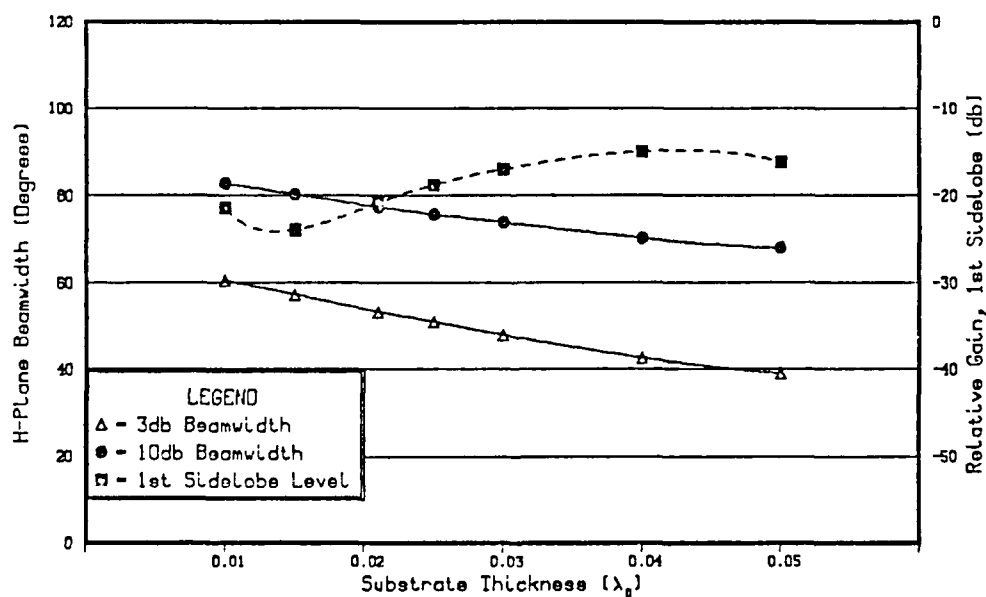


Figure 4.6b H-Plane Effects of Changing Substrate Thickness.

The other substrate parameter to consider is the relative dielectric constant (ϵ_r). Figure 4.7 depicts a proven insensitivity of pattern behavior to changes in ϵ_r between 2.33 and 10.5. (For detailed corroboration, see Figures A.46-A.48 and C.37-C.39.) Simply stated, this occurs because the surface impedance only depends on d when the substrate is electrically thin, i.e., when $(\epsilon_r - 1)d / \lambda_0 \leq .2$. In other words, for small d , the surface impedance equation simplifies as

$$Z_s = \frac{\eta_0}{\sqrt{\epsilon_r}} \tan(k_0 d \sqrt{\epsilon_r}) \approx \frac{\eta_0}{\sqrt{\epsilon_r}} k_0 d \sqrt{\epsilon_r} = \eta_0 k d \quad (4.2)$$

This finding is commercially relevant because the cost of substrate materials is a factor in building these relatively inexpensive antennas.

F. SUMMARY OF RADIATION PATTERN EFFECTS

The general purpose of modeling the LTSA is to gain insight and apply the necessary theory to understand its behavior. Equally significant, however, is the specific purpose, which is to provide useful guidance for the design and application of this antenna. Based on the credibility of the theoretical model, highlights of the parametric analysis deserve reiteration. Data already exists for studies of LTSA's with large lengths. Modeled herein are design lengths of $3\lambda_0$, $4\lambda_0$ and $5\lambda_0$. The results show that directivity is directly and consistently proportional to the antenna length. The design process may commence by selecting an appropriate L for a desired directive gain.

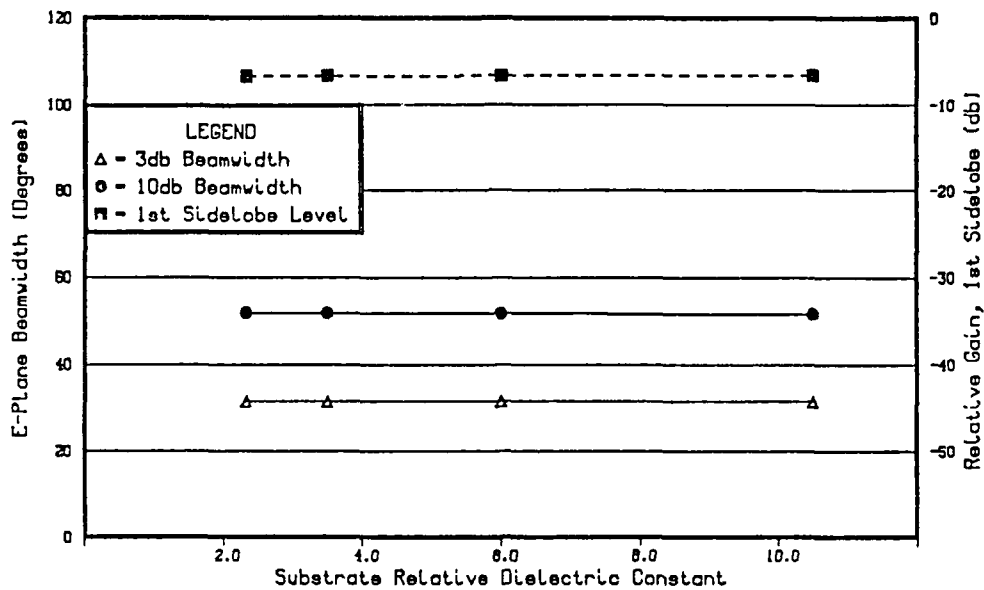


Figure 4.7a E-Plane Effects of Changing Substrate Permittivity.

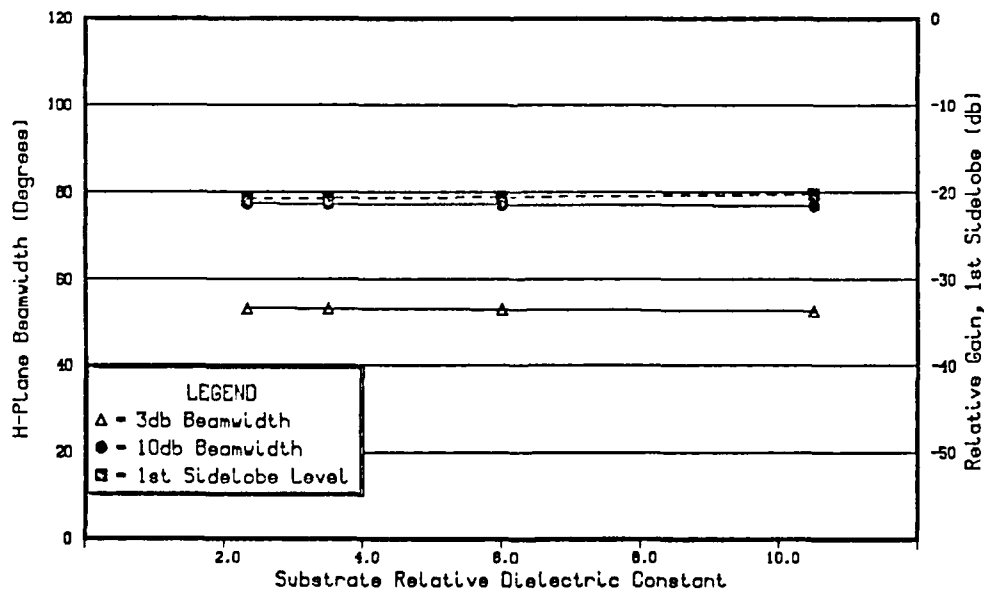


Figure 4.7b H-Plane Effects of Changing Substrate Permittivity.

The applied model uniquely provides an aid to investigate, the height factor. A key finding is that the empirically observed optimum range of H/λ_0 is also evident in the predicted pattern behavior. Results further show that while the range of an optimum H/λ_0 does depend on antenna length, the pattern itself depends on L/λ_0 and H/λ_0 independently.

For the modeled designs of flare angle between 6° and 30° , two mechanisms appear to cancel the effects of one another. Consequently, the directivity is virtually unaffected by the flare angle. Given other design parameters the same, flare angles chosen between 19° and 22° give the best sidelobe suppression.

Substrate thickness is the dominant contribution to surface impedance. For electrically thin substrate, ϵ_r has no effect. In the modeled range of d , the H-plane beam narrows about 5° per $.01 \lambda_0$. In the otherwise unaffected E-plane, the backlobe is suppressed below -10 db for $d \geq .03 \lambda_0$ and the main beam suddenly narrows between $d = .04 \lambda_0$ and $.05 \lambda_0$. Although beam sharpening can be done with thicker substrate, it may be relatively costly and impractical.

V. CONCLUSIONS OF MODELING STUDY

The scope of any analysis includes a purpose, supporting theory and a demonstrative application or proof. For the LTSA, the purpose is to develop a model which accurately predicts its behavior. Since experiments and applications began in 1982, such a model has become an important goal in the antenna community. The supporting theory advanced here is to use the MM to solve the reaction integral equation. Thereafter, the far fields are computed once the current distribution is known. The primary limitation to exploiting this model is the availability of CPU time required for rigorous MM solutions. Using this model, the contribution of this study is a parametric analysis of 39 LTSA designs. The resulting modeled behavior generally agrees with known empirical data. Consequently, the analysis not only is consistent with applied theory but also is useful for the LTSA design process.

The presentation of ideas for review begins with the MM technique. As detailed in Chapter 2, MM makes it possible and practical to solve for an unknown function, $f(x)$, in an equation which does not have a closed form solution. The original equation is essentially transformed to an equivalent matrix equation which is then solved by conventional methods. There are two major considerations in MM. Foremost is the choice of basis functions, which ideally are selected to

faithfully represent the true $f(x)$. However, since the form of $f(x)$ is often unknown, selecting basis functions in electromagnetic applications is usually a result of trial and error. This alludes to the second key aspect of MM. CPU time may be scarce or expensive. The two factors affecting the economy of those resources are rate of convergence and desired precision in the solution. A good (or fortuitous) choice of basis functions improves the rate of convergence. The matrix size (hence CPU cost) grows geometrically with the extent of required accuracy.

The present model employs the popular Piecewise Sinusoidal-Galerkin technique. The main reason for this choice is that it helps to reduce the CPU time involved in computing the elements of the impedance matrix. Furthermore, it has the potential for reducing the number of unknowns for a given problem. A convergent solution for the radiation pattern (far-field) is obtained with four to five segments per wavelength. An accurate solution for current distribution (near-field) entails much more CPU time because more segments are required for convergence. The model is rigorous for the air dielectric case and approximate if the LTSA has an electrically thin dielectric substrate. To precisely include the dielectric in the algorithm contributes little more to the solution than increased CPU time.

In summation of the parametric analysis, there are several conclusions which are valid for the ranges of modeled

design parameters. Moreover, it is reasonable to extrapolate behavior based on these significant modeling results:

- * An appropriate antenna length is best suggested by the initial determination of required directivity.
- * For a given length there is a range of optimum height which will contribute to a well formed narrow beam.
- * Although the flare angle has no effect on directivity in a given design, there is a flare angle bracket within which side-lobes are ameliorated.
- * Substrate thickness has a significant and inversely proportional relationship to H-plane beamwidth.
- * For electrically thin substrate, the relative dielectric constant has no effect on the radiation pattern.

Future design and development of the LTSA will be enhanced by this research. Having successfully modeled the pattern behavior, the next step is to obtain a convergent solution for the LTSA current. Such a goal will probably await lower cost microprocessing when improved accuracy of MM techniques is more cost effective. In the interim, it appears that the concept, the ideas and the algorithm used in this study may be equally effective in the analysis of similar antennas.

APPENDIX A LTSA RADIATION PATTERNS

The parametric analysis of radiation patterns begins with the known empirical design which was accurately modeled (Figure A.1) using the following specifications:

- * Feed Gap = $.02\lambda_0$
- * Length = $3\lambda_0$
- * Height = $.9\lambda_0$
- * Flare Angle = 12°
- * Substrate Thickness = $.021\lambda_0$
- * Substrate Relative Dielectric Constant = 2.33

The study of these parameters and their effects is based on Figures A.2-A.48 which show the computed radiation pattern for each case. Each computed pattern is templated with the reference pattern to illustrate the immediate effects of the design change.

Since the theoretical model uses a strip dipole source, the feed dipole length is varied as a design parameter but the feed gap is fixed at $.021\lambda_0$. The comparative effects of this design parameter (Figures A.2-A.4) serve to help understand the source model rather than the antenna itself.

Figures A.5-A.16 show calculated patterns for three different antenna lengths of $3\lambda_0$, $4\lambda_0$ and $5\lambda_0$. In each case, the height of the antenna was changed in the range $.25\lambda_0$ - $1.5\lambda_0$. These same designs are given a different perspective

in Figures A.17-A.31 which show the effects of changing height for given antenna lengths.

The range of flare angles which were modeled is 6° to 30° . Each modeled design is compared with the original design (12°) in Figures A.32-A.39.

The surface impedance is determined by both the substrate thickness and permittivity. Varying these parameters results in radiation patterns shown in Figures A.40-A.48.

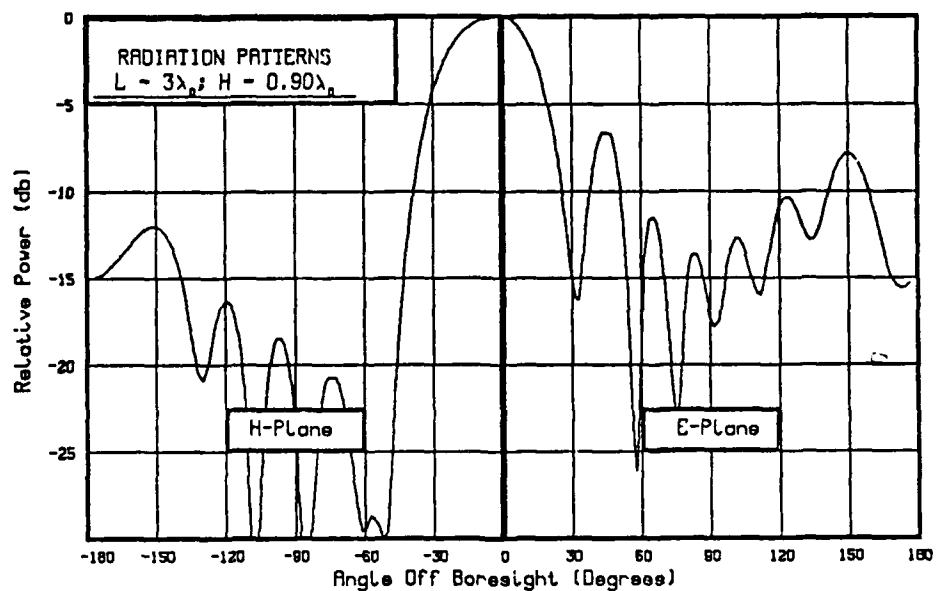


Figure A.1 Predicted Patterns for a Known Empirical Design.

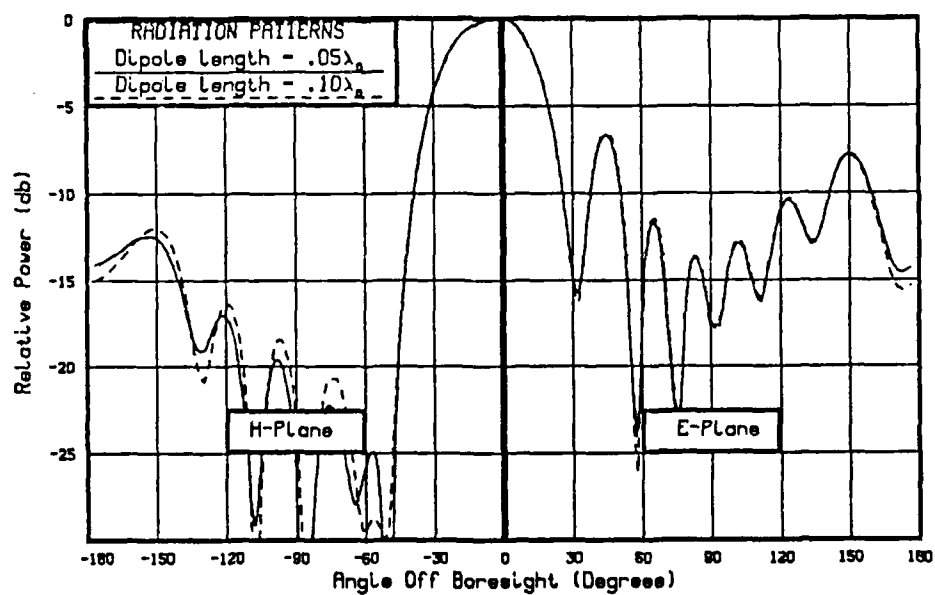


Figure A.2 Effects of Decreasing Feed Dipole Length to $.05\lambda_0$.

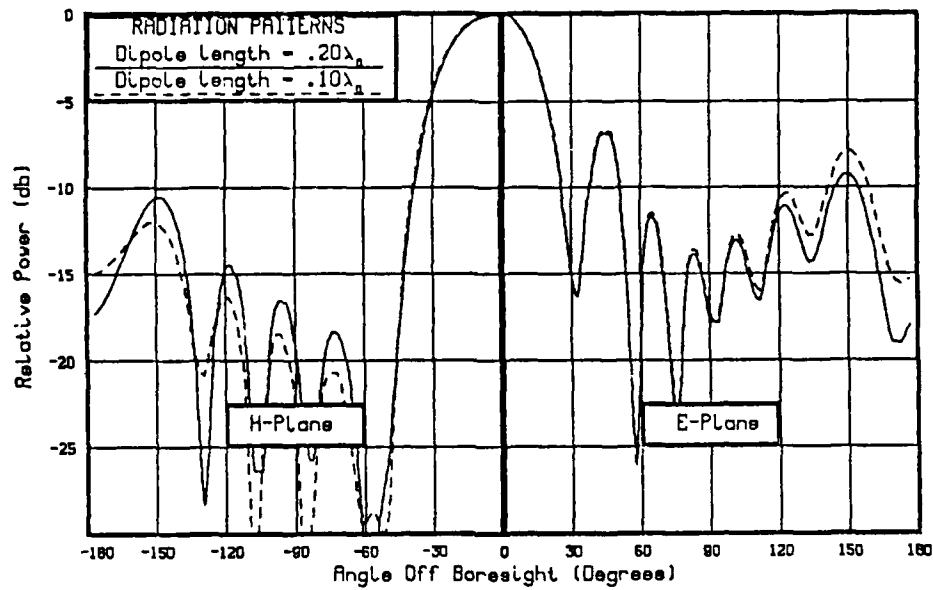


Figure A.3 Effects of Increasing Feed Dipole Length to $0.20\lambda_0$.

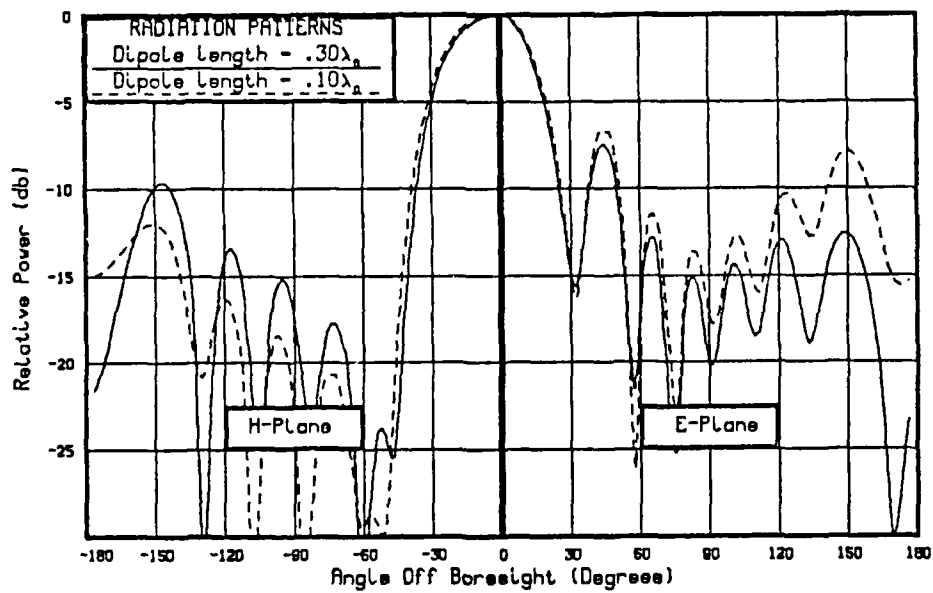


Figure A.4 Effects of Increasing Feed Dipole Length to $0.30\lambda_0$.

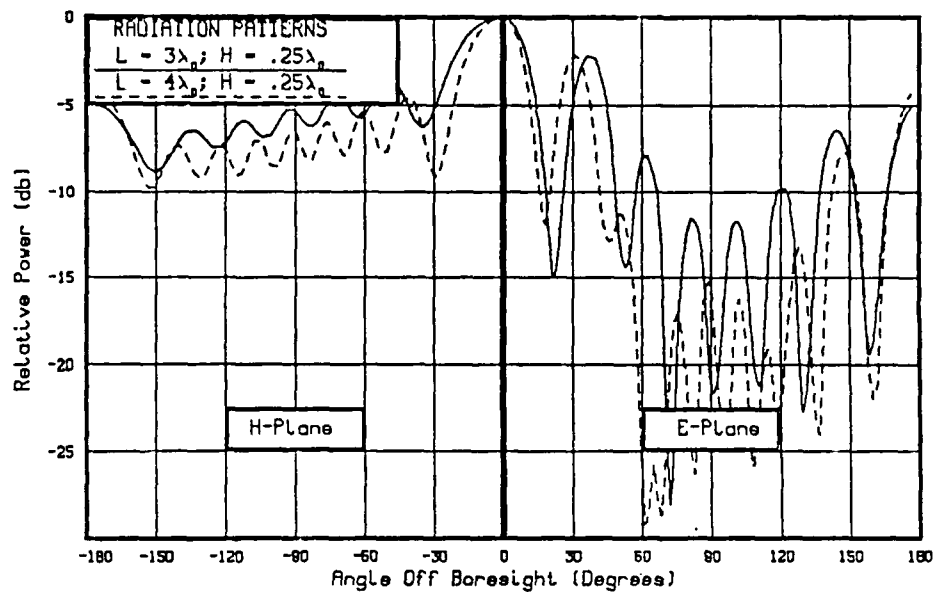


Figure A.5 Effects of Decreasing Length to $3\lambda_0$ for $H = .25\lambda_0$.

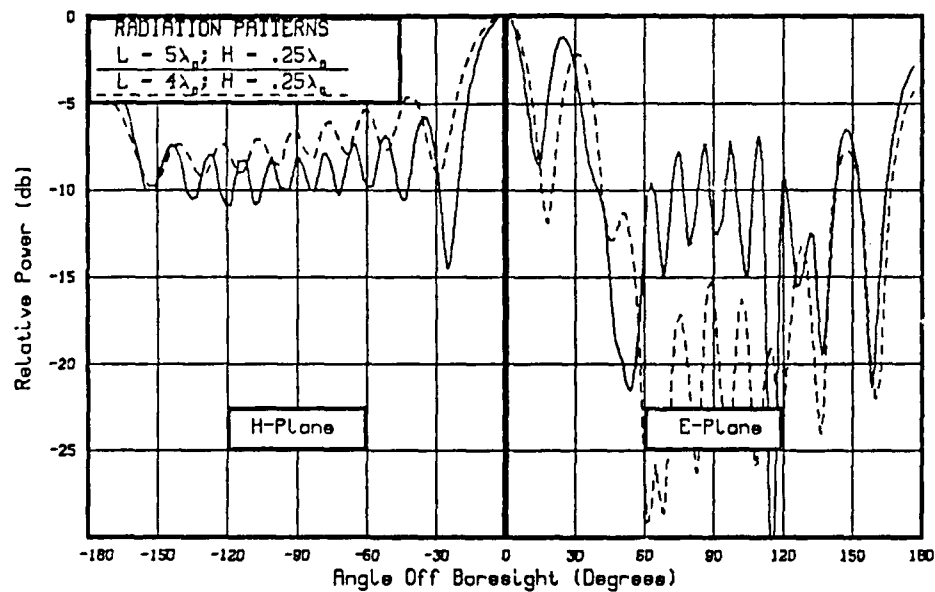


Figure A.6 Effects of Increasing Length to $5\lambda_0$ for $H = .25\lambda_0$.

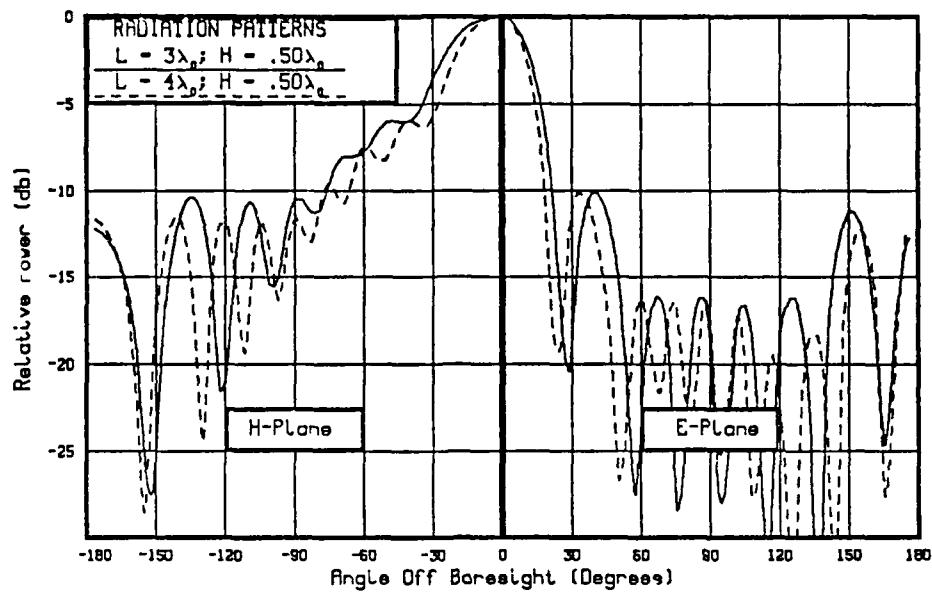


Figure A.7 Effects of Decreasing Length to $3\lambda_0$ for $H = .50\lambda_0$.

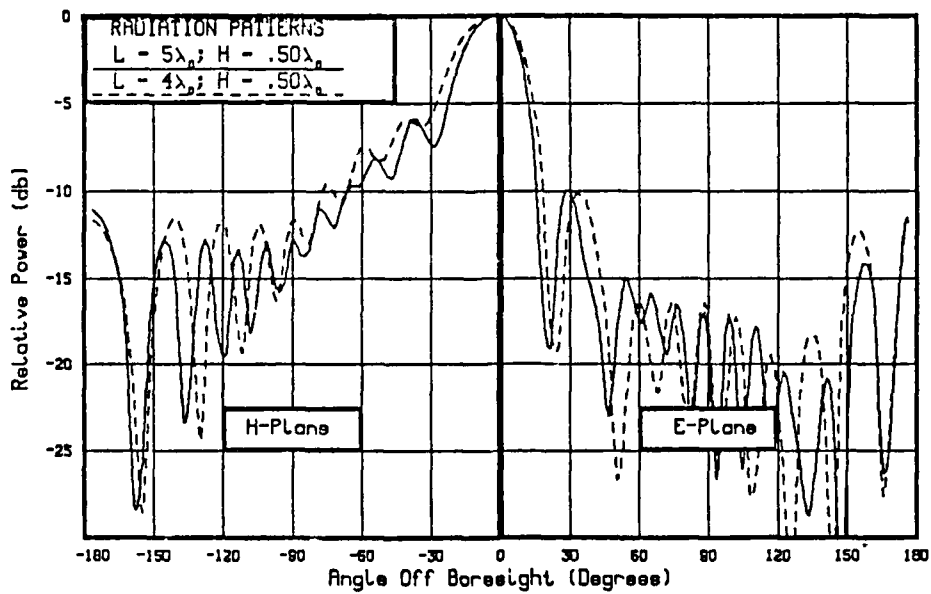


Figure A.8 Effects of Increasing Length to $5\lambda_0$ for $H = .50\lambda_0$.

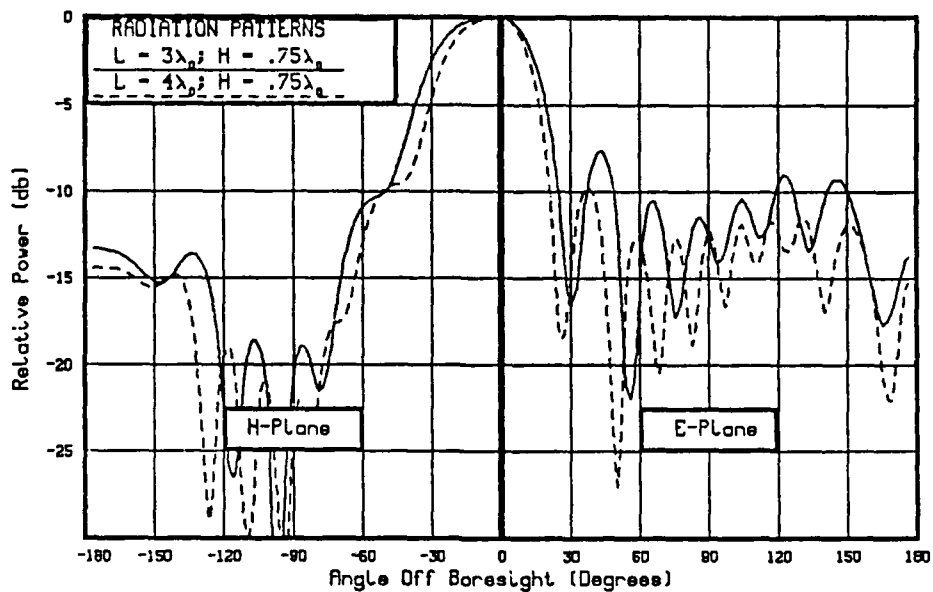


Figure A.9 Effects of Decreasing Length to $3\lambda_0$ for $H = .75\lambda_0$.

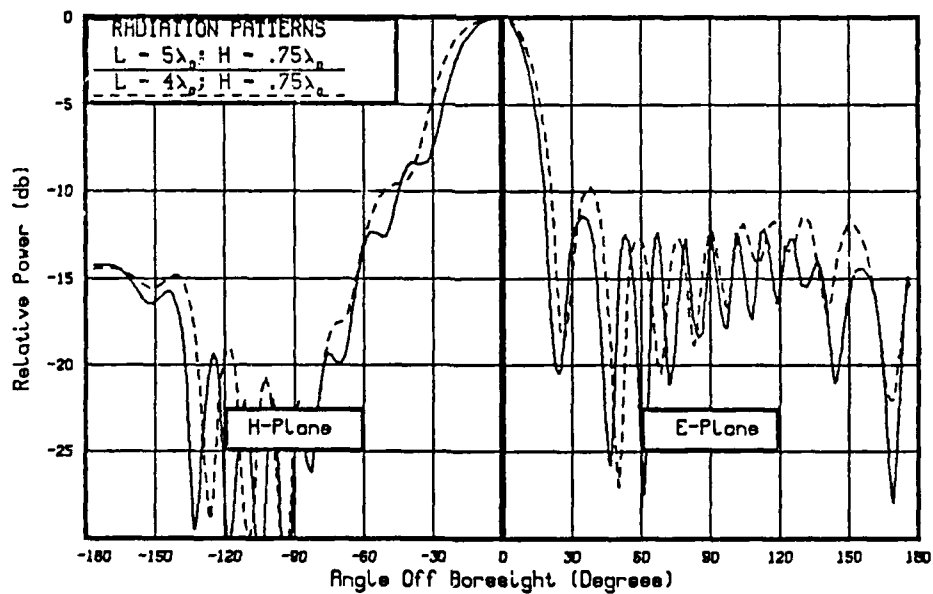


Figure A.10 Effects of Increasing Length to $5\lambda_0$ for $H = .75\lambda_0$.

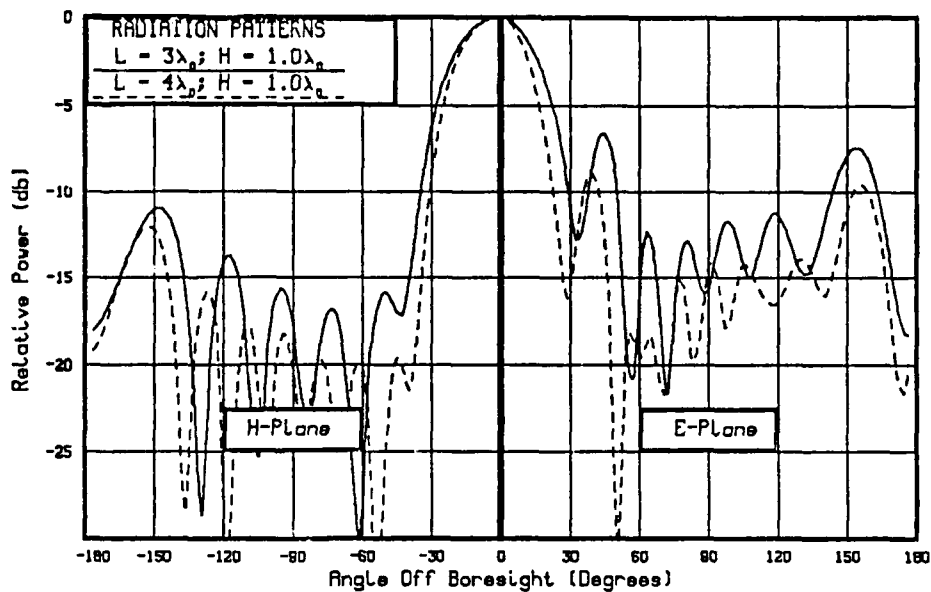


Figure A.11 Effects of Decreasing Length to $3\lambda_0$ for $H=1.0\lambda_0$.

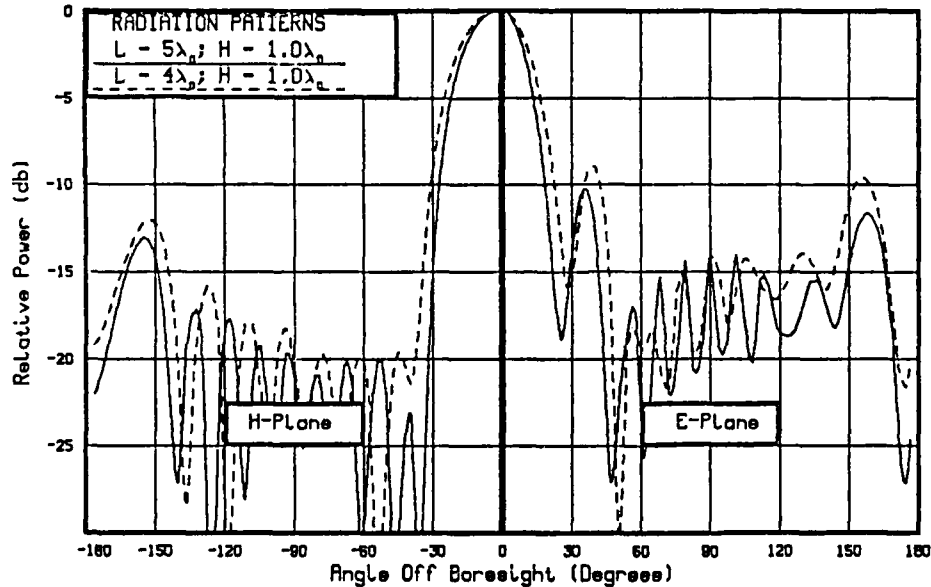


Figure A.12 Effects of Increasing Length to $5\lambda_0$ for $H=1.0\lambda_0$.

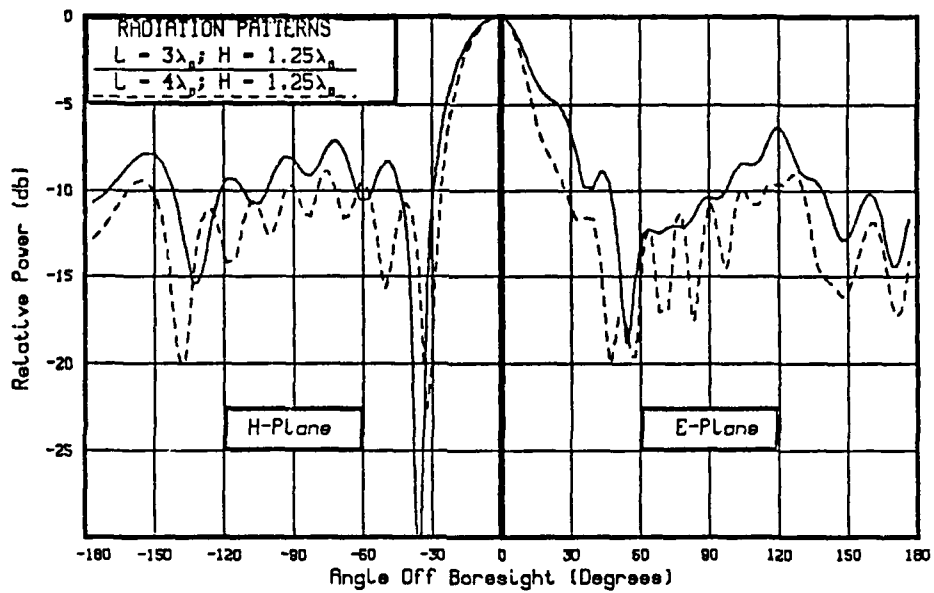


Figure A.13 Effects of Decreasing Length to $3\lambda_0$ for $H=1.25\lambda_0$.

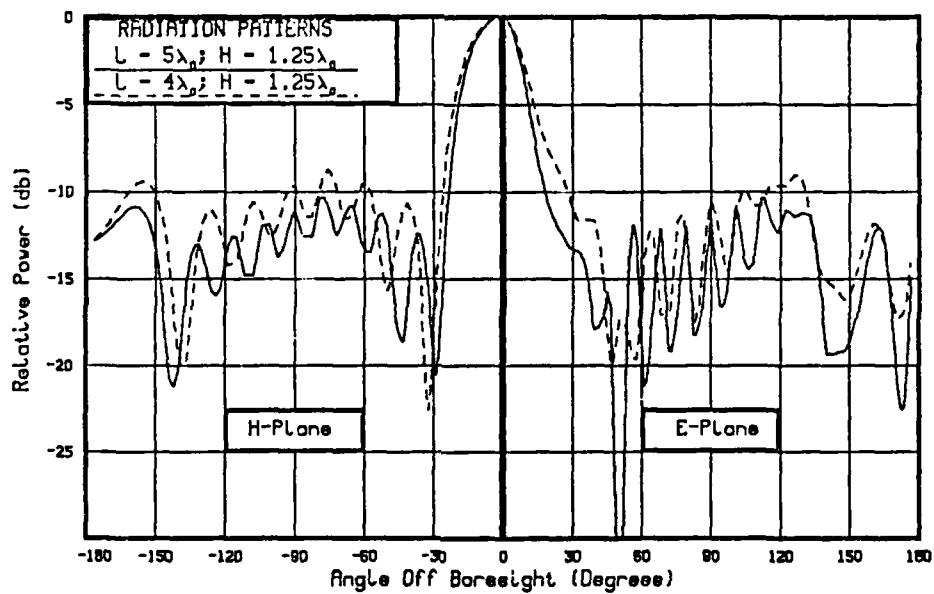


Figure A.14 Effects of Increasing Length to $5\lambda_0$ for $H=1.25\lambda_0$.

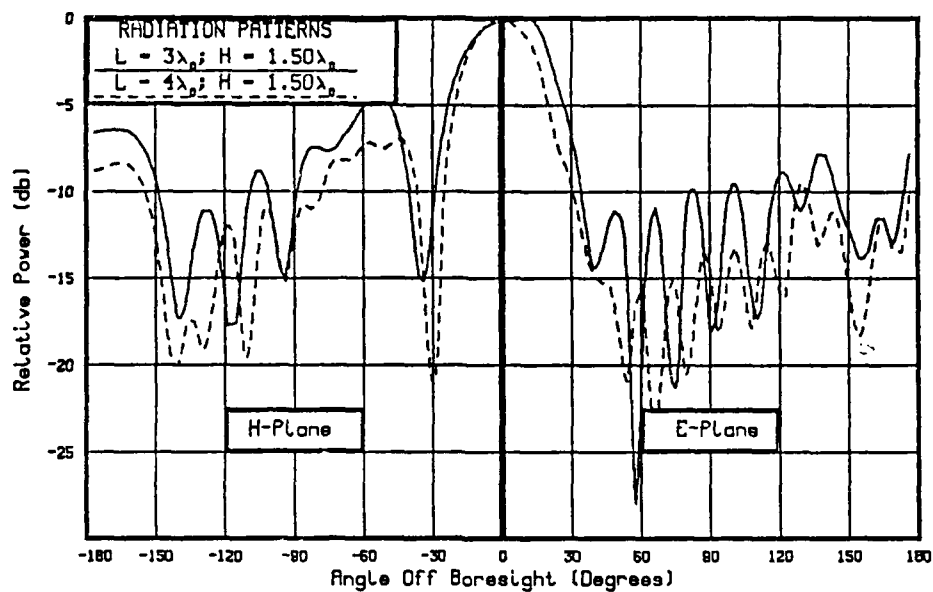


Figure A.15 Effects of Decreasing Length to $3\lambda_0$ for $H=1.50\lambda_0$.

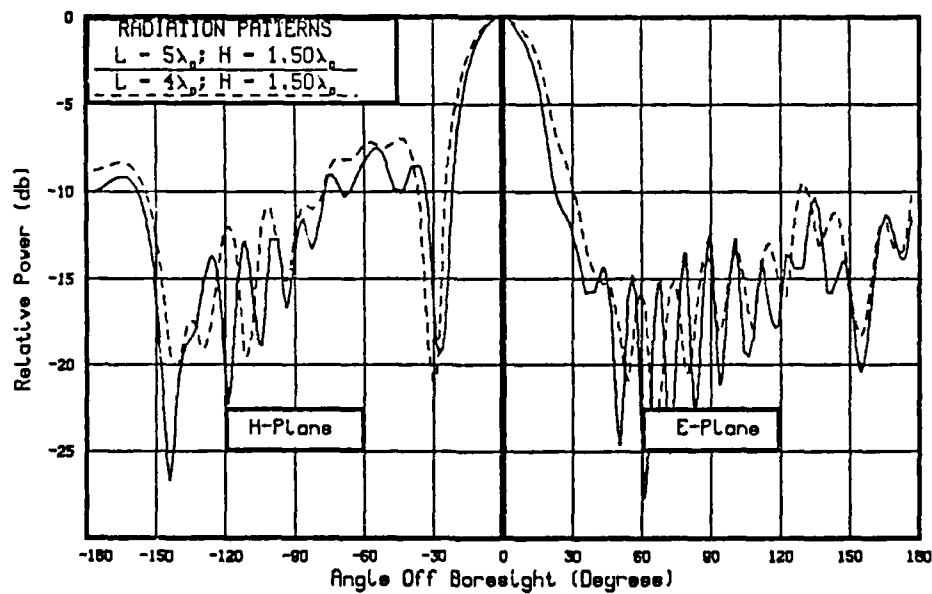


Figure A.16 Effects of Increasing Length to $5\lambda_0$ for $H=1.50\lambda_0$.

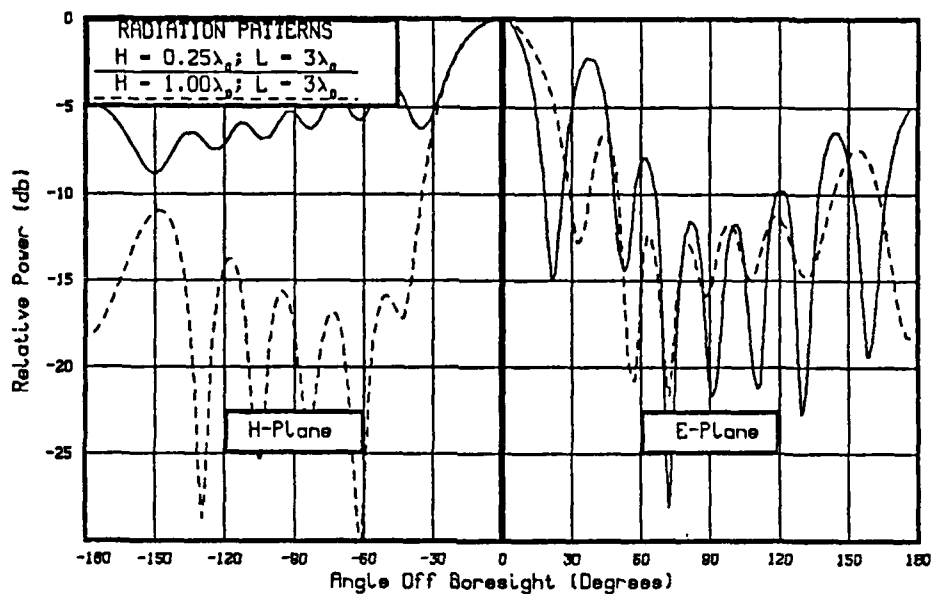


Figure A.17 Effects of Decreasing Height to $.25\lambda_0$ for $L=3\lambda_0$.

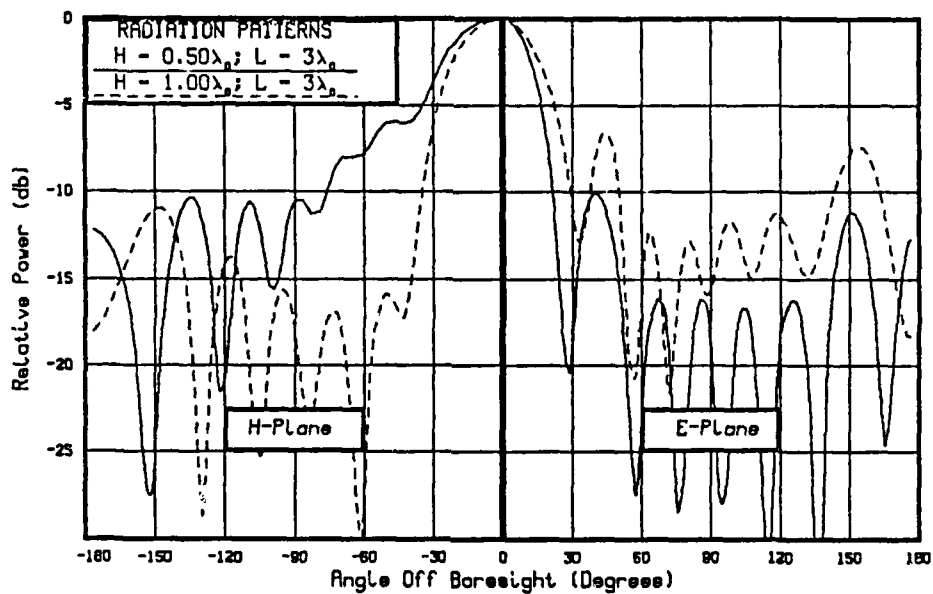


Figure A.18 Effects of Decreasing Height to $.50\lambda_0$ for $L=3\lambda_0$.

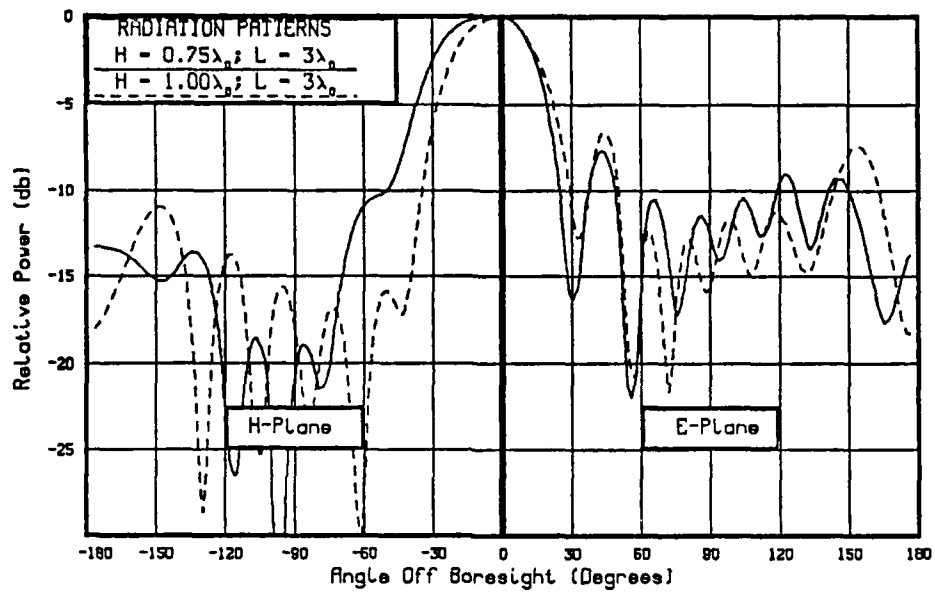


Figure A.19 Effects of Decreasing Height to $.75\lambda_0$ for $L=3\lambda_0$.

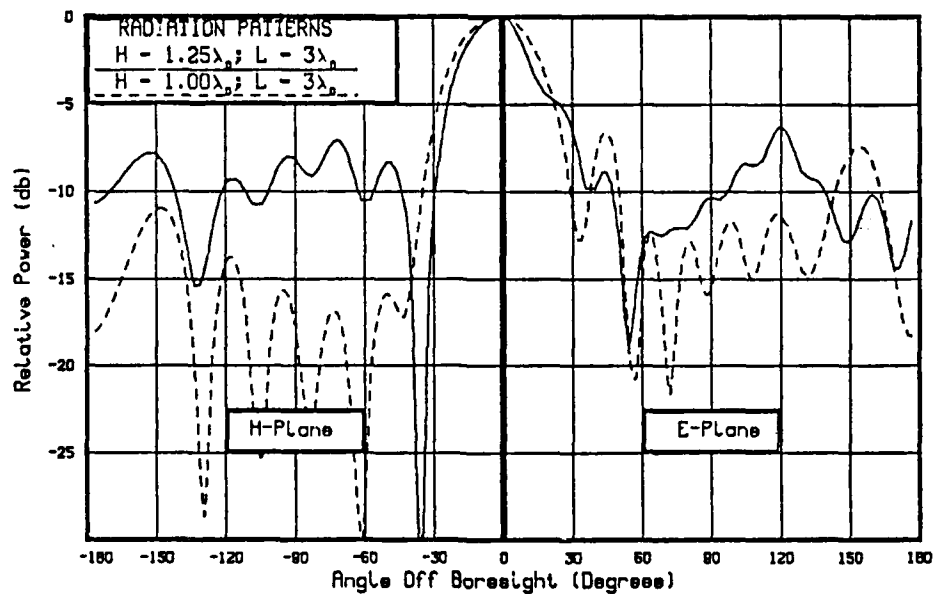


Figure A.20 Effects of Increasing Height to $1.25\lambda_0$ for $L=3\lambda_0$.

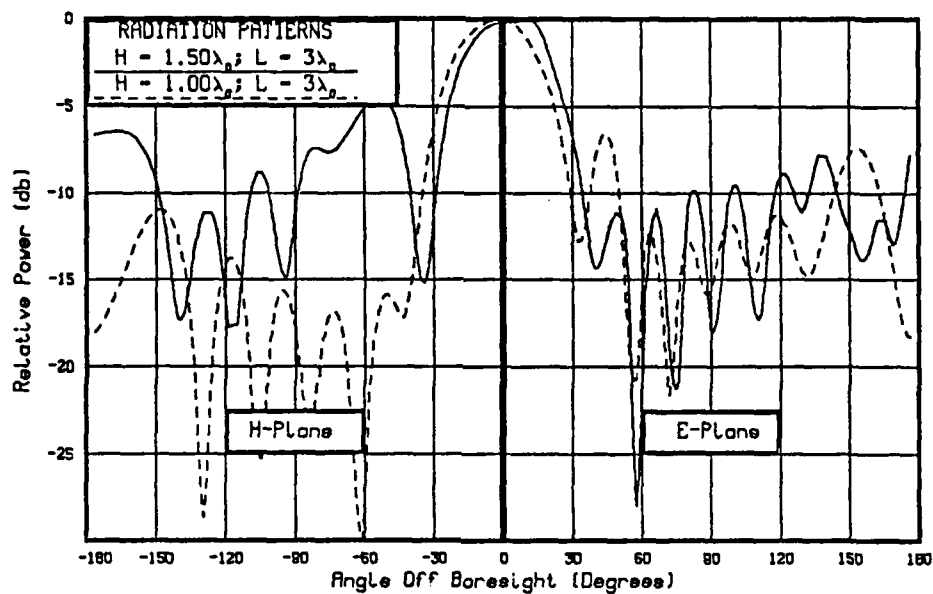


Figure A.21 Effects of Increasing Height to $1.50\lambda_0$ for $L=3\lambda_0$.

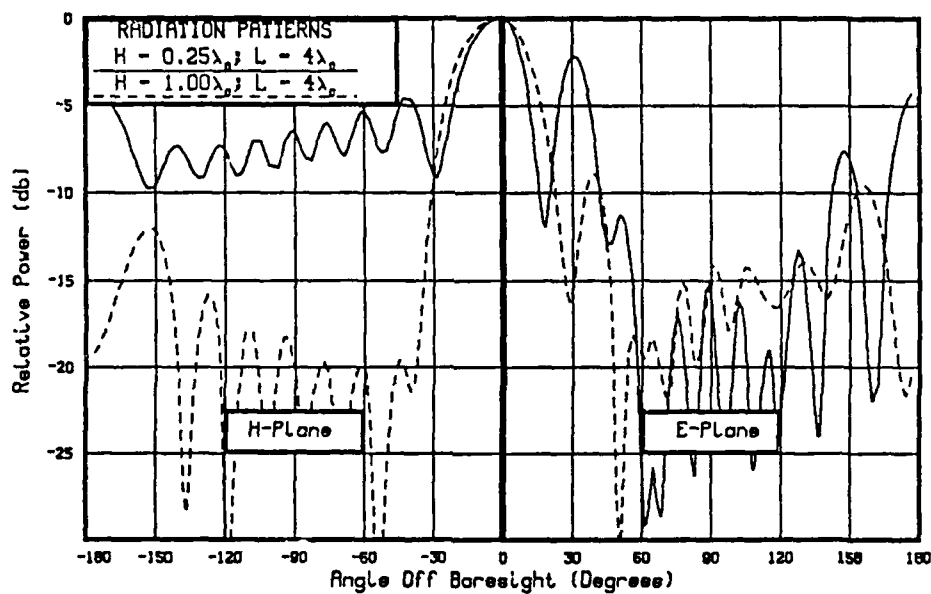


Figure A.22 Effects of Decreasing Height to $.25\lambda_0$ for $L=4\lambda_0$.

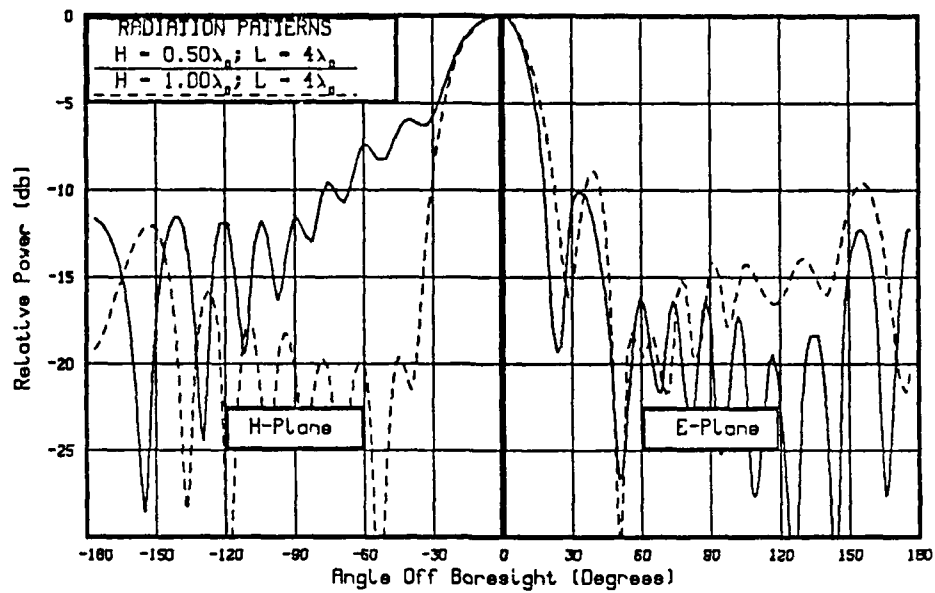


Figure A.23 Effects of Decreasing Height to $.50\lambda_0$ for $L=4\lambda_0$.

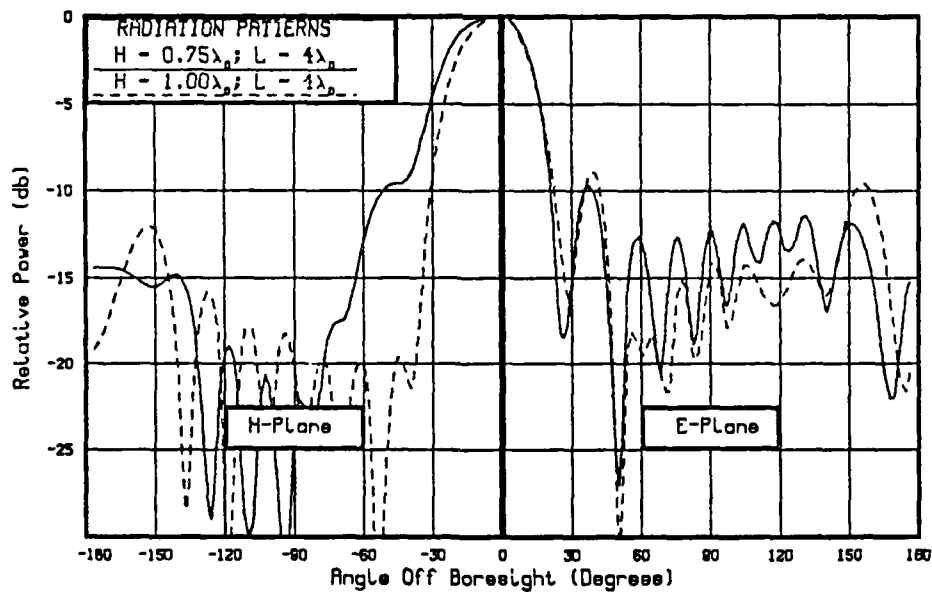


Figure A.24 Effects of Decreasing Height to $.75\lambda_0$ for $L=4\lambda_0$.

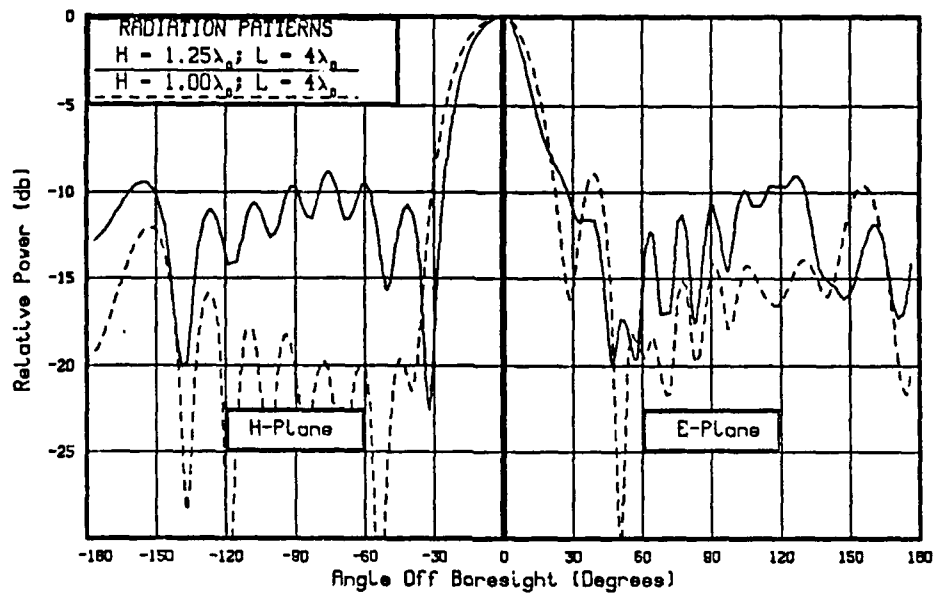


Figure A.25 Effects of Increasing Height to $1.25\lambda_0$ for $L=4\lambda_0$.

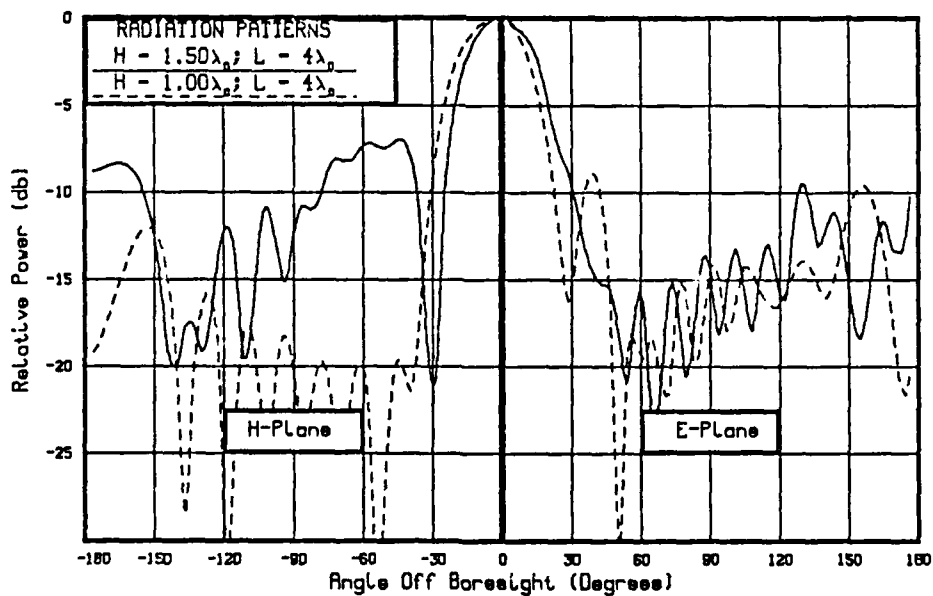


Figure A.26 Effects of Increasing Height to $1.50\lambda_0$ for $L=4\lambda_0$.

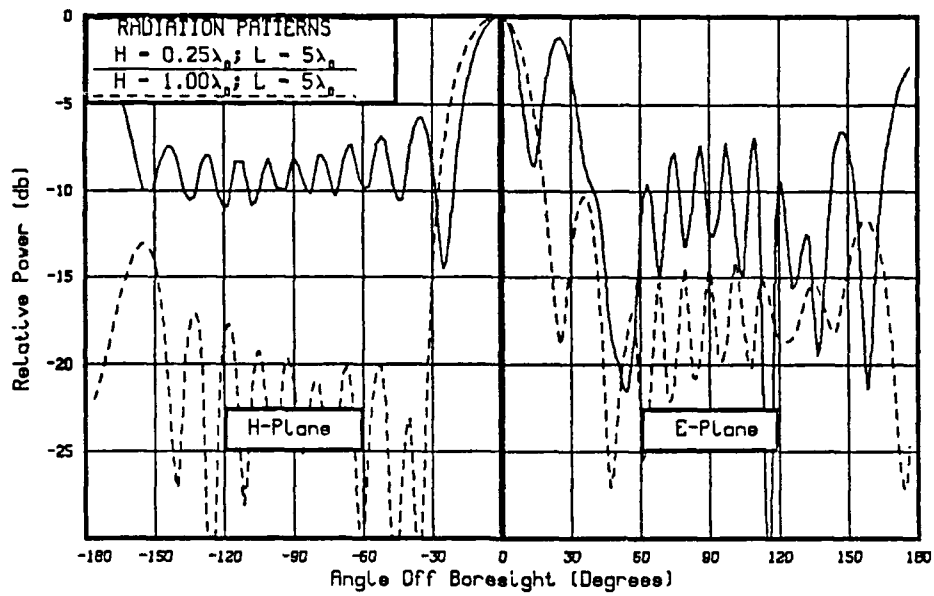


Figure A.27 Effects of Decreasing Height to $.25\lambda_0$ for $L=5\lambda_0$.

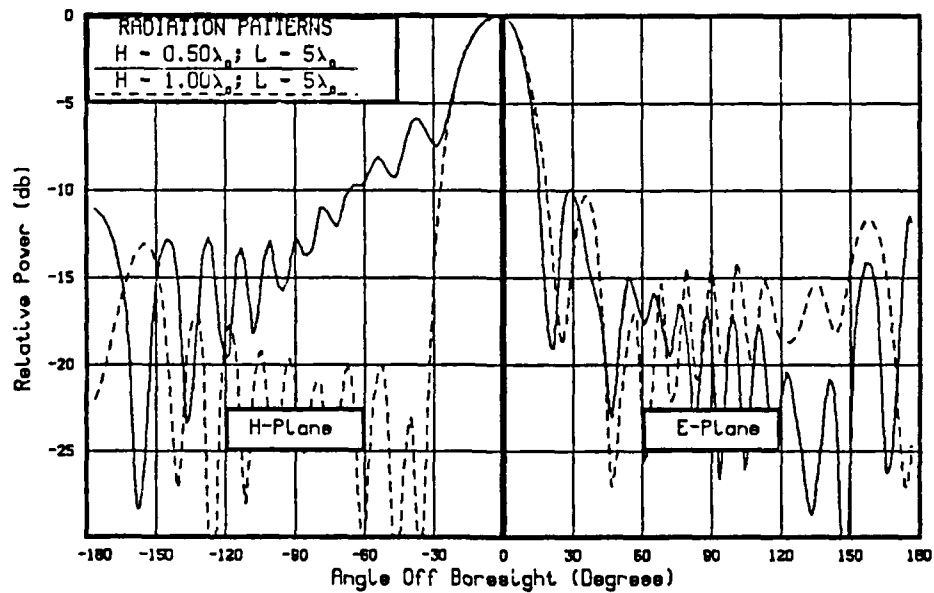


Figure A.28 Effects of Decreasing Height to $.50\lambda_0$ for $L=5\lambda_0$.

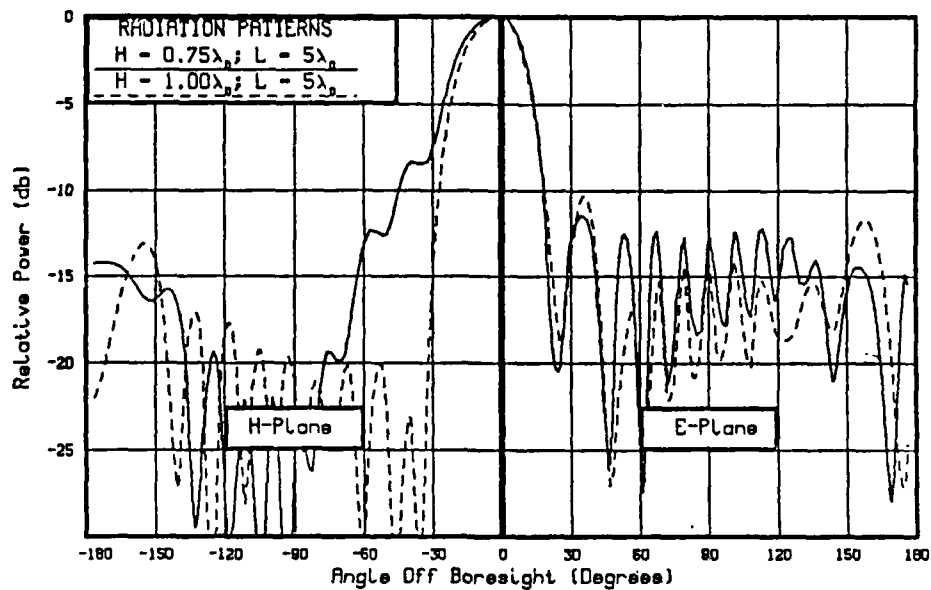


Figure A.29 Effects of Decreasing Height to $.75\lambda_0$ for $L=5\lambda_0$.

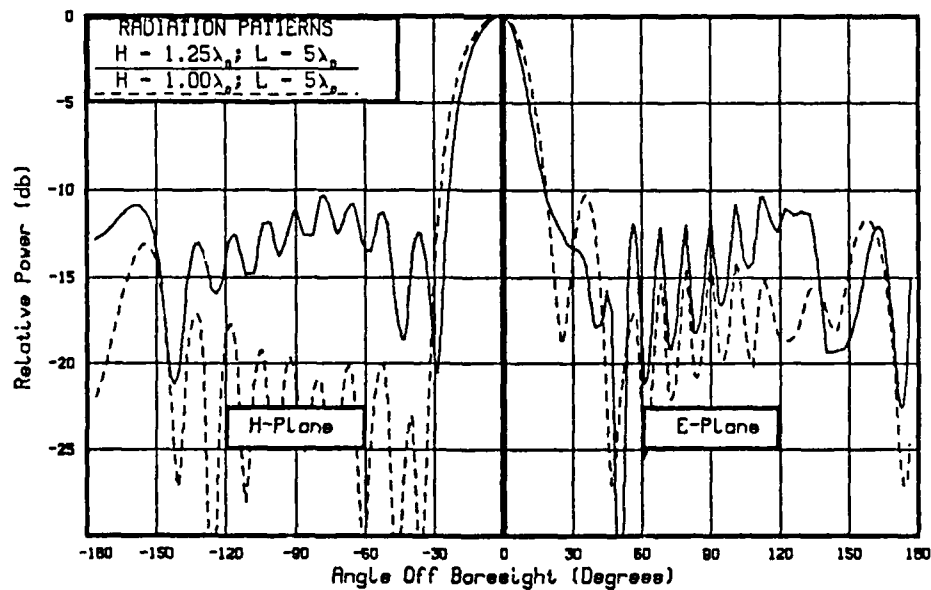


Figure A.30 Effects of Increasing Height to $1.25\lambda_0$ for $L=5\lambda_0$.

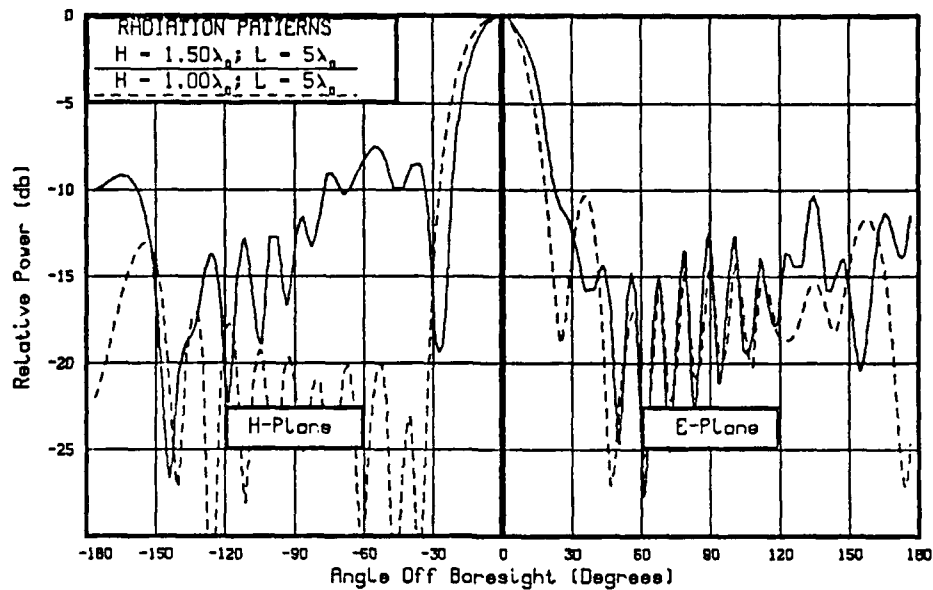


Figure A.31 Effects of Increasing Height to $1.50\lambda_0$ for $L=5\lambda_0$.

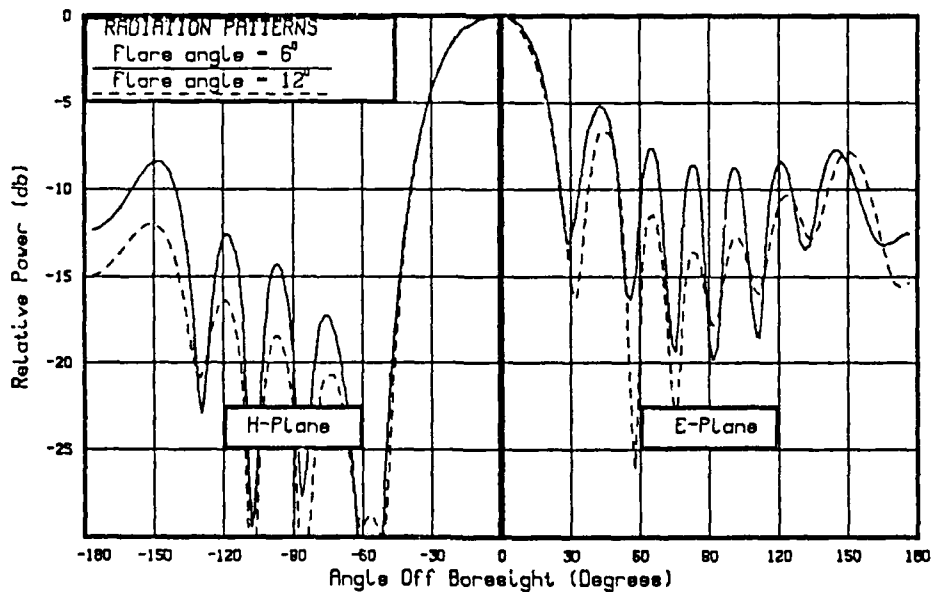


Figure A.32 Effects of Decreasing Flare Angle to 6° .

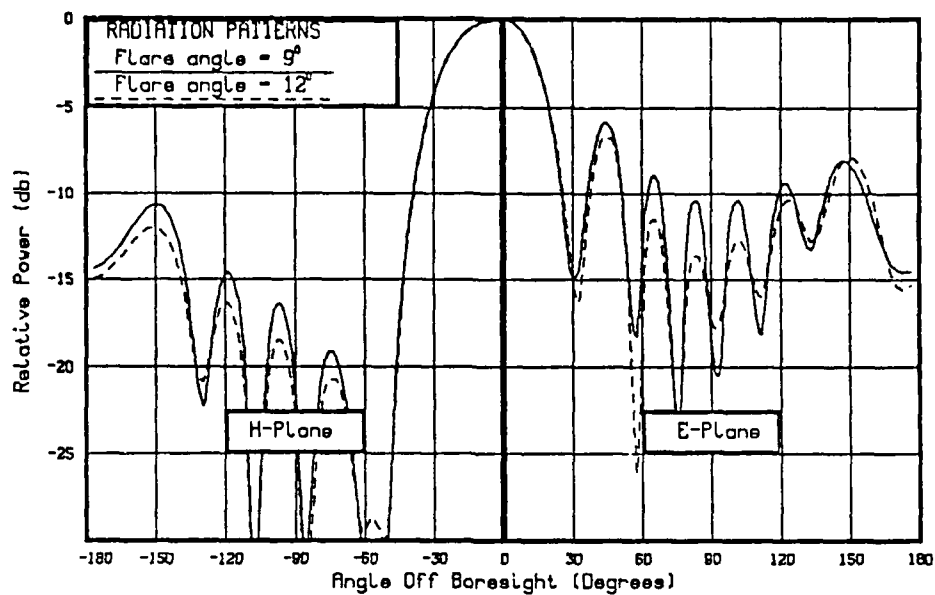


Figure A.33 Effects of Decreasing Flare Angle to 9° .

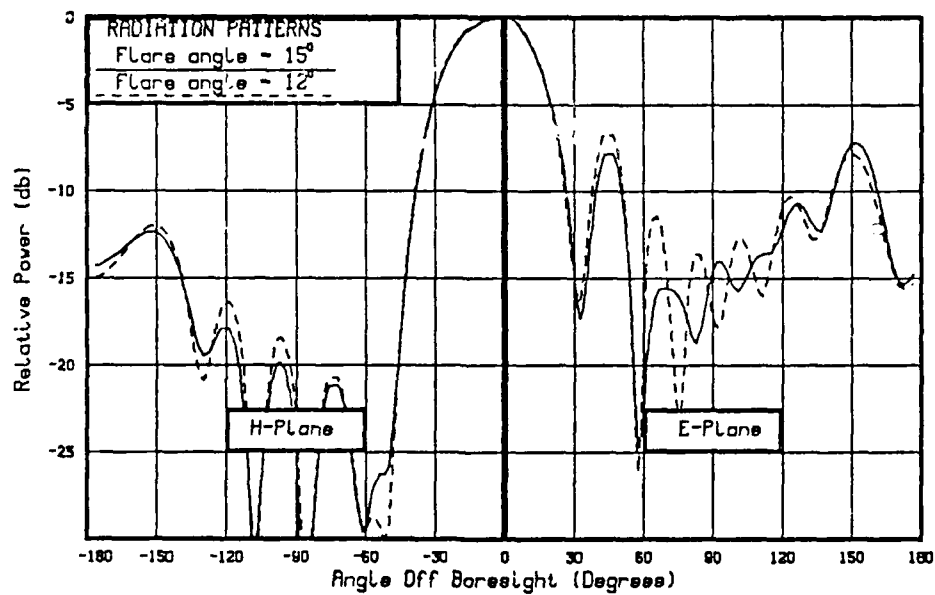


Figure A.34 Effects of Increasing Flare Angle to 15° .

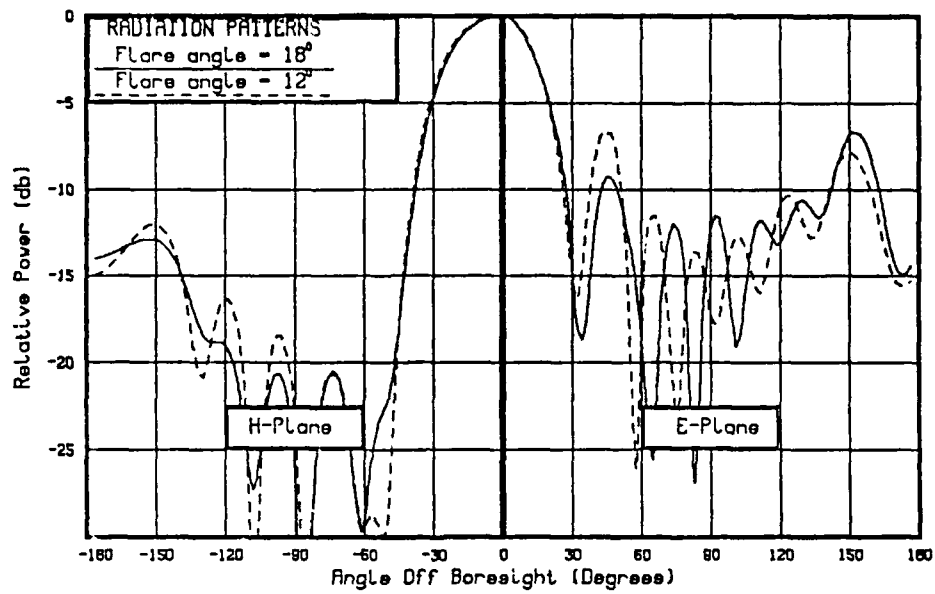


Figure A.35 Effects of Increasing Flare Angle to 18° .

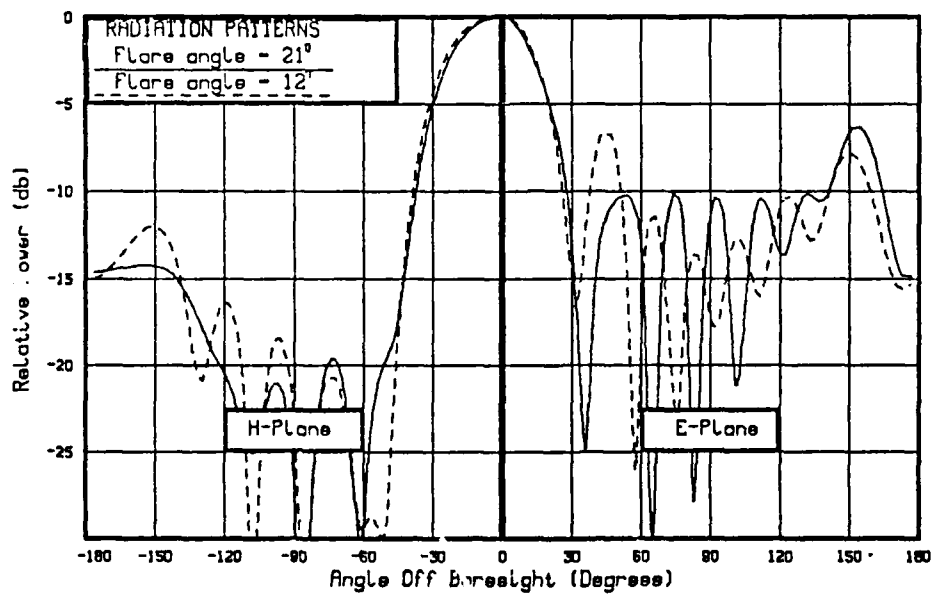


Figure A.36 Effects of Increasing Flare Angle to 21° .

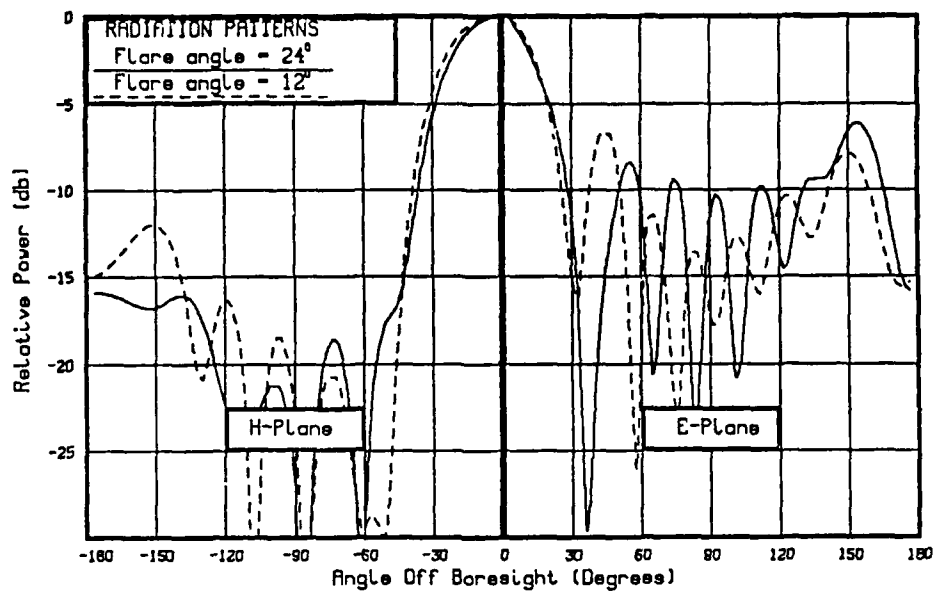


Figure A.37 Effects of Increasing Flare Angle to 24° .

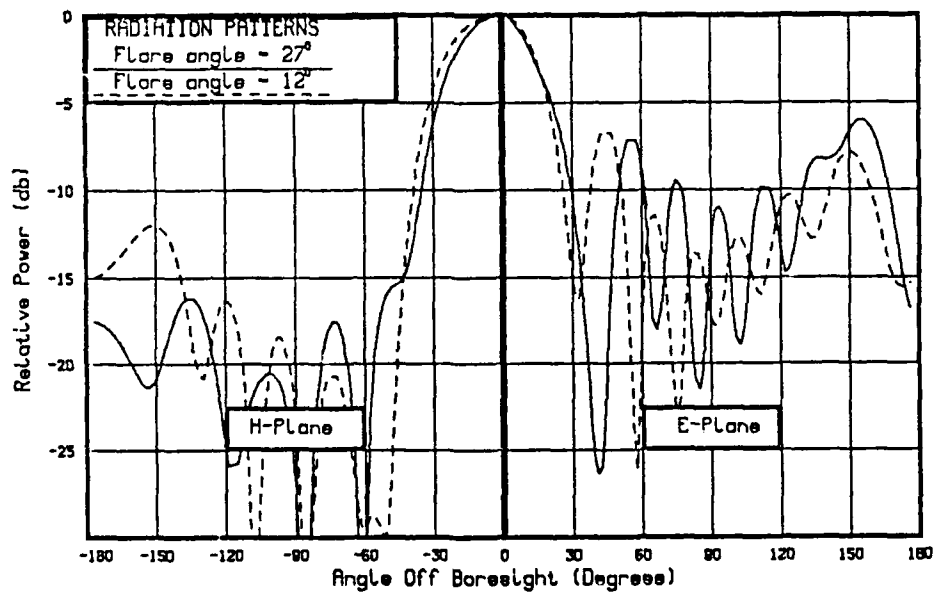


Figure A.38 Effects of Increasing Flare Angle to 27° .

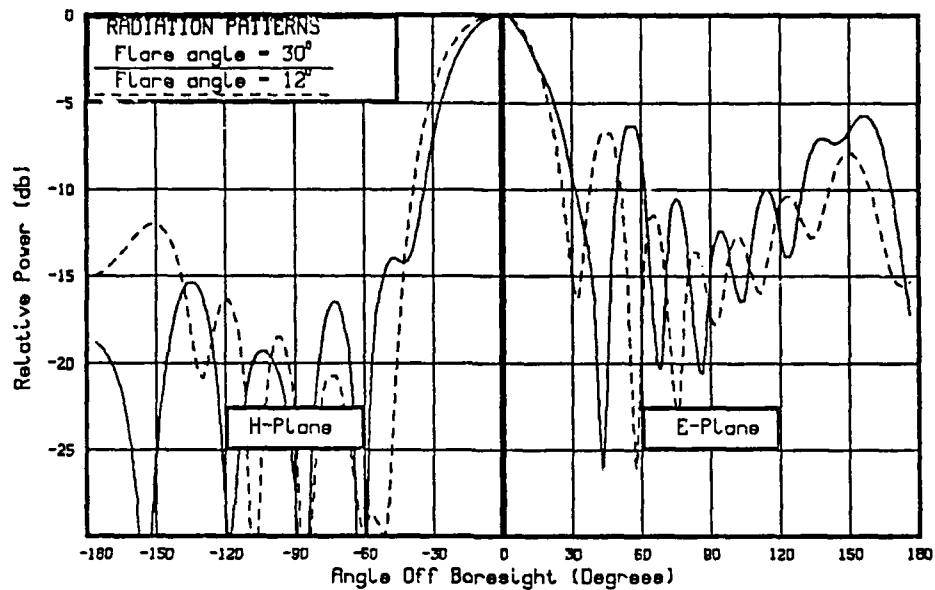


Figure A.39 Effects of Increasing Flare Angle to 30° .

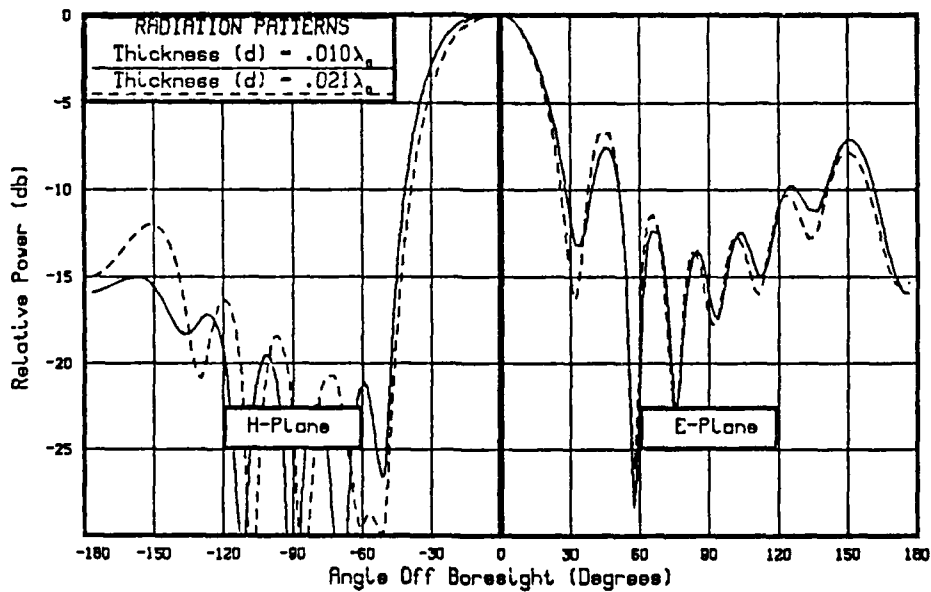


Figure A.40 Effects of Decreasing Substrate Thickness to $.010\lambda_0$.

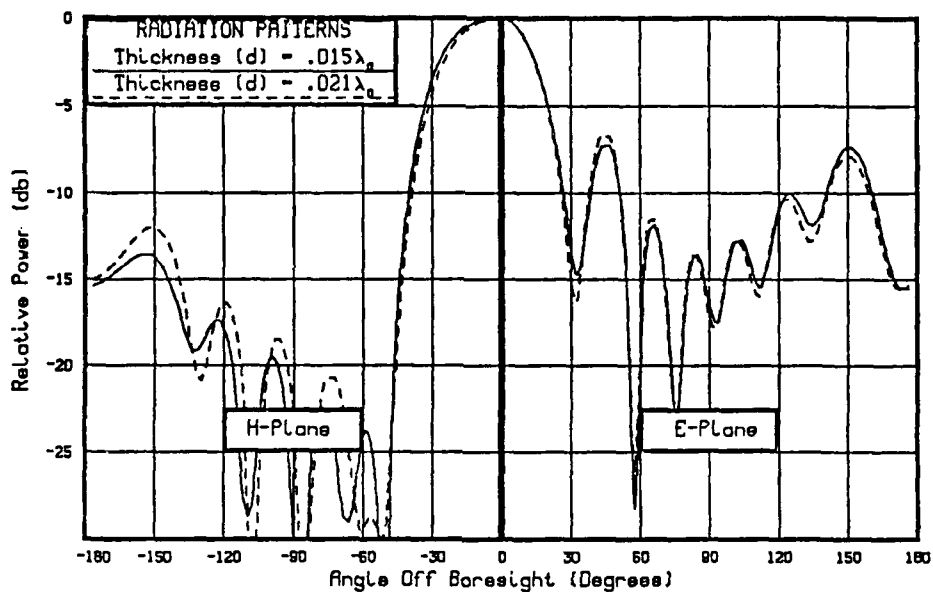


Figure A.41 Effects of Decreasing Substrate Thickness to $.015\lambda_0$.

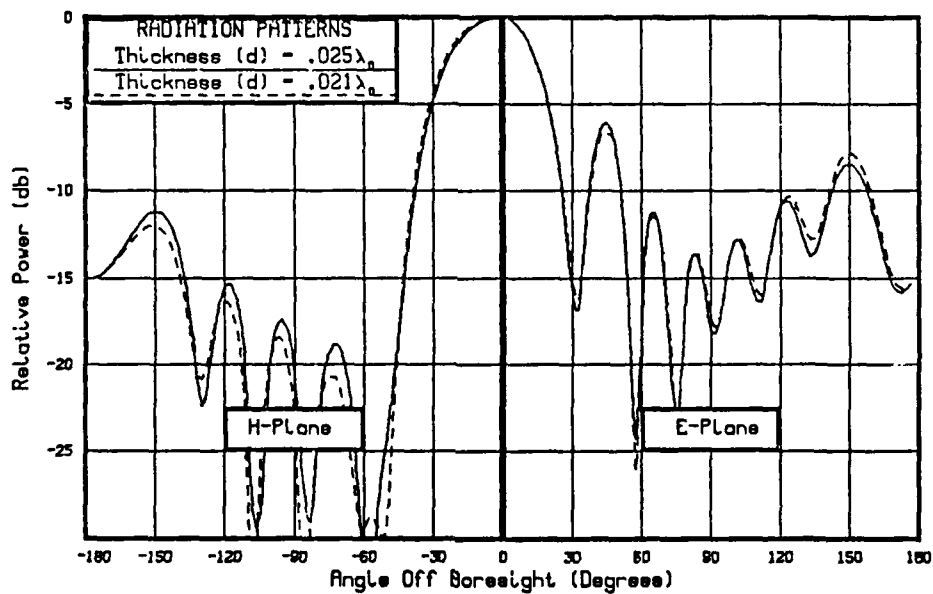


Figure A.42 Effects of Decreasing Substrate Thickness to $.025\lambda_0$.

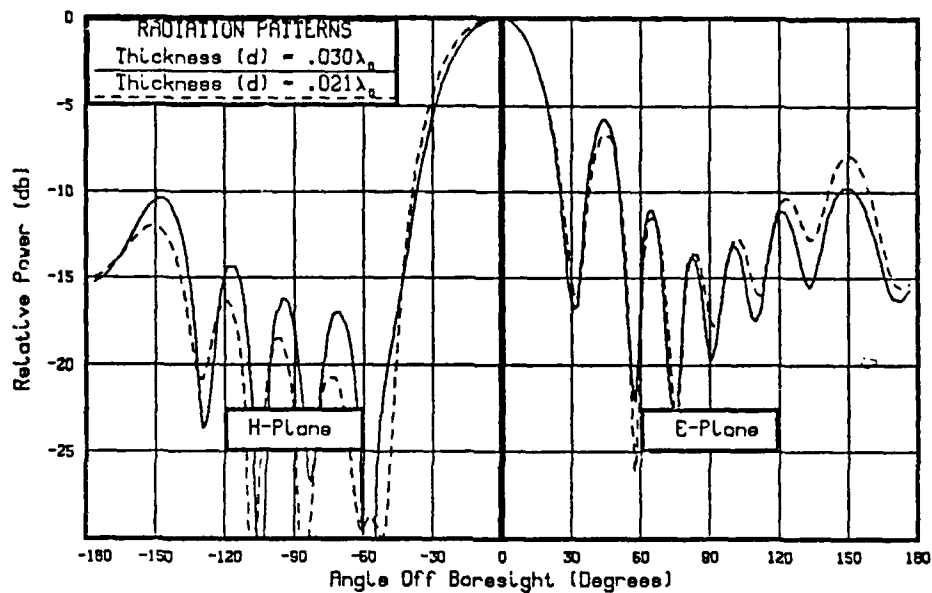


Figure A.43 Effects of Decreasing Substrate Thickness to $.030\lambda_0$.

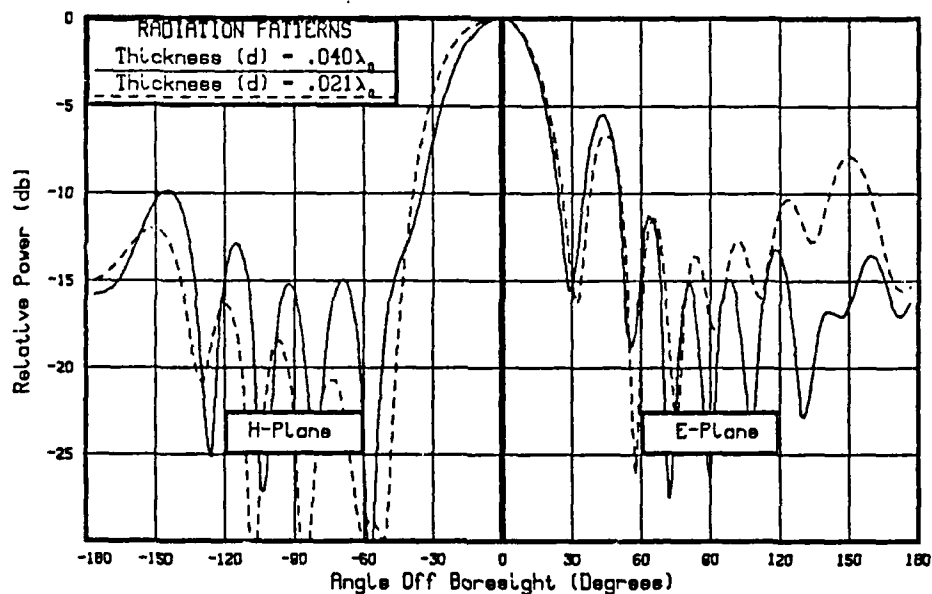


Figure A.44 Effects of Decreasing Substrate Thickness to $.040\lambda_0$.

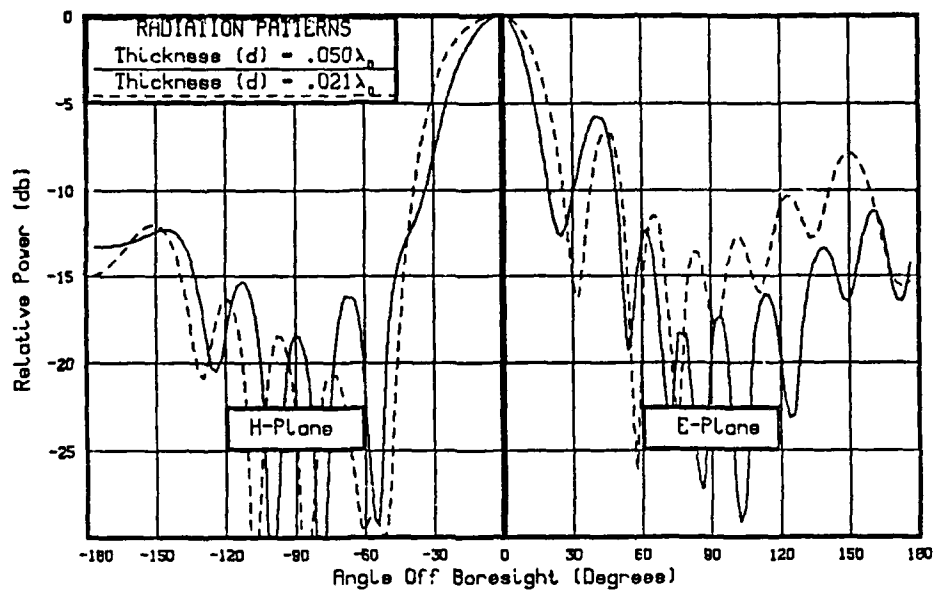


Figure A.45 Effects of Decreasing Substrate Thickness to $.050\lambda_0$.

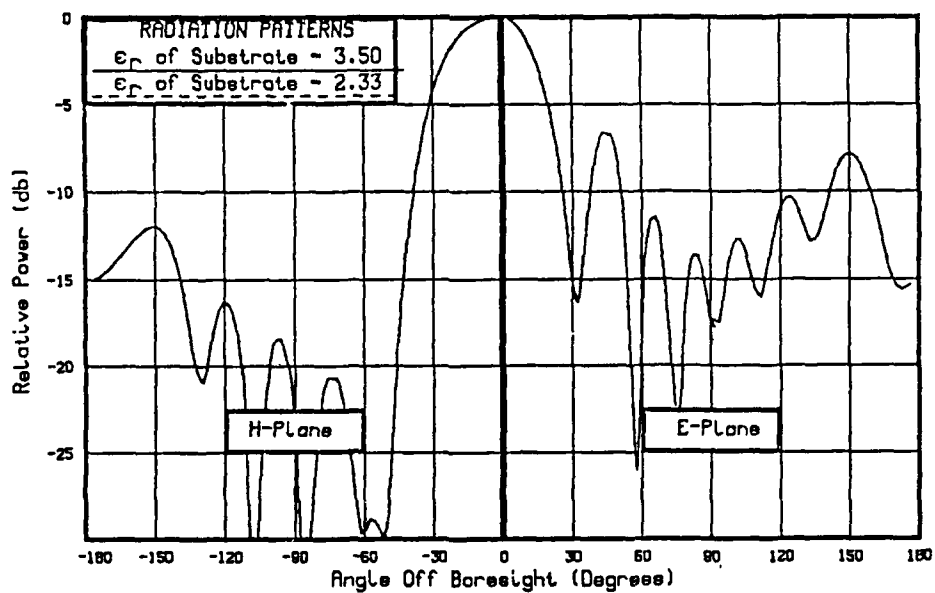


Figure A.46 Effects of Increasing Substrate Permittivity: $\epsilon_r = 3.5$.

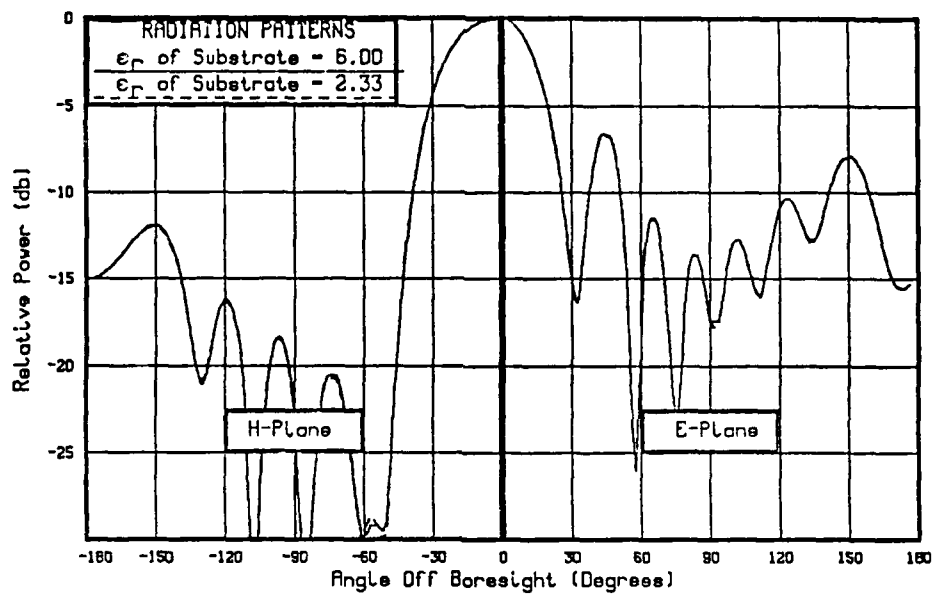


Figure A.47 Effects of Increasing Substrate Permittivity: $\epsilon_r=6.0$.

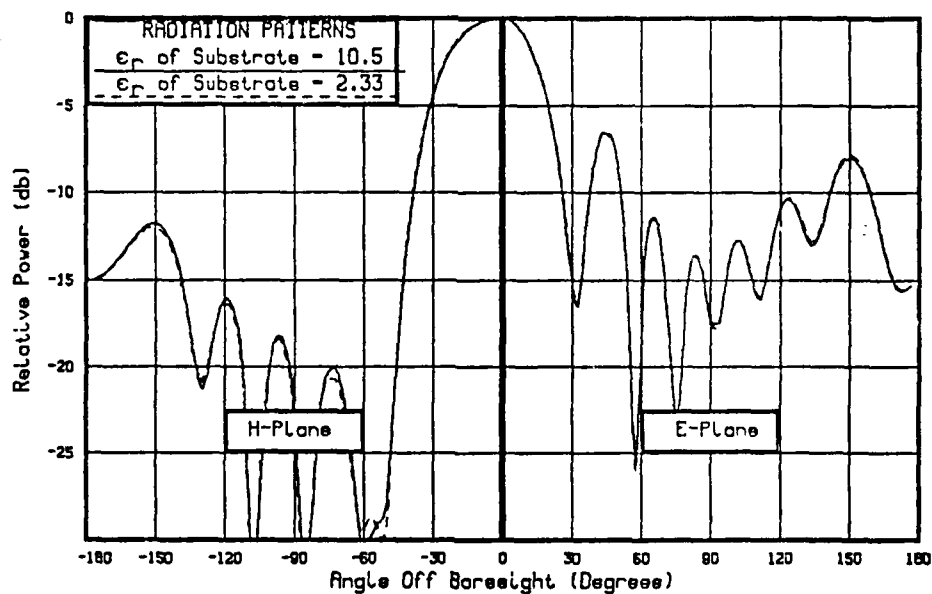


Figure A.48 Effects of Increasing Substrate Permittivity: $\epsilon_r=10.5$.

APPENDIX B LTSA RADIATION CHARACTERISTICS AS FUNCTIONS OF THE LENGTH AND HEIGHT

The summary of pattern behavior is made concise, but useful, by examining the beamwidth and sidelobe characteristics. Figures B.1-B.9 present this information (in both the E-Plane and H-Plane) versus the antenna length and height. These figures demonstrate the results of changing length for different modeled heights (Figures B.1-B.6). Similarly, Figures B.1-B.9 complement the analysis by illustrating the effects of changing height for each modeled length.

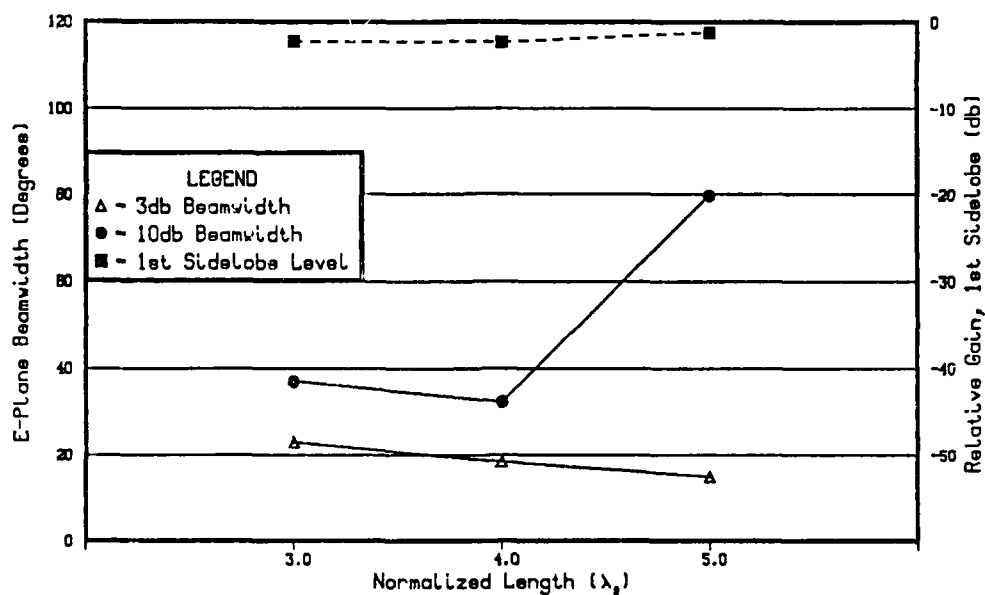


Figure B.1a E-Plane Effects of Changing L ; $H = 0.25\lambda_0$.

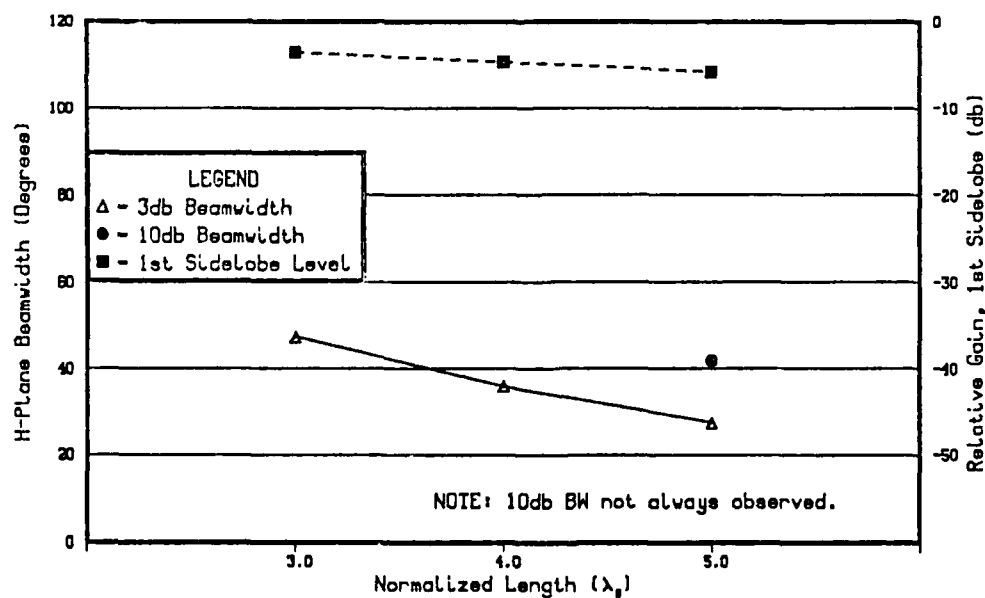


Figure B.1b H-Plane Effects of Changing L ; $H = 0.25\lambda_0$.

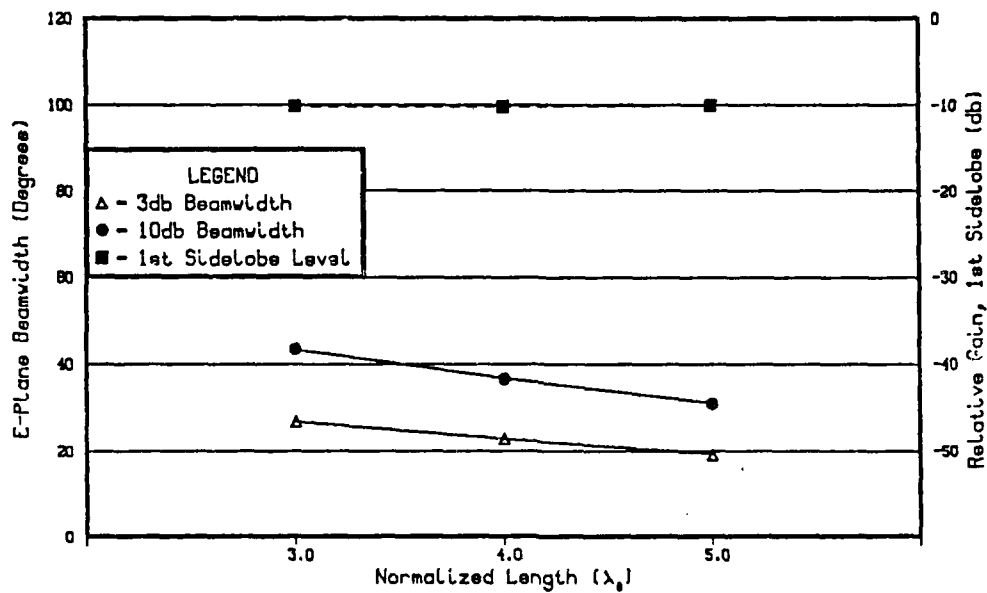


Figure B.2a E-Plane Effects of Changing L ; $H = 0.50\lambda_0$.

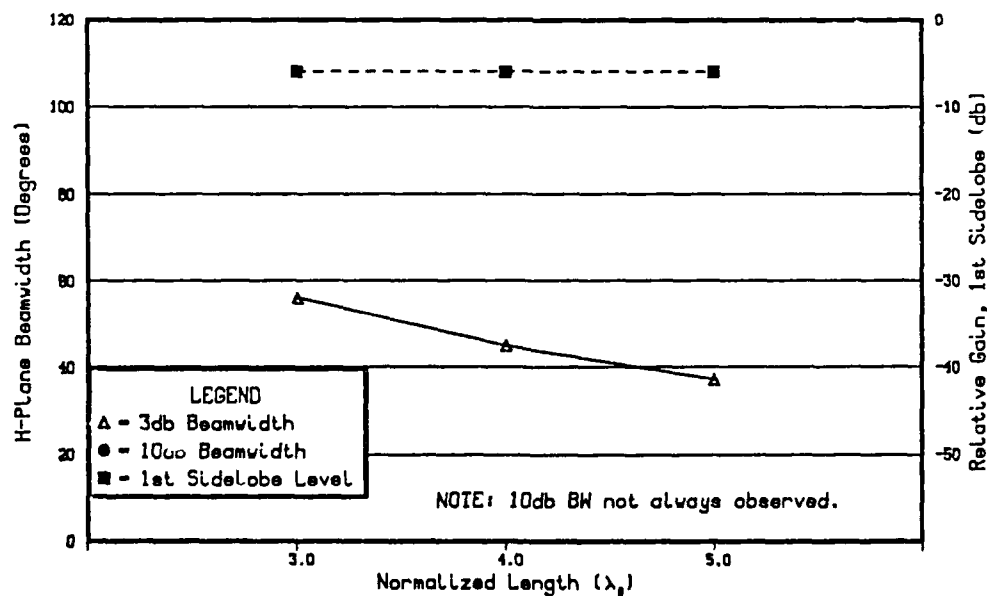


Figure B.2b H-Plane Effects of Changing L ; $H = 0.50\lambda_0$.

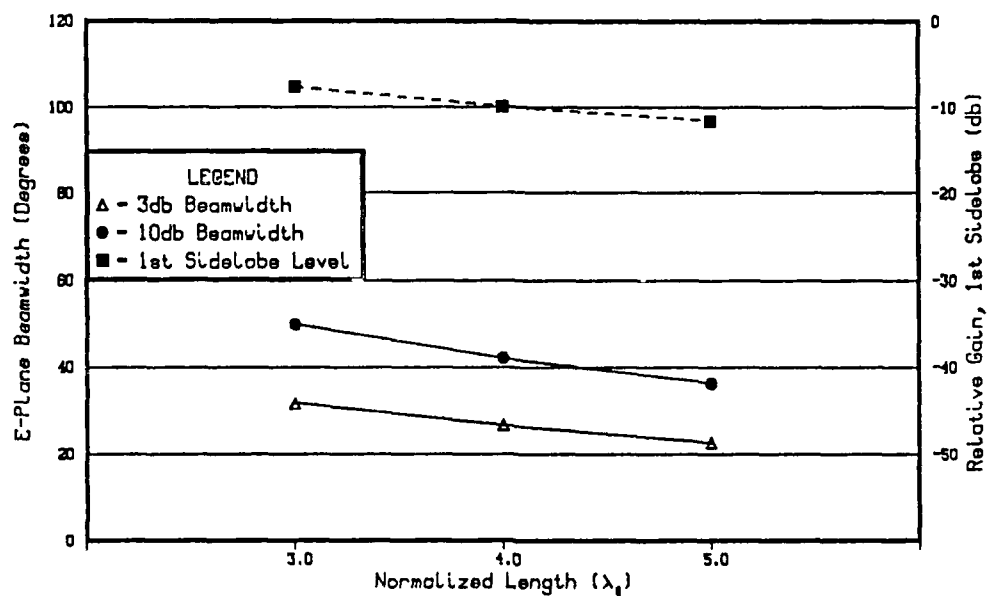


Figure B.3a E-Plane Effects of Changing L ; $H = 0.75\lambda_0$.

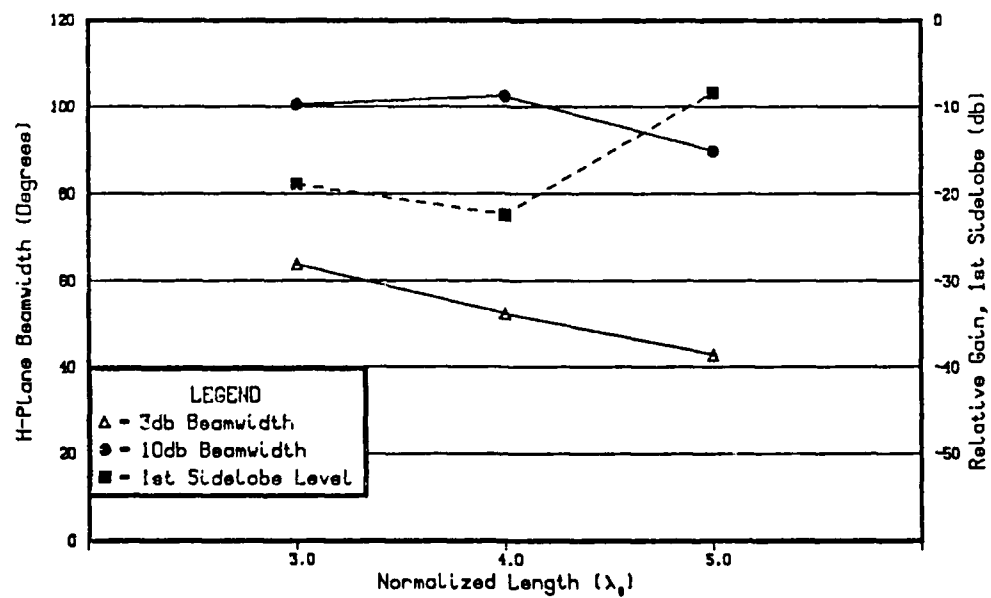


Figure B.3b H-Plane Effects of Changing L ; $H = 0.75\lambda_0$.

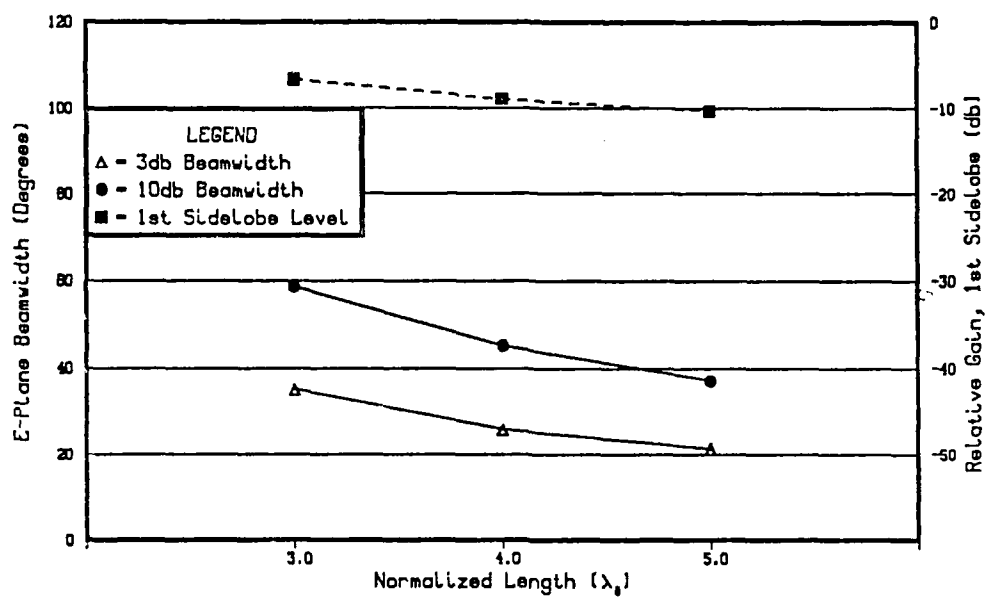


Figure B.4a E-Plane Effects of Changing L ; $H = 1.00\lambda_0$.

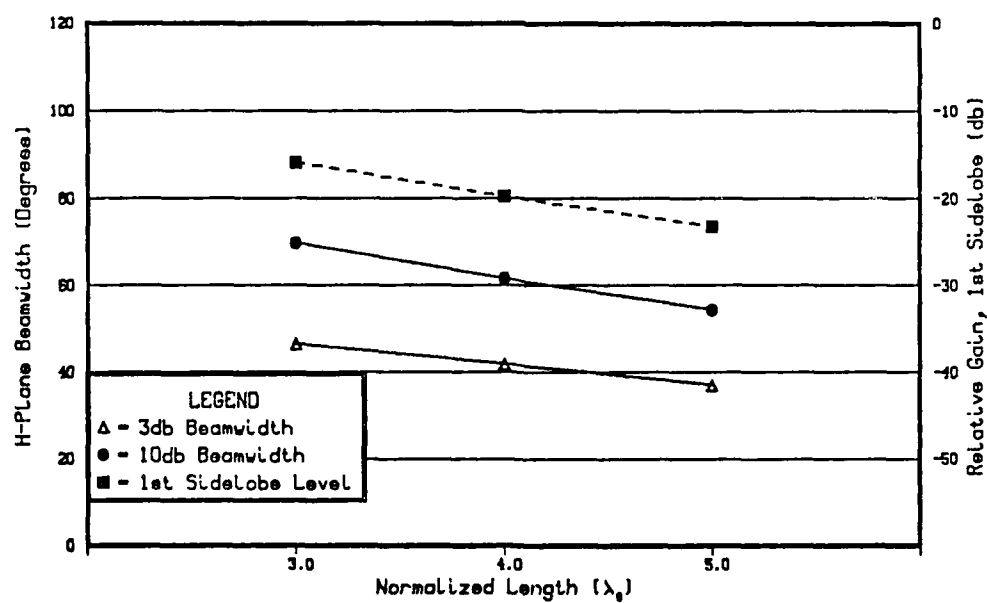


Figure B.4b H-Plane Effects of Changing L ; $H = 1.00\lambda_0$.

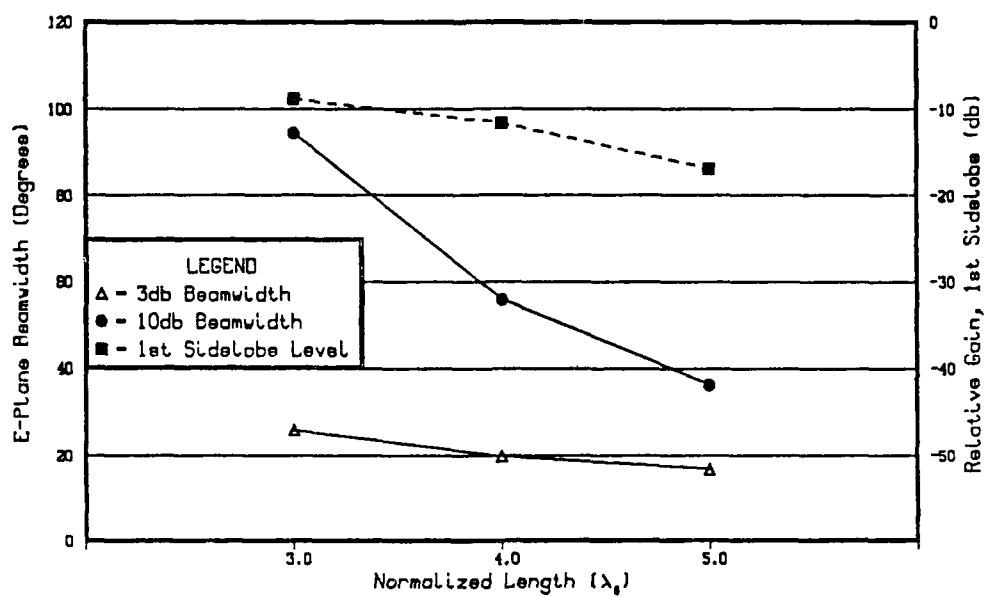


Figure B.5a E-Plane Effects of Changing L ; $H = 1.25\lambda_0$.

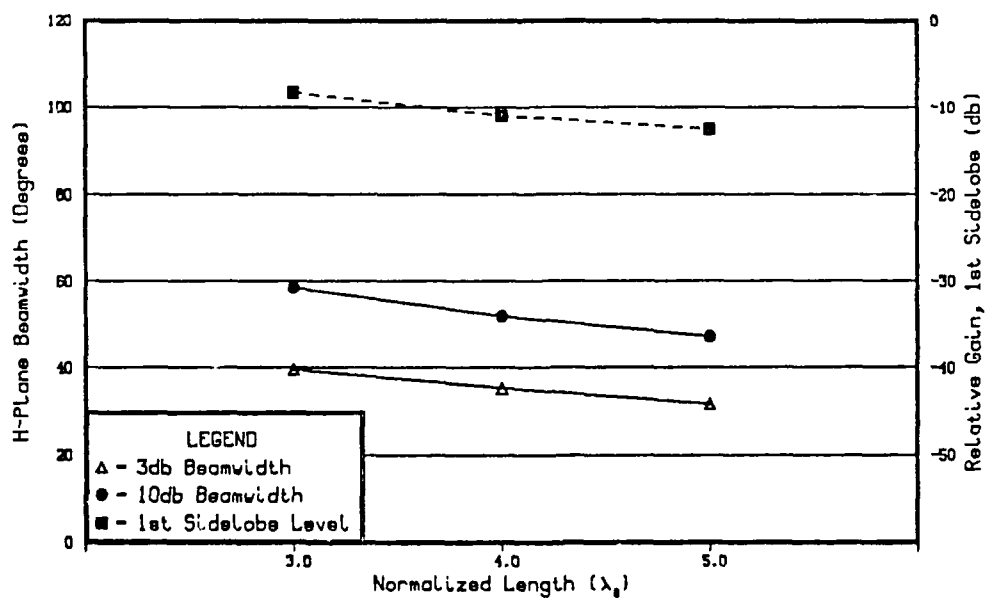


Figure B.5b H-Plane Effects of Changing L ; $H = 1.25\lambda_0$.

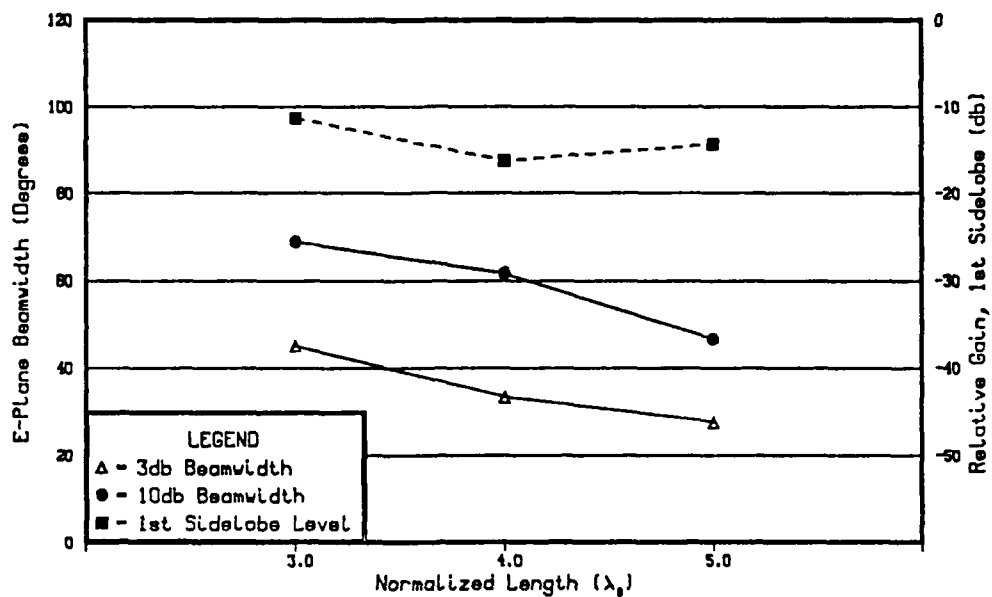


Figure B.6a E-Plane Effects of Changing L ; $H = 1.50\lambda_0$.

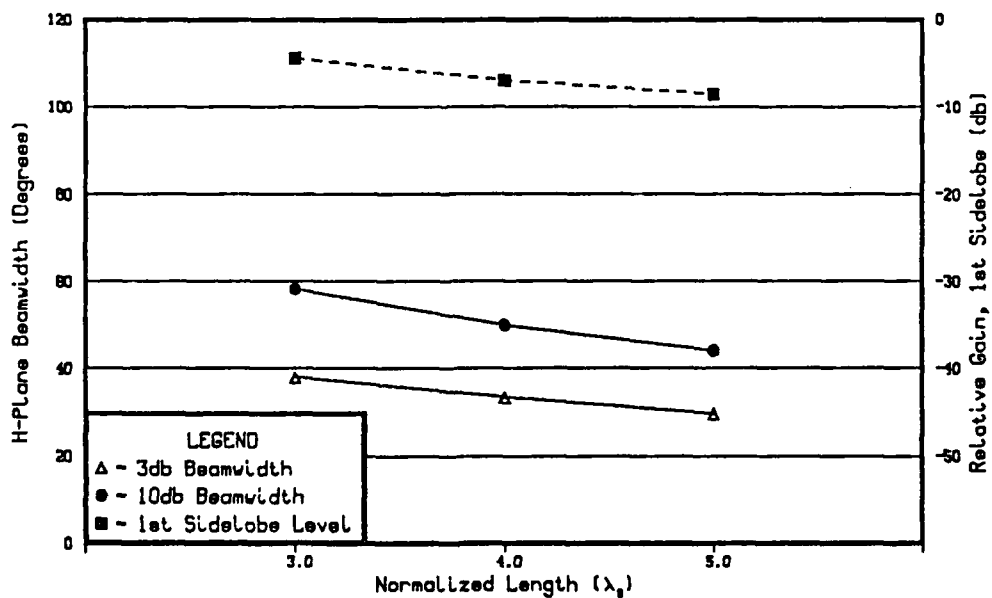


Figure B.6b H-Plane Effects of Changing L ; $H = 1.50\lambda_0$.

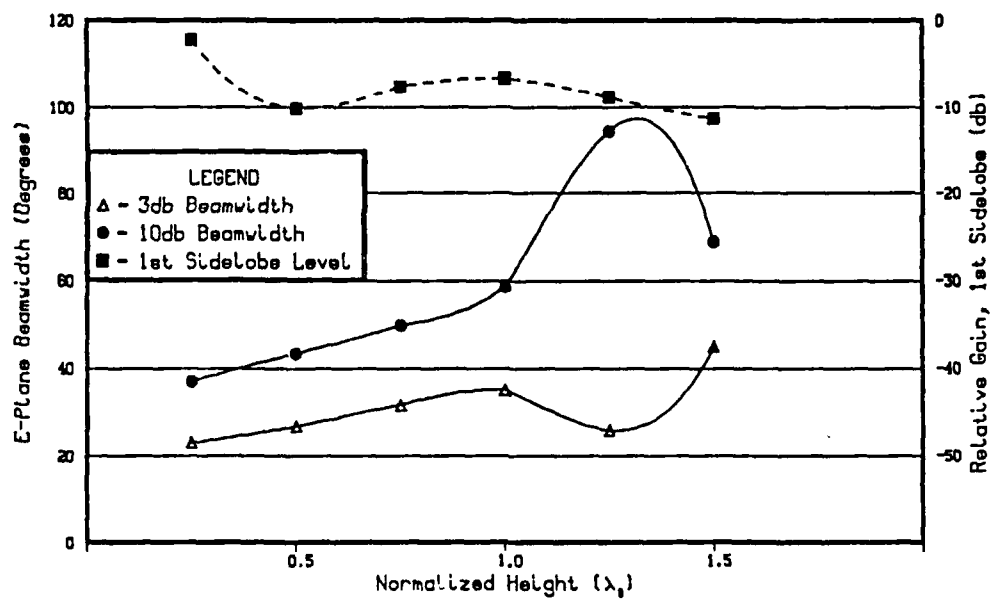


Figure B.7a E-Plane Effects of Changing H ; $L = 3\lambda_0$.

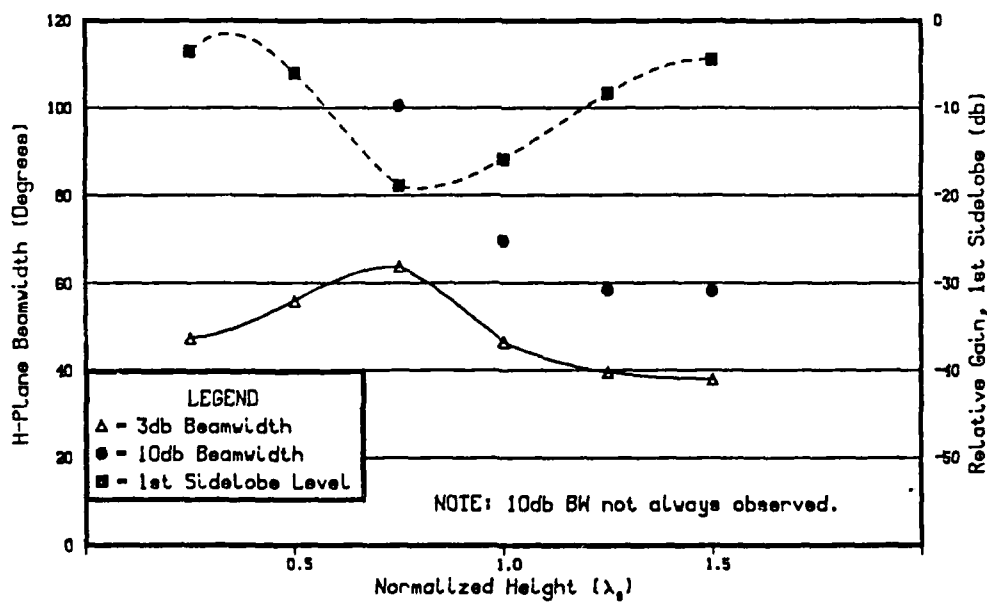


Figure B.7b H-Plane Effects of Changing H ; $L = 3\lambda_0$.

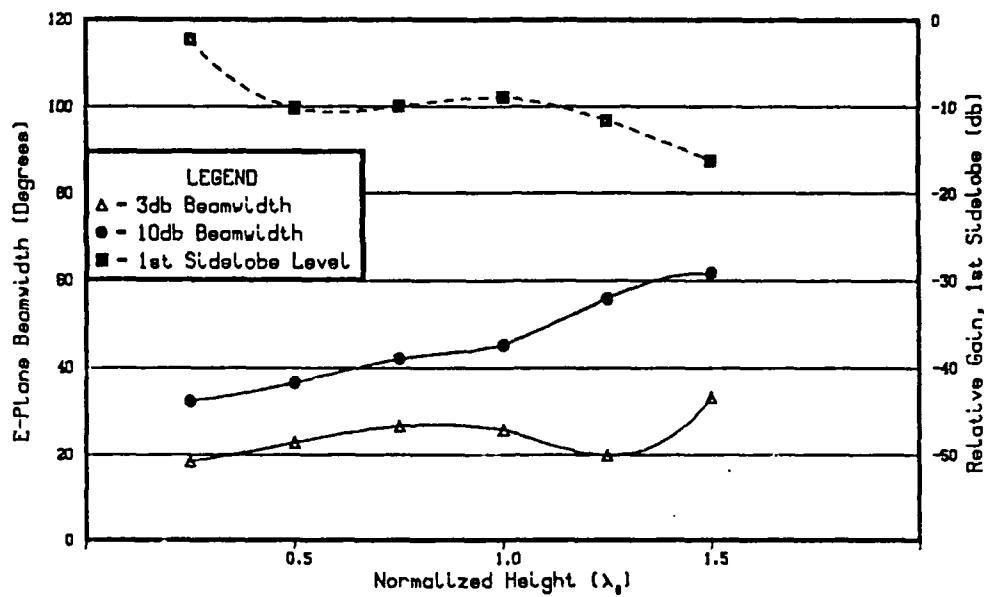


Figure B.8a E-Plane Effects of Changing H ; $L = 4\lambda_0$.

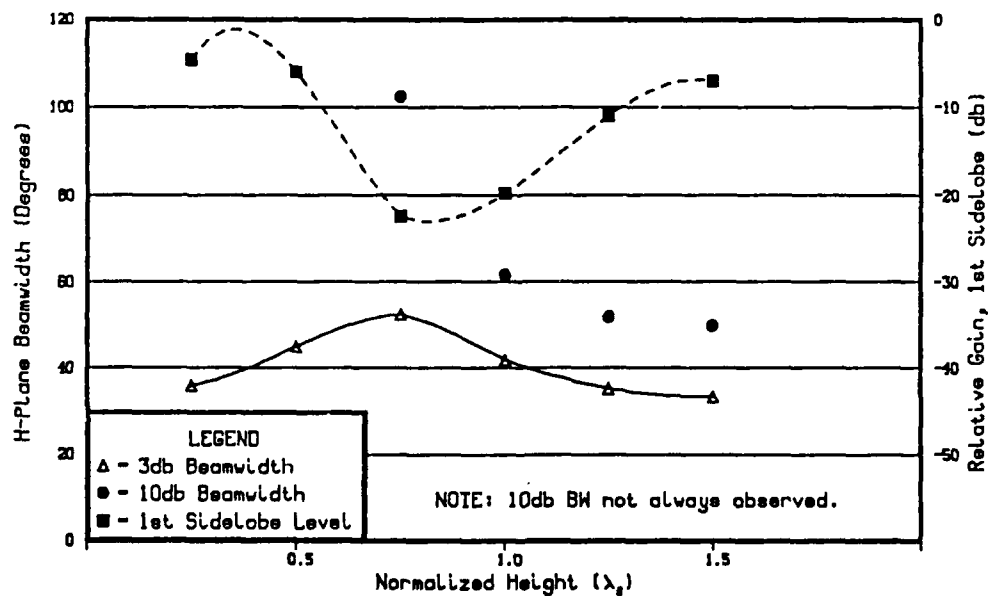


Figure B.8b H-Plane Effects of Changing H ; $L = 4\lambda_0$.

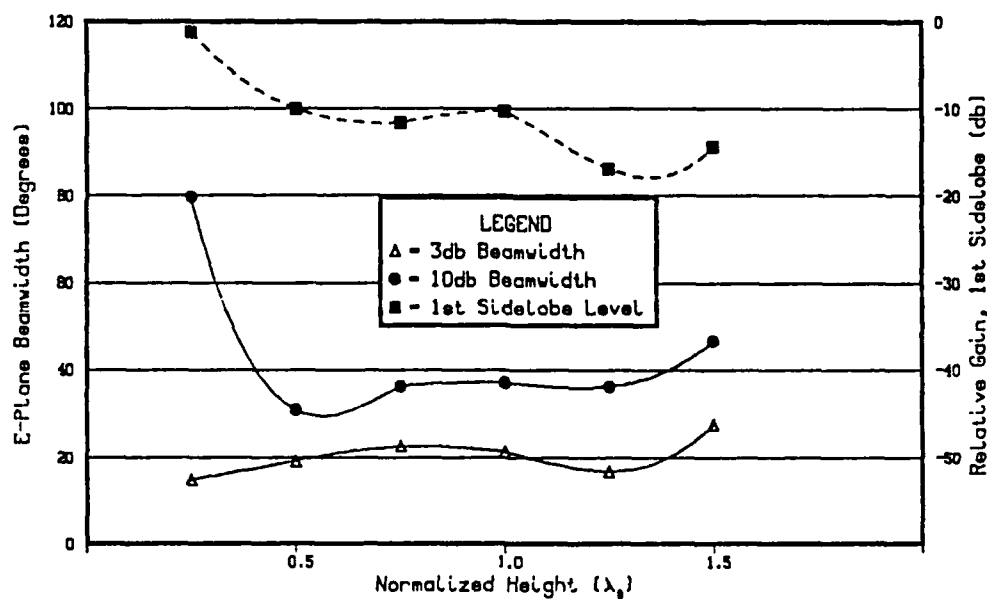


Figure B.9a E-Plane Effects of Changing H ; $L = 5\lambda_0$.

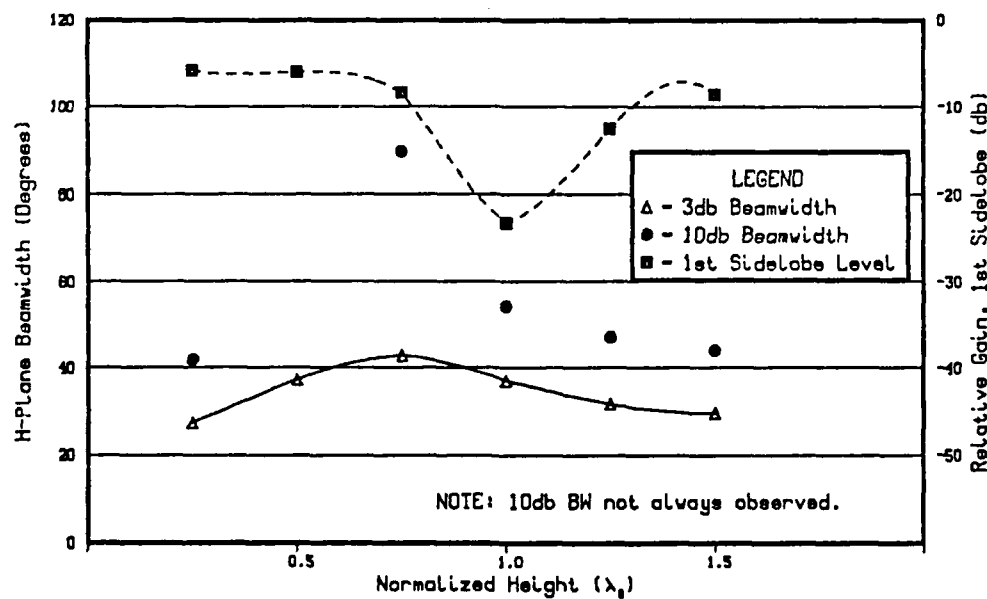


Figure B.9b H-Plane Effects of Changing H ; $L = 5\lambda_0$.

APPENDIX C LTSA CURRENT DISTRIBUTION

A key facet of this unique planar antenna is the slow wave structure which is achieved by the use of the dielectric substrate. However, the travelling wave nature of the plate currents is responsible for obtaining an end-fire main beam. This effect is illustrated in the modeled current distribution for each design used in this thesis.

The current distribution plots in Figures C.1-C.39 provide a means to correlate observed pattern changes to the respective changes in current on the antenna. These computations are based on fair approximations sufficient to accurately predict the far-field pattern.

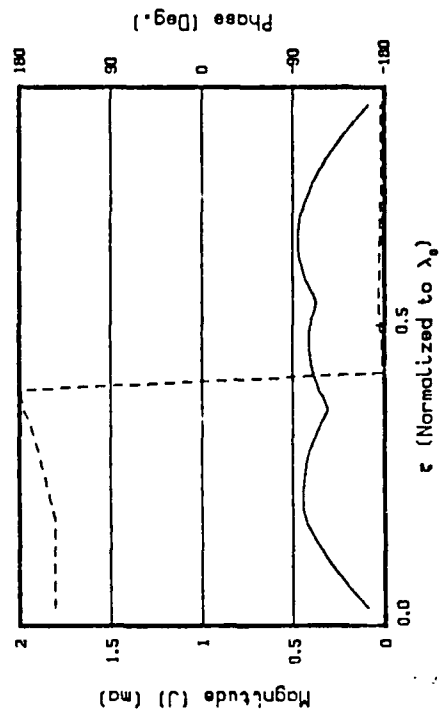
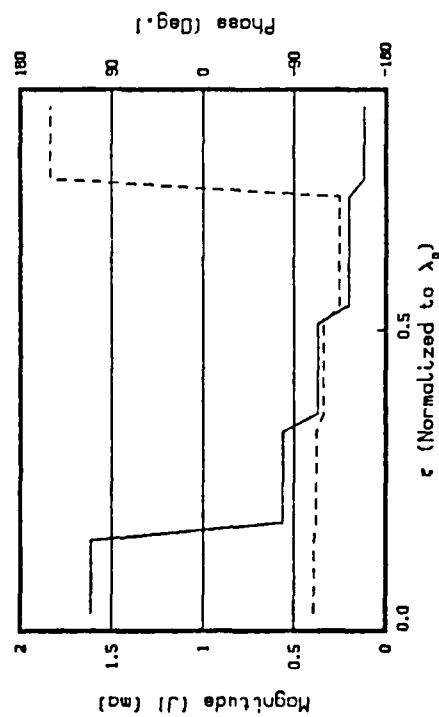
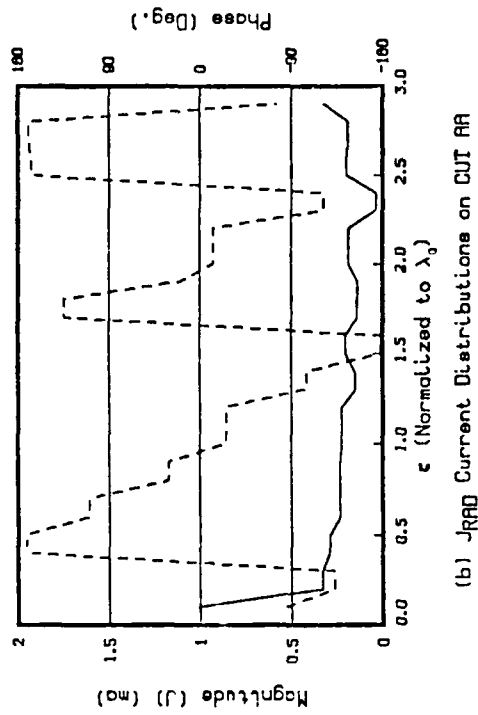
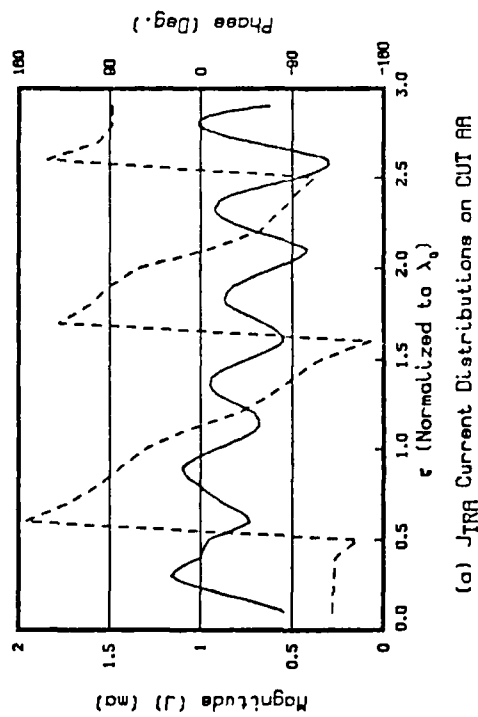
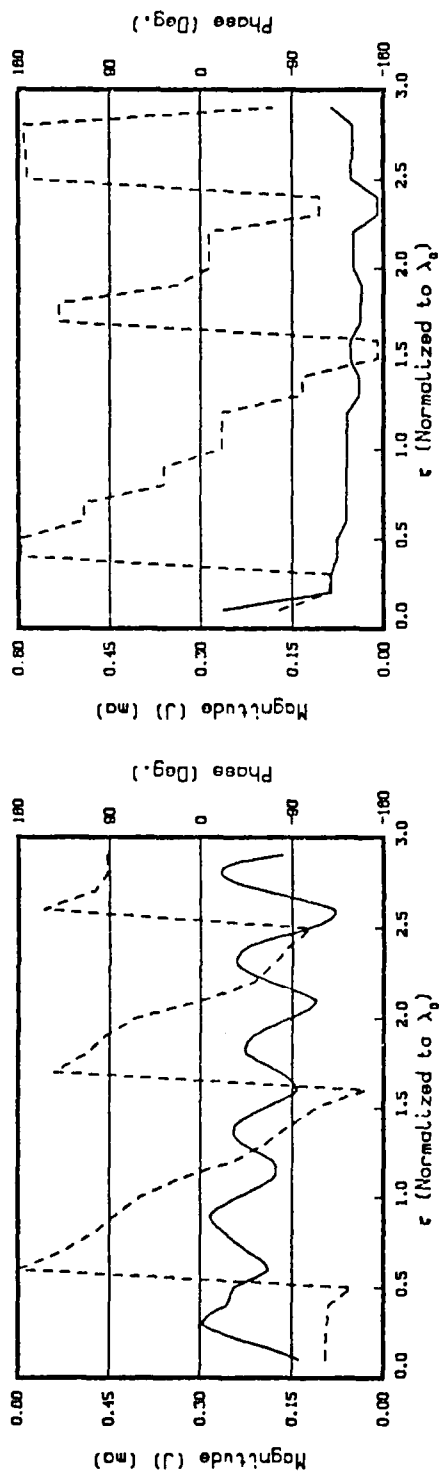
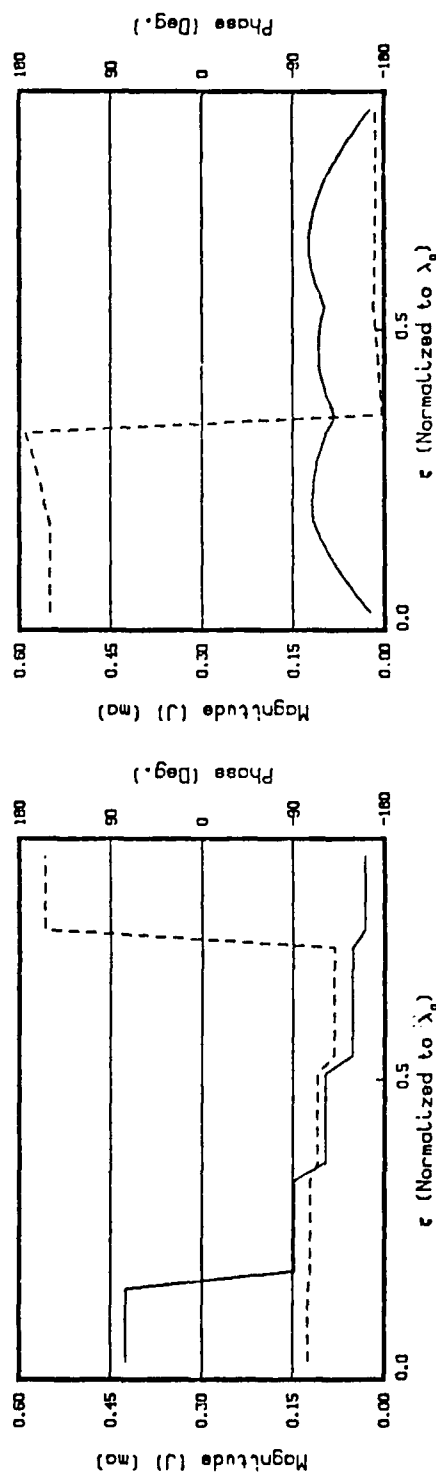


Figure C.1 LTSA Plate Currents Modeled for a Known Empirical Design.

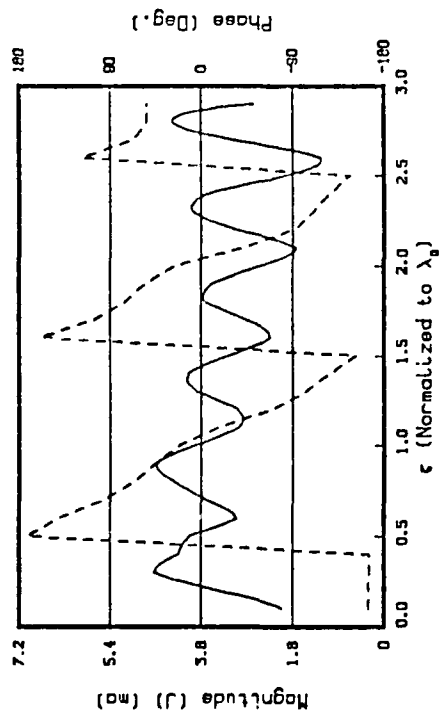


(b) JRAD Current Distributions on CUT AA

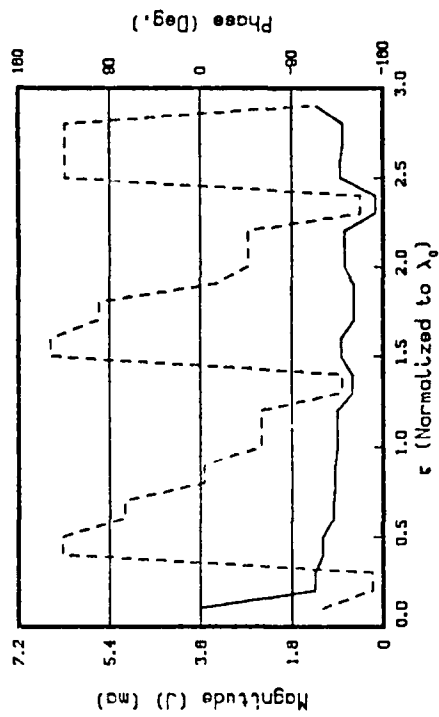


(d) JRAD Current Distributions on CUT BB

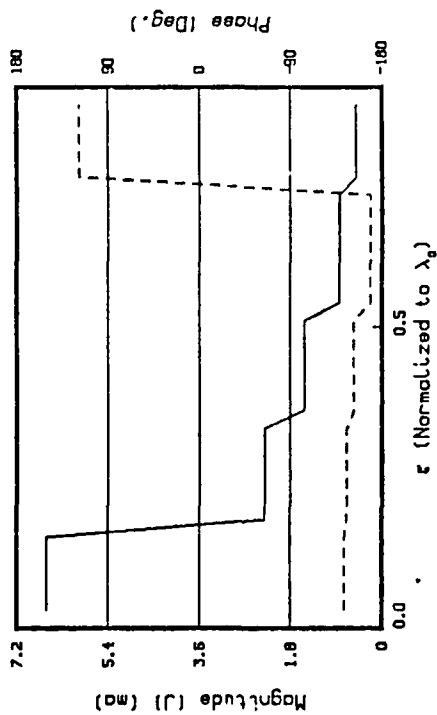
Figure C.2 Modeled Currents When Feed Dipole Length = $.05\lambda_0$.



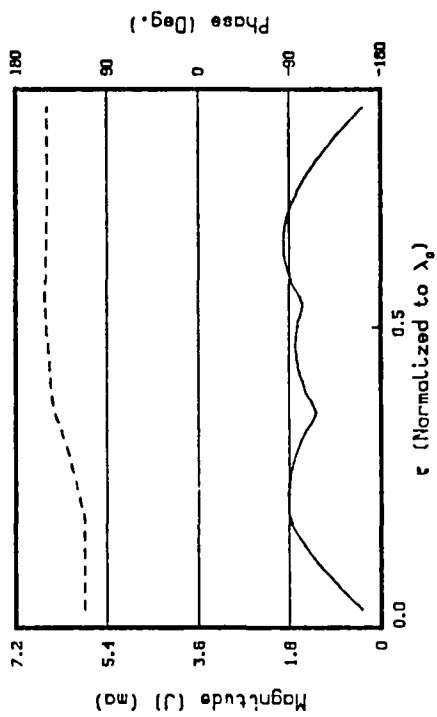
(a) J_{TRR} Current Distributions on CUT AA



(b) J_{TRR} Current Distributions on CUT AA

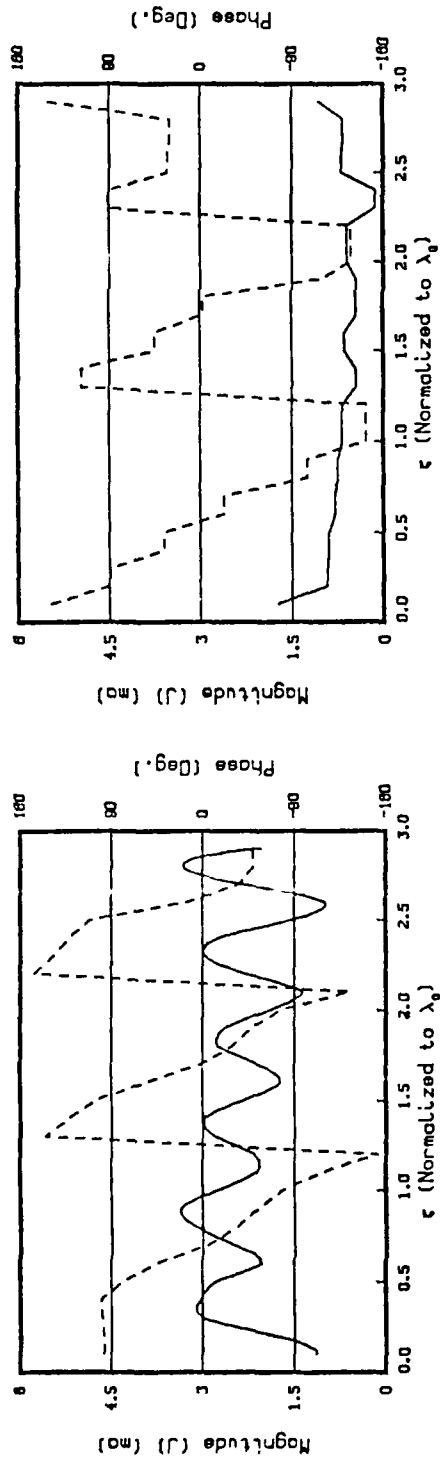


(c) J_{TRR} Current Distributions on CUT BB

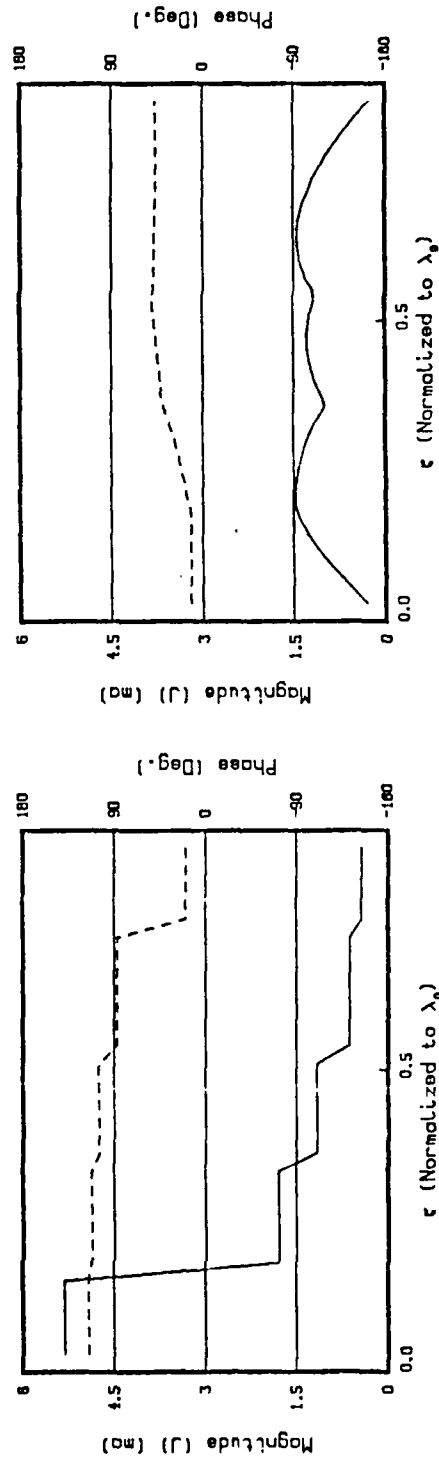


(d) J_{TRR} Current Distributions on CUT BB

Figure C.3 Modeled Currents When Feed Dipole Length = $.20\lambda_0$.

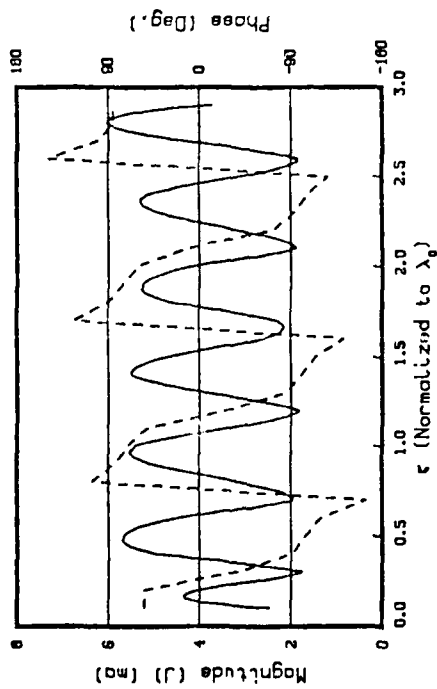


(b) J-RAD Current Distributions on CUT RR

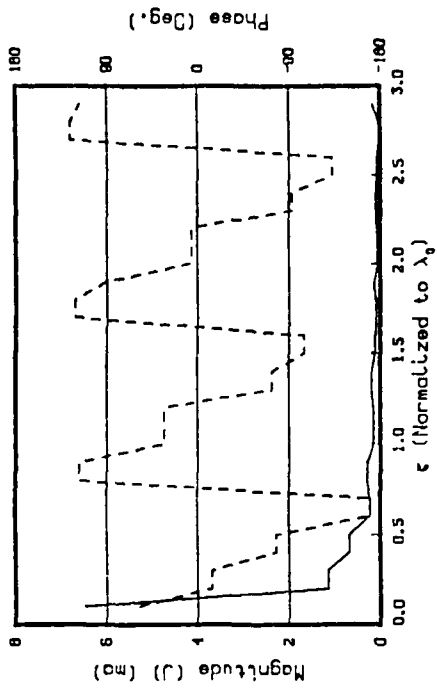


(d) J-RAD Current Distributions on CUT BB

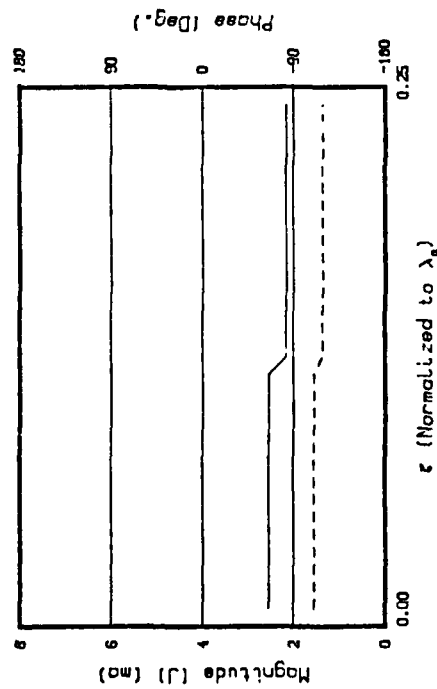
Figure C.4 Modeled Currents When Feed Dipole Length = $.30\lambda_0$.



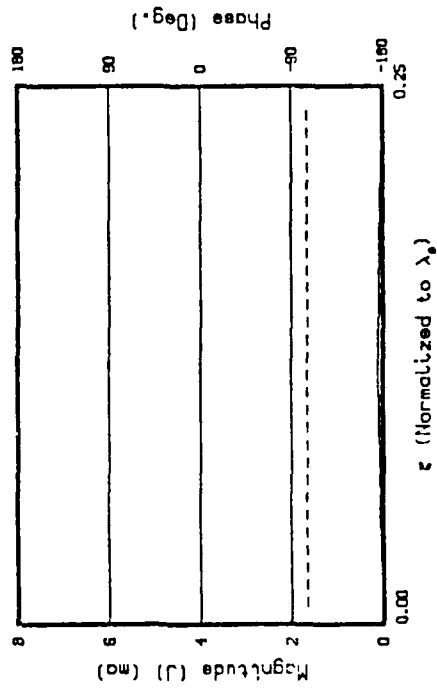
(a) J_{TRA} Current Distributions on CUT AA



(b) J_{RFO} Current Distributions on CUT AA

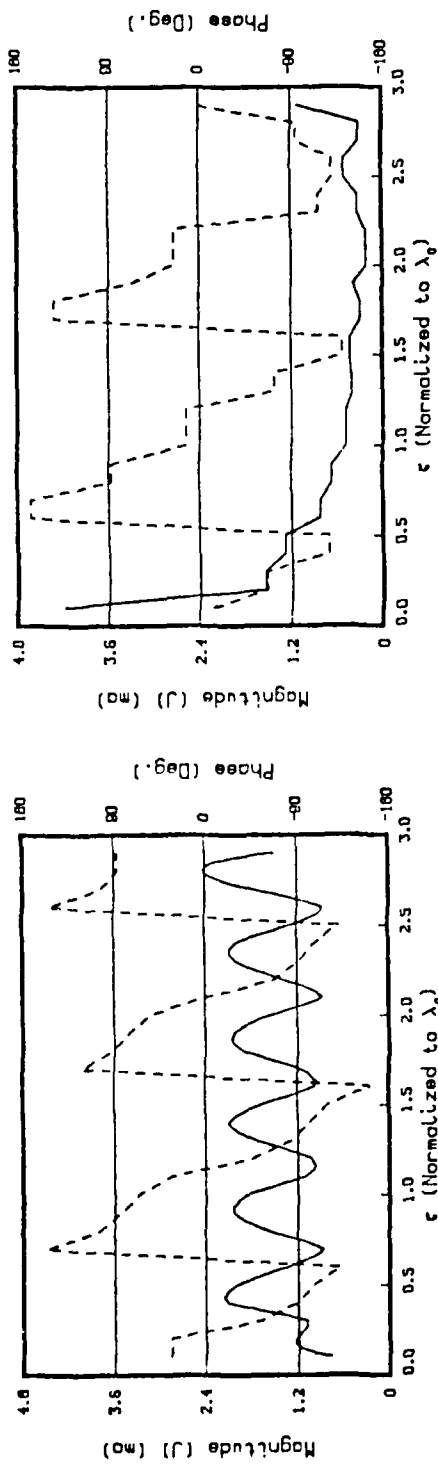


(c) J_{TRA} Current Distributions on CUT BB

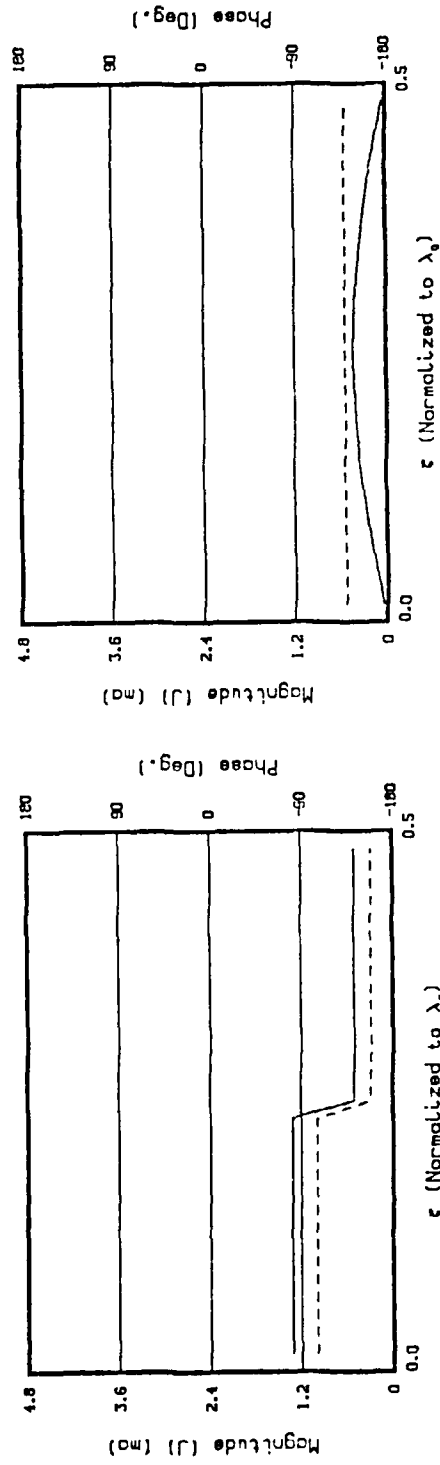


(d) J_{RFO} Current Distributions on CUT BB

Figure C.5 Modeled Currents When Height $\sim .25\lambda_0$ and Length $\sim 3\lambda_0$.



(a) JTRR Current Distributions on CUT RA

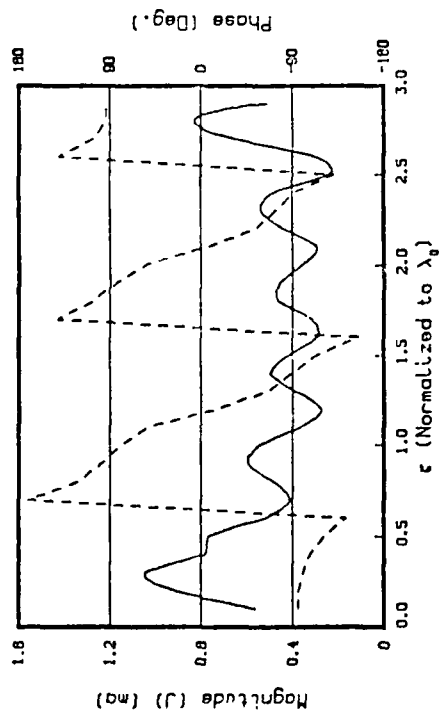


(b) JTRR Current Distributions on CUT RA

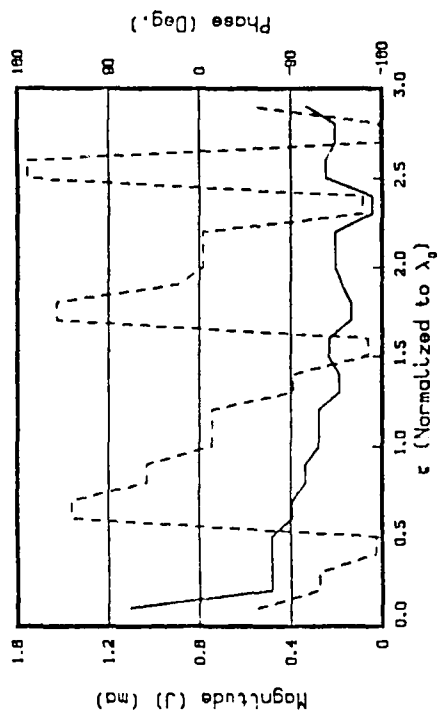
(c) JTRR Current Distributions on CUT BB

(d) JTRR Current Distributions on CUT BB

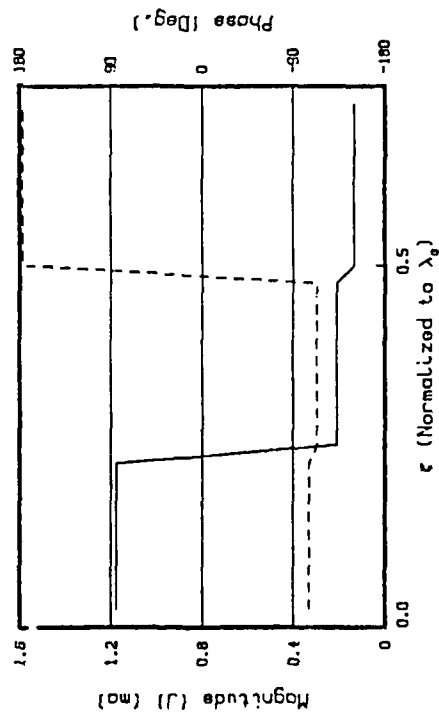
Figure C.6 Modeled Currents When Height = $.50\lambda_0$ and Length = $3\lambda_0$.



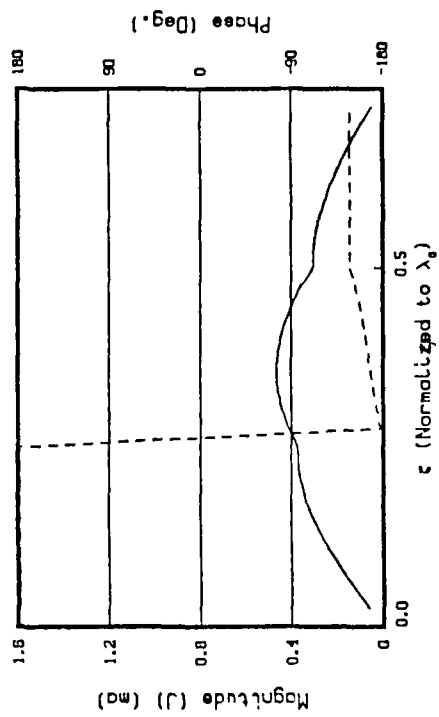
(a) J-TRR Current Distributions on CUT AA



(b) J-RRR Current Distributions on CUT AA



(c) J-TRR Current Distributions on CUT BB



(d) J-RRR Current Distributions on CUT BB

Figure C.7 Modeled Currents When Height = $.75\lambda_0$ and Length = $3\lambda_0$.

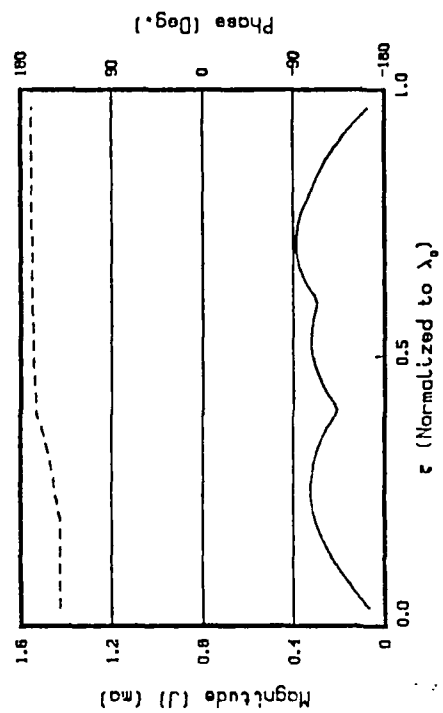
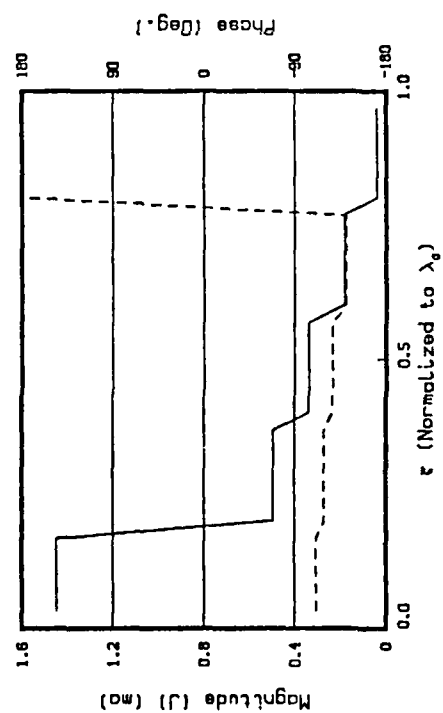
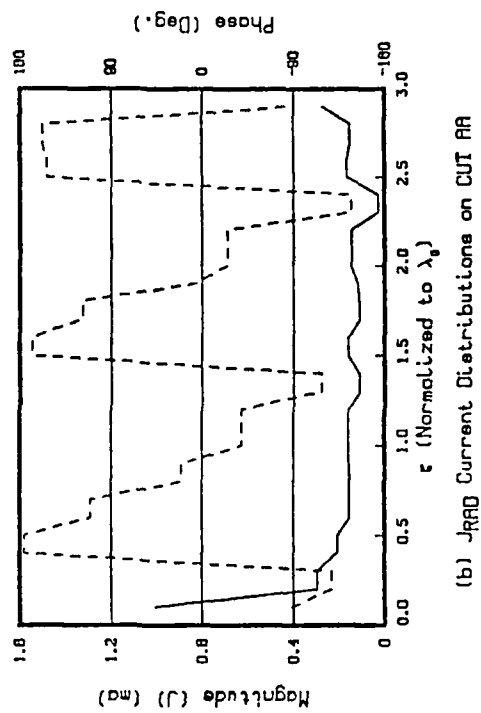
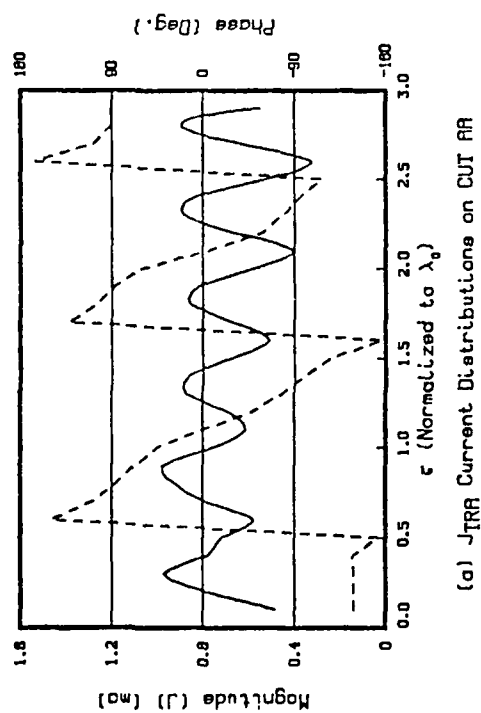
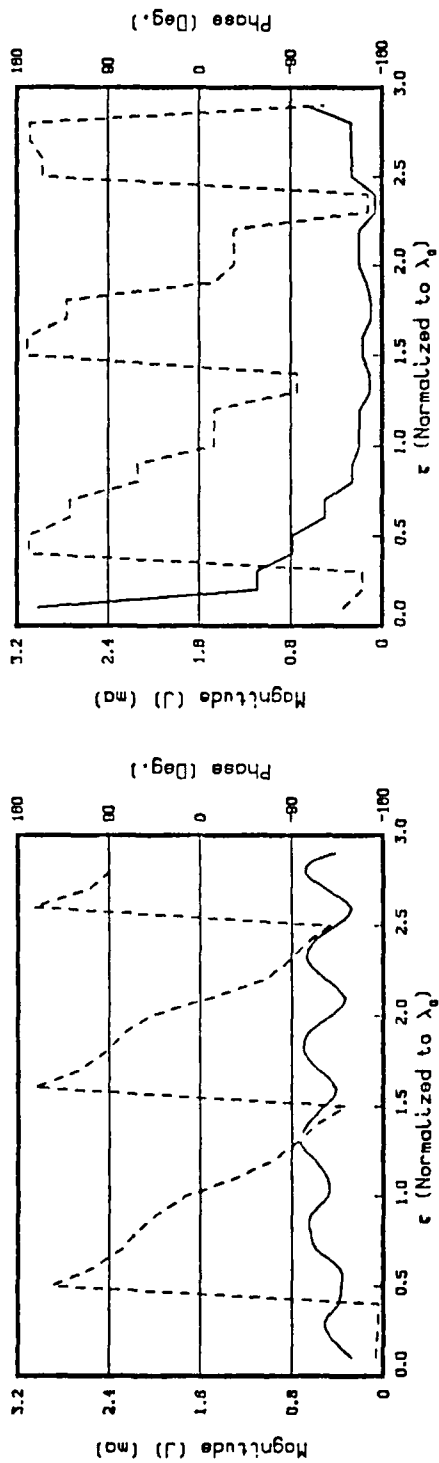
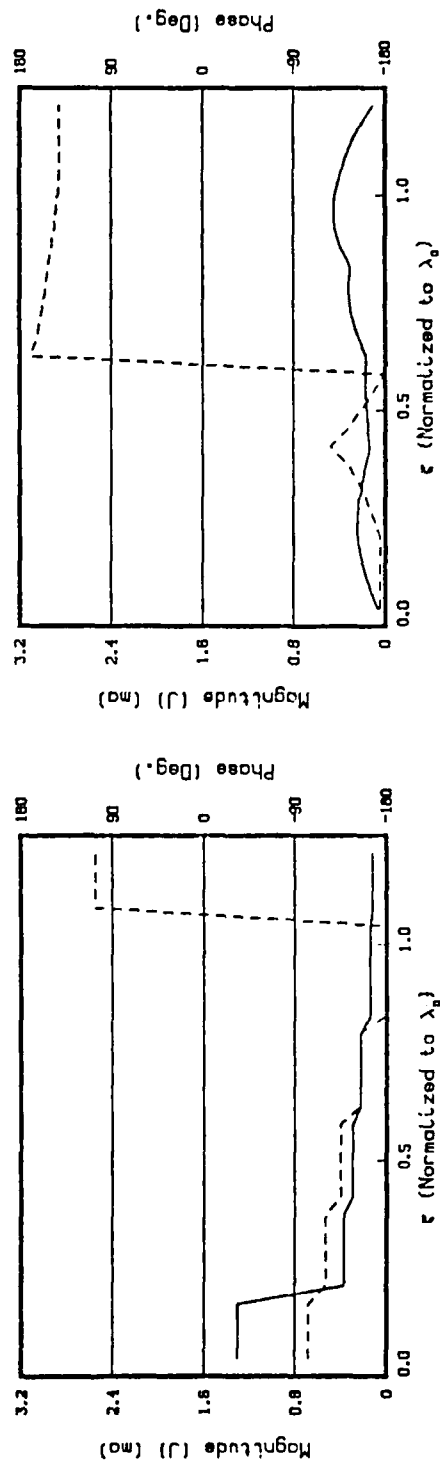


Figure C.8 Modeled Currents When Height = $1.00\lambda_0$ and Length = $3\lambda_0$.

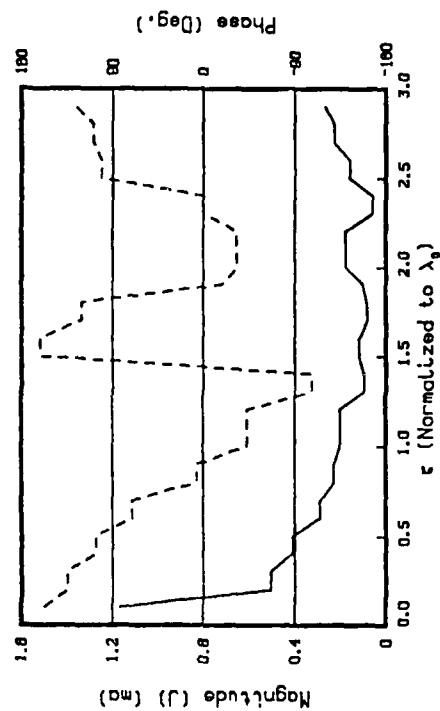


(b) JRAQ Current Distributions on CUT AA

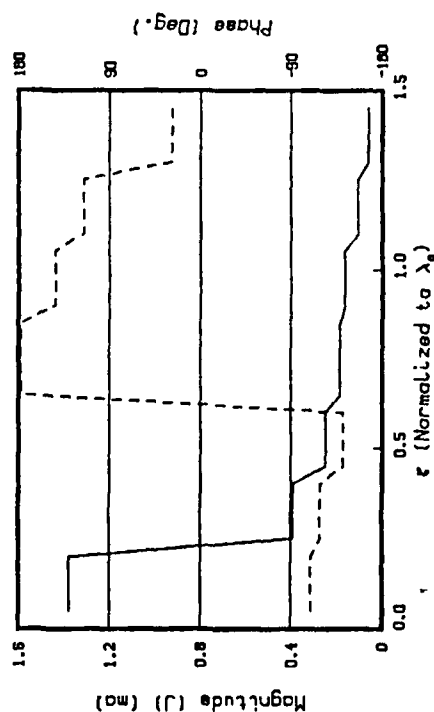


(d) JRAQ Current Distributions on CUT BB

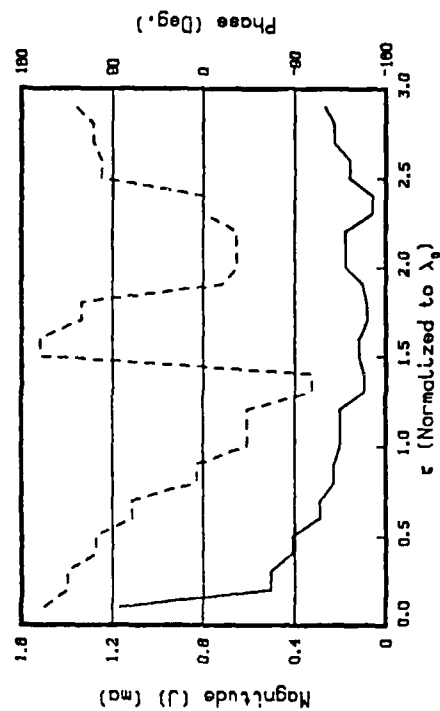
Figure C.9 Modeled Currents When Height = $1.25\lambda_0$ and Length = $3\lambda_0$.



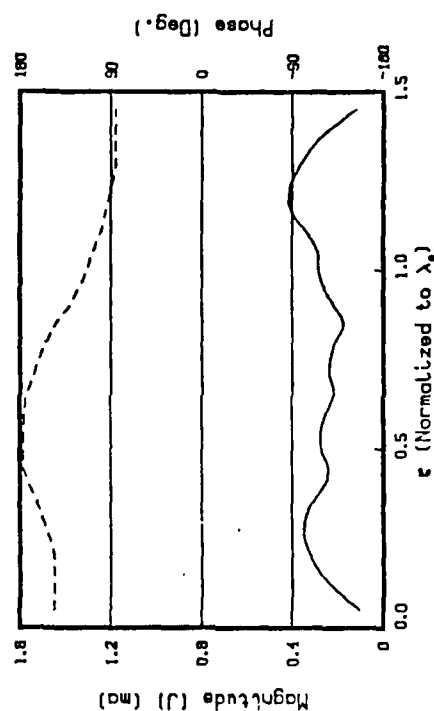
(a) JTRA Current Distributions on CUT RA



(c) JTRA Current Distributions on CUT BB

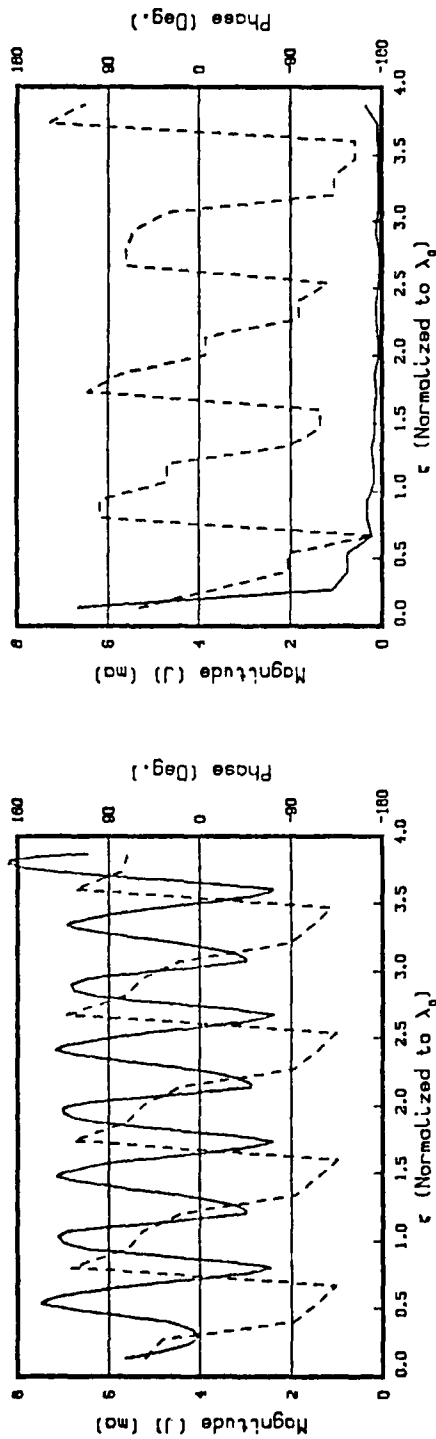


(b) JRAD Current Distributions on CUT RA

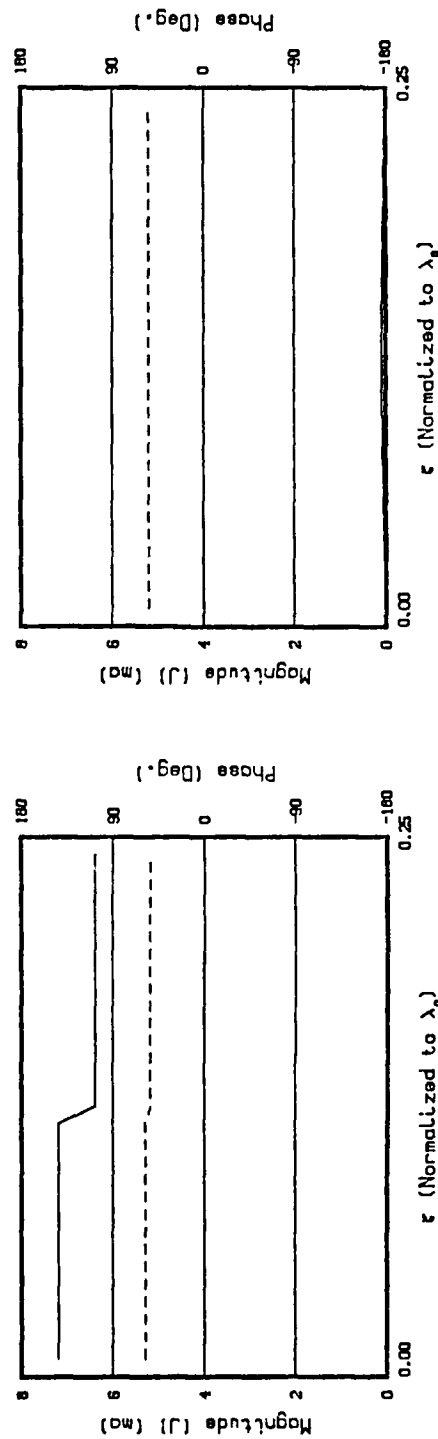


(d) JRAD Current Distributions on CUT BB

Figure C.10 Modeled Currents When Height = $1.50\lambda_0$ and Length = $3\lambda_0$.

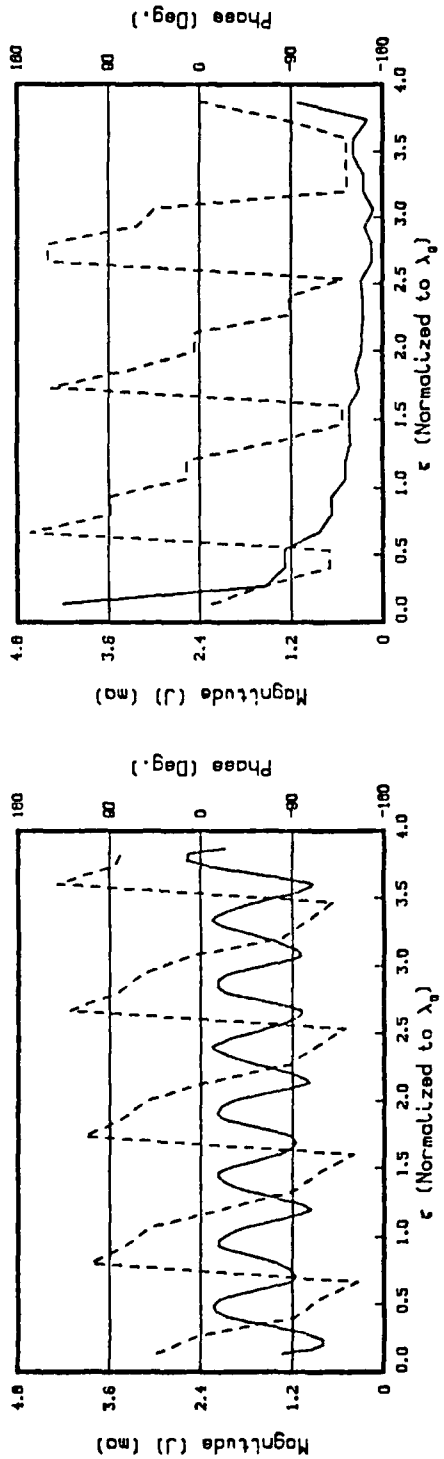


(b) J_{RR} Current Distributions on CUT AA

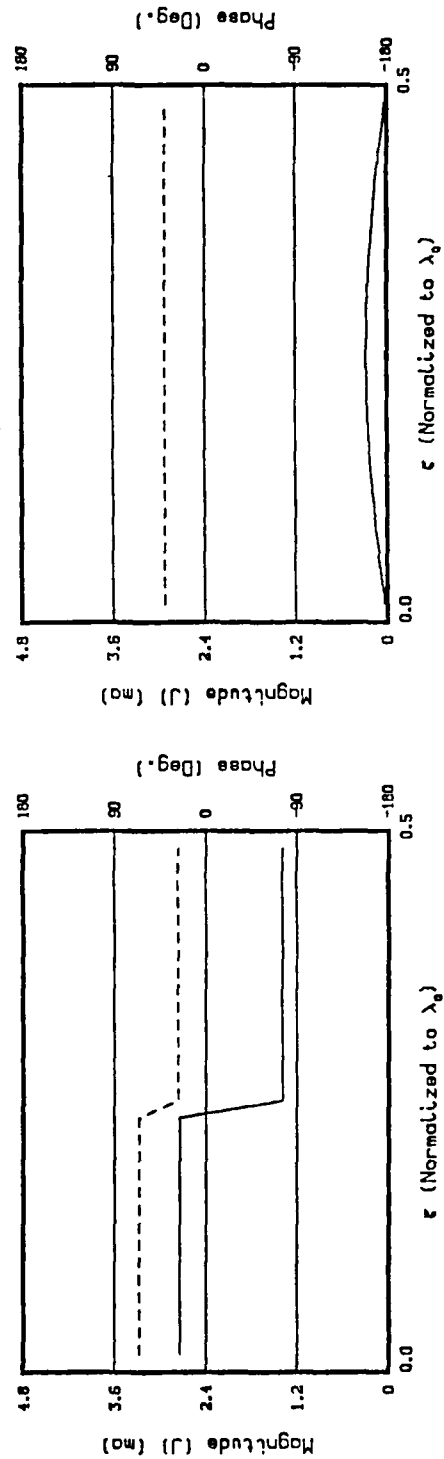


(d) J_{RR} Current Distributions on CUT BB

Figure C.11 Modeled Currents When Height = $0.25\lambda_0$ and Length = $4\lambda_0$.

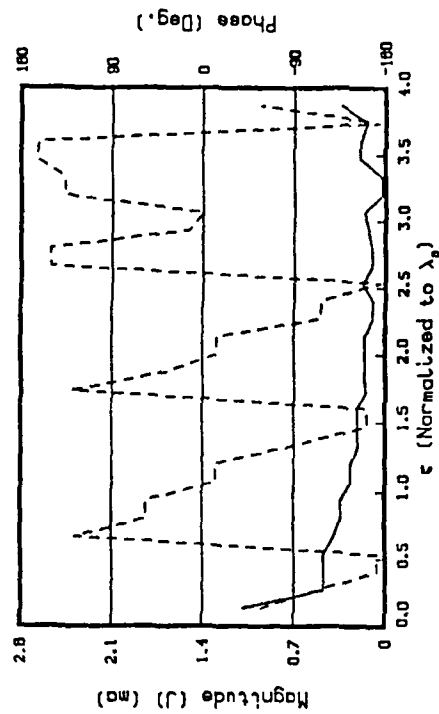


(b) JRAD Current Distributions on CUT AA

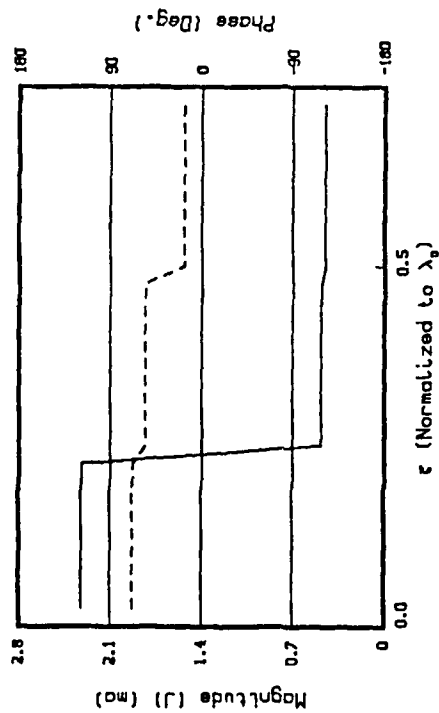


(d) JRAD Current Distributions on CUT BB

Figure C.12 Modeled Currents When Height = $0.50\lambda_0$ and Length = $4\lambda_0$.

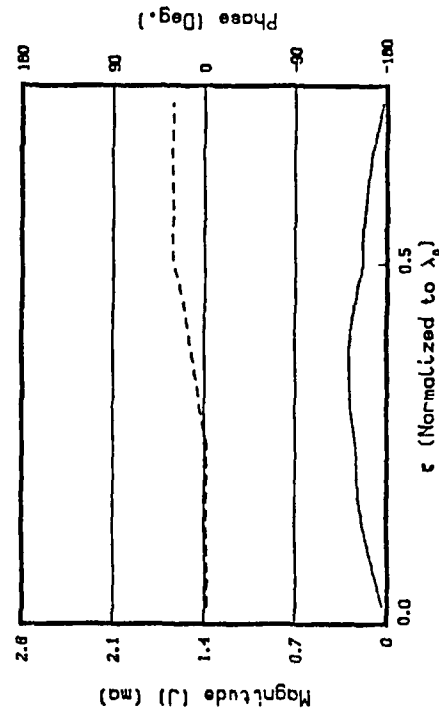


(a) JTRA Current Distributions on CUT AA



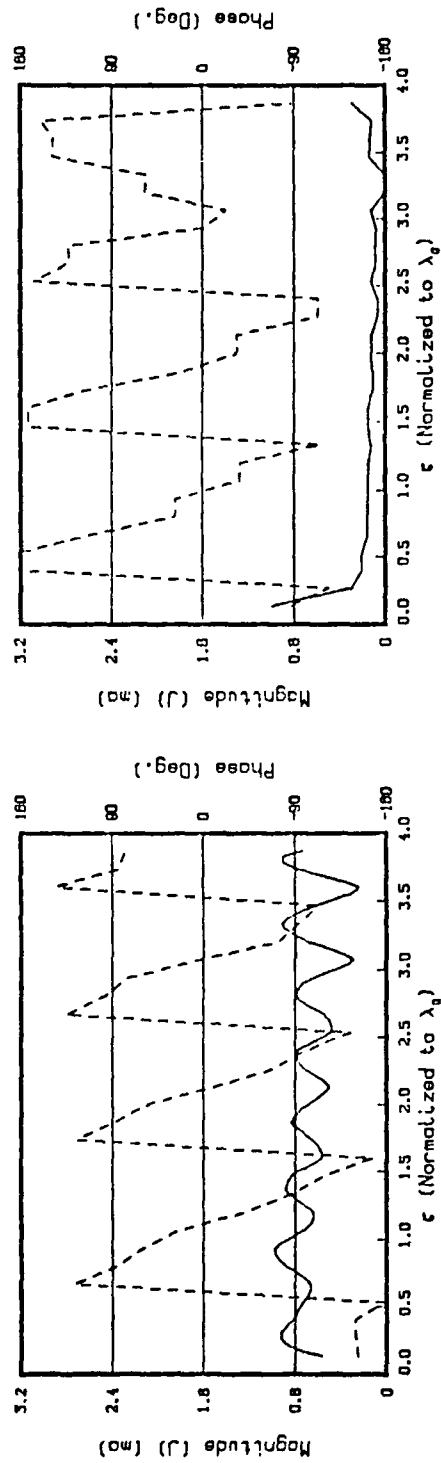
(c) JTRA Current Distributions on CUT BB

(b) JRAD Current Distributions on CUT AA

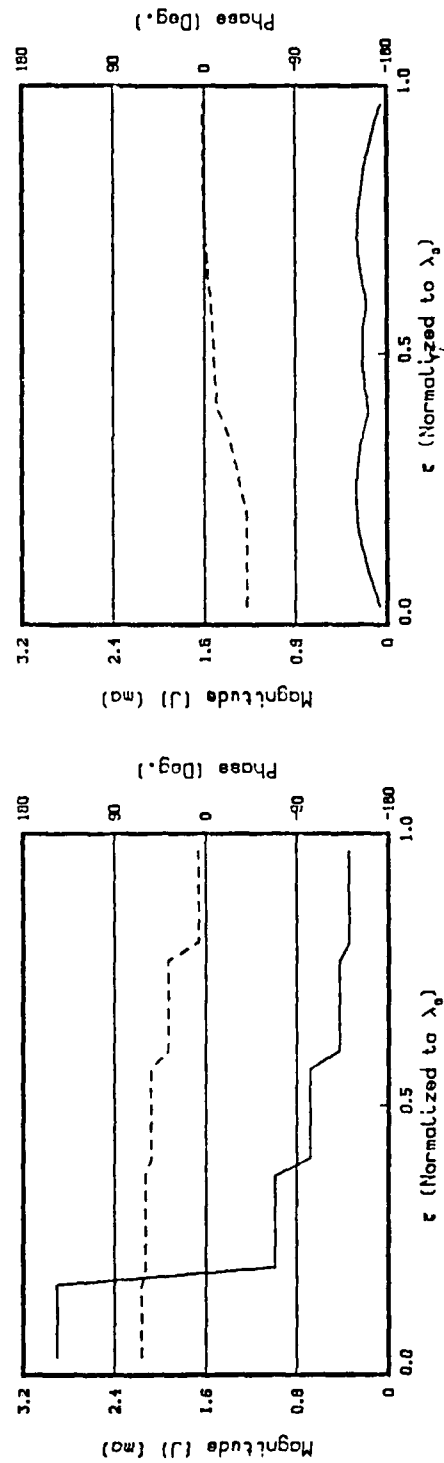


(d) JRAD Current Distributions on CUT BB

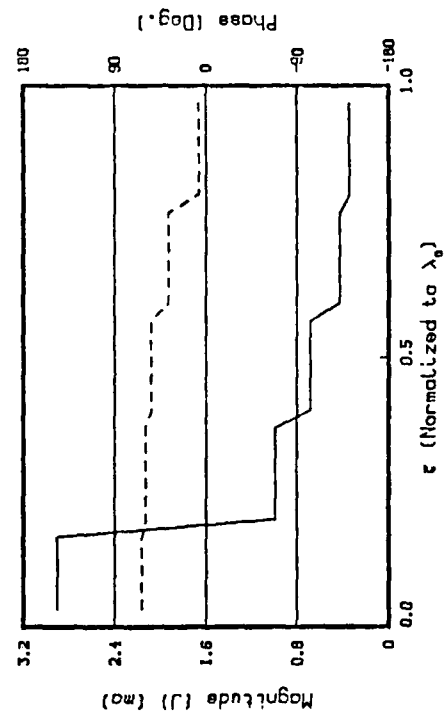
Figure C.13 Modeled Currents When Height = $0.75\lambda_0$ and Length = $4\lambda_0$.



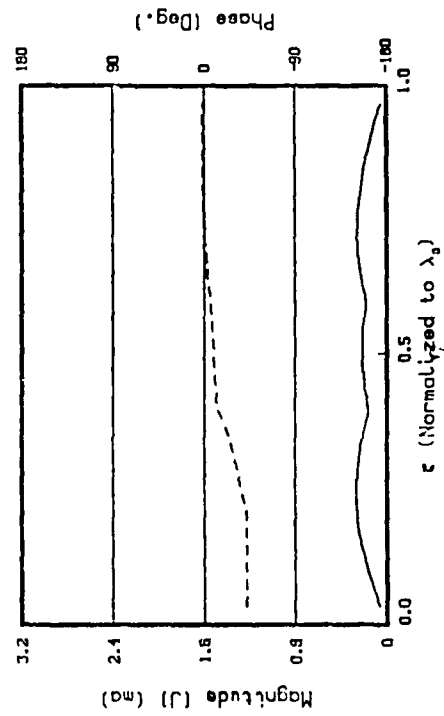
(a) JTRA Current Distributions on CUT RA



(b) JRAD Current Distributions on CUT RA

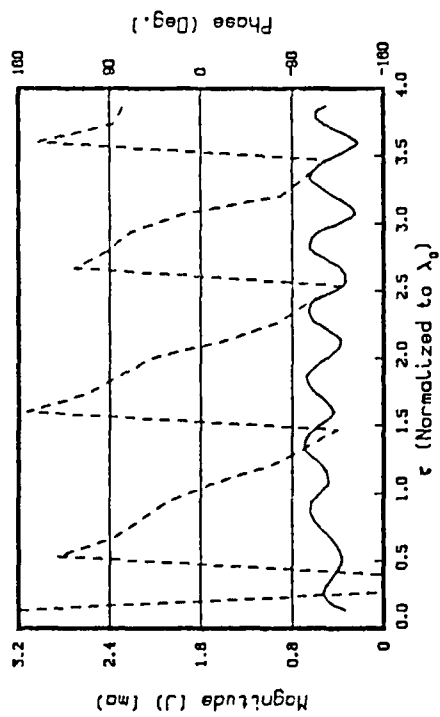


(c) JTRA Current Distributions on CUT BB

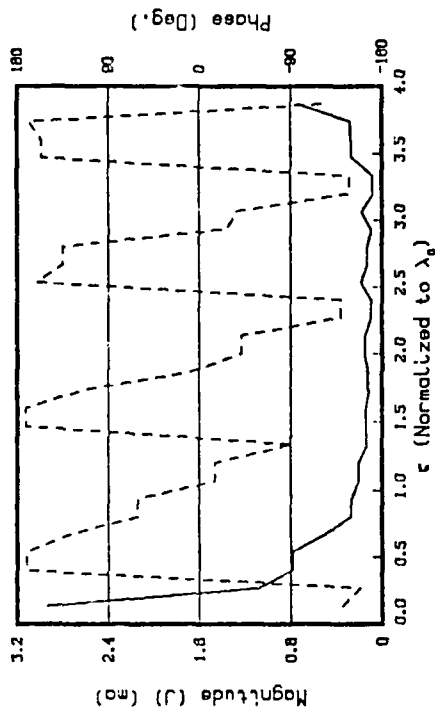


(d) JRAD Current Distributions on CUT BB

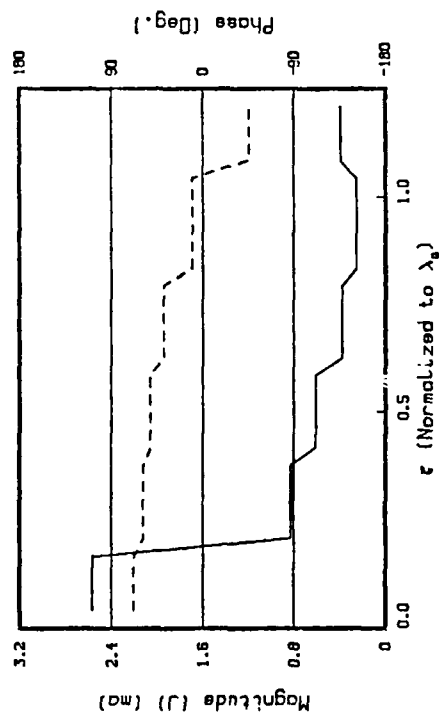
Figure C.14 Modeled Currents When Height = $1.00\lambda_0$ and Length = $4\lambda_0$.



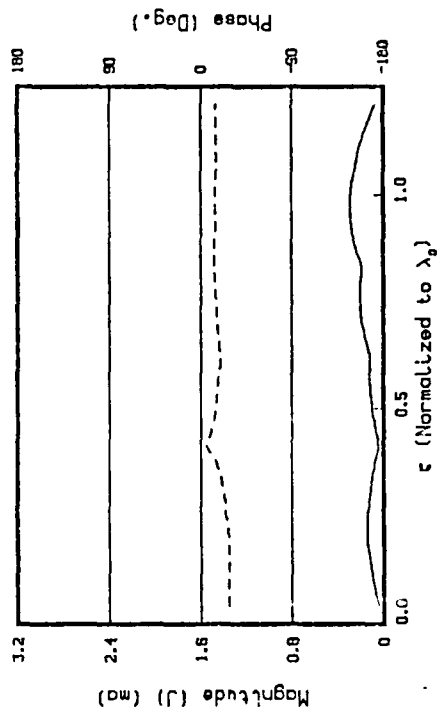
(a) JTR Current Distributions on CUT RA



(b) JRAD Current Distributions on CUT RA

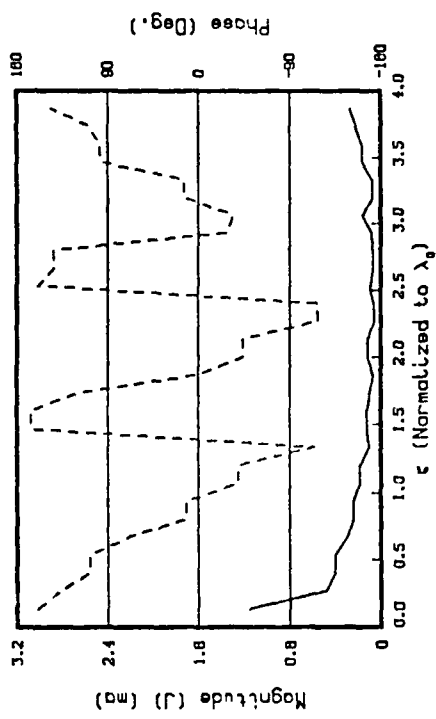


(c) JTR Current Distributions on CUT BB

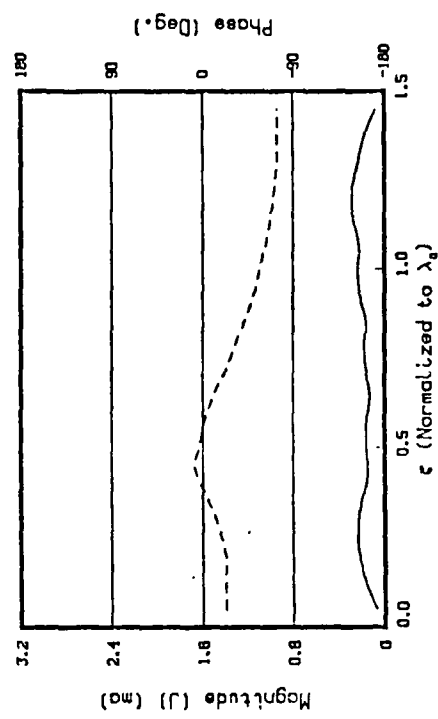


(d) JRAD Current Distributions on CUT BB

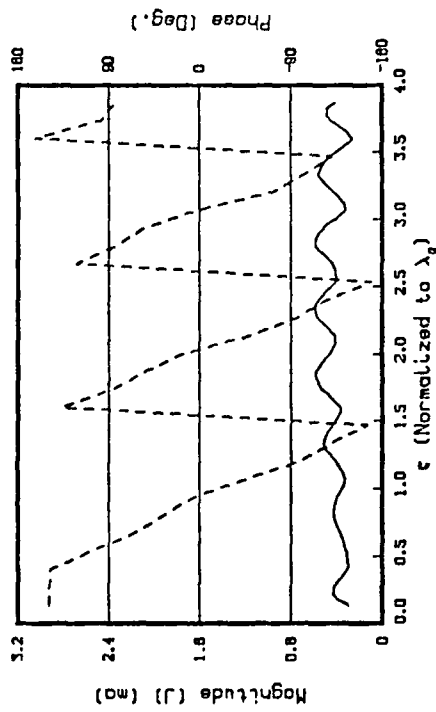
Figure C.15 Modeled Currents When Height = $1.25\lambda_0$ and Length = $4\lambda_0$.



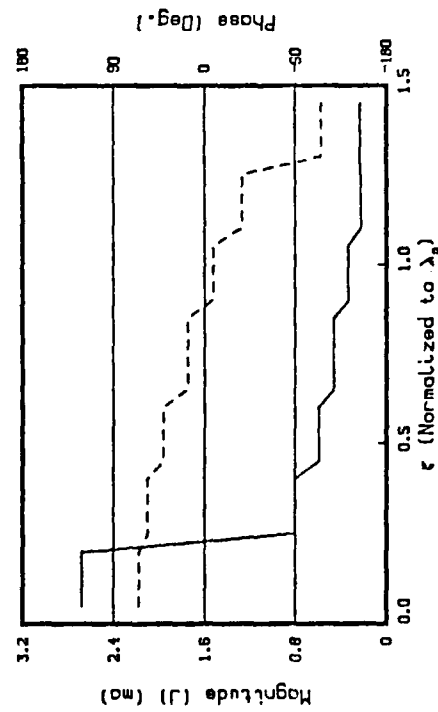
(a) JTRA Current Distributions on CUT AA



(b) JRAD Current Distributions on CUT AA

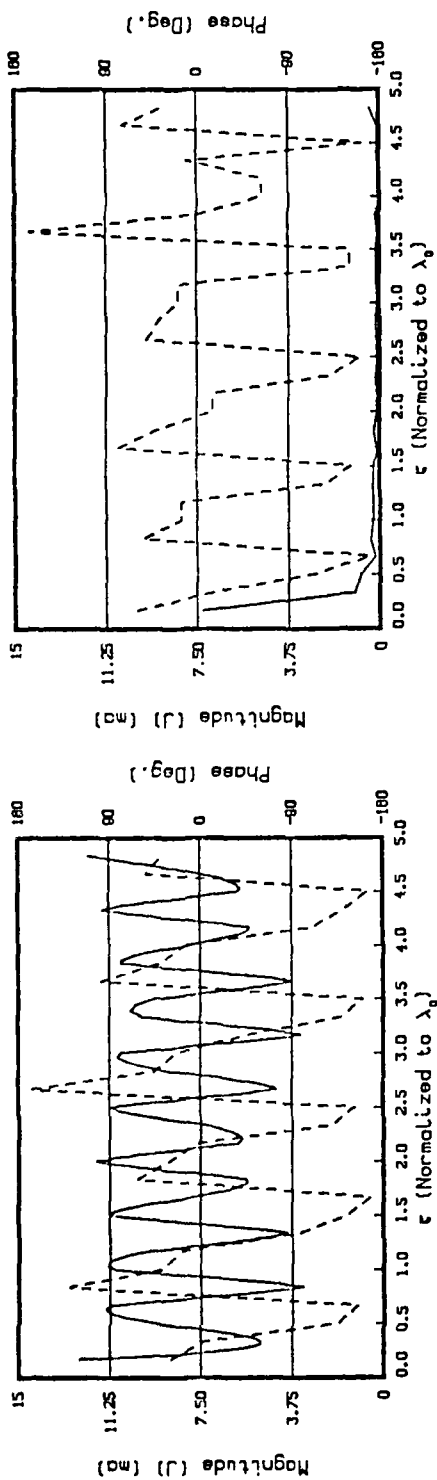


(c) JTRA Current Distributions on CUT BB



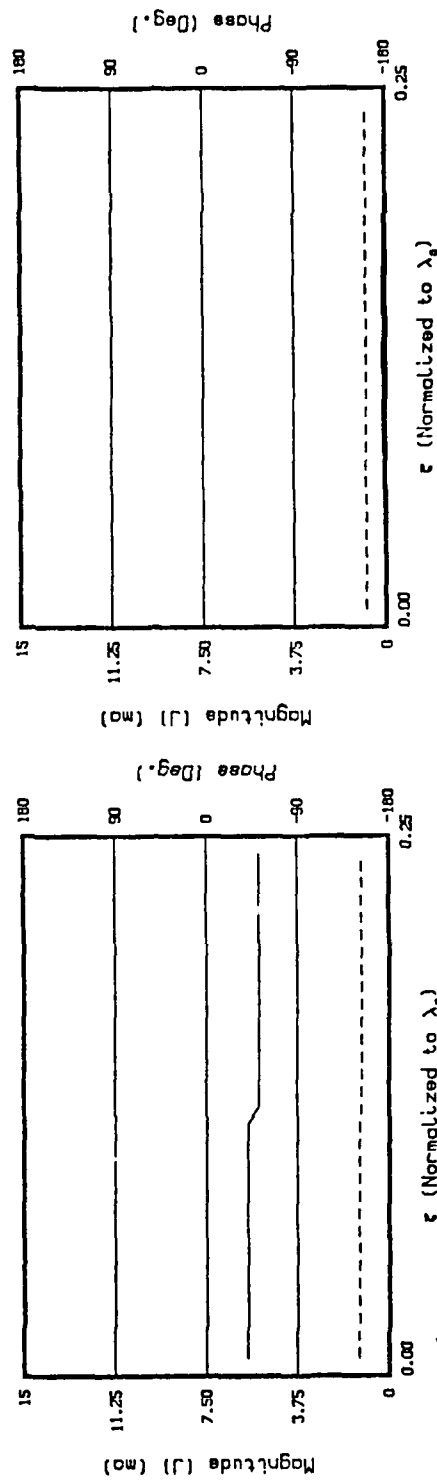
(d) JRAD Current Distributions on CUT BB

Figure C.16 Modeled Currents When Height = $1.50\lambda_0$ and Length = $4\lambda_0$.



(a) JTRR Current Distributions on CUT AR

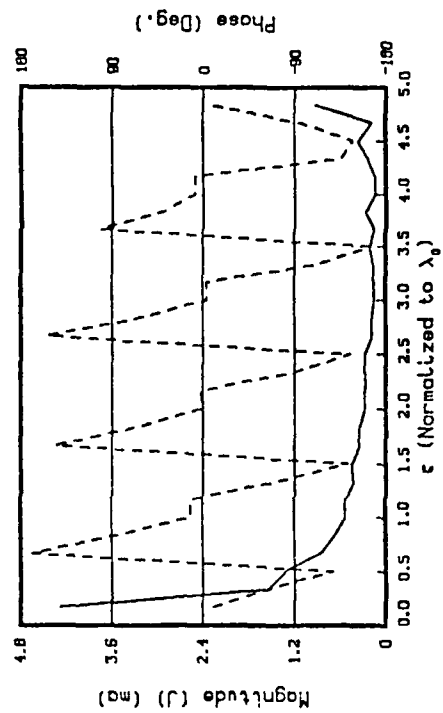
(b) JRRD Current Distributions on CUT AR



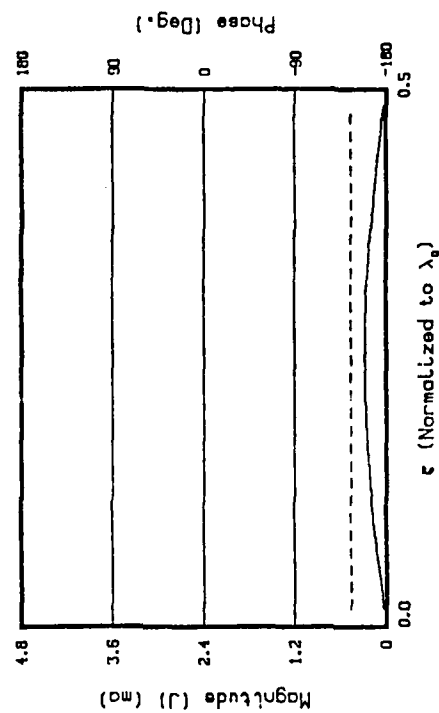
(c) JTRR Current Distributions on CUT BB

(d) JRRD Current Distributions on CUT BB

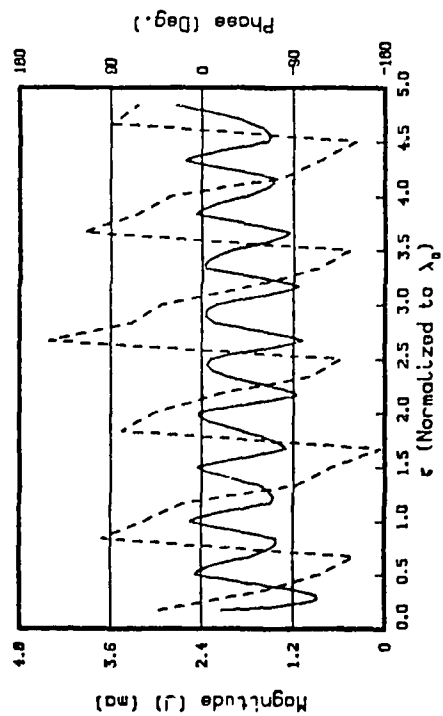
Figure C.17 Modeled Currents When Height = $0.25\lambda_0$ and Length = $5\lambda_0$.



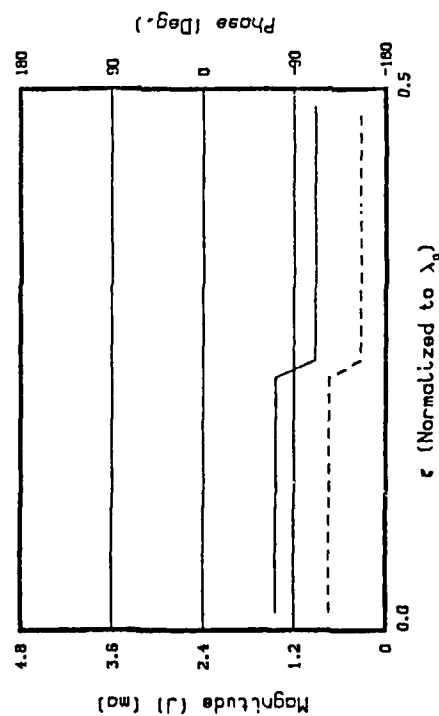
(a) JTRR Current Distributions on CUT AA



(b) JTRR Current Distributions on CUT BB

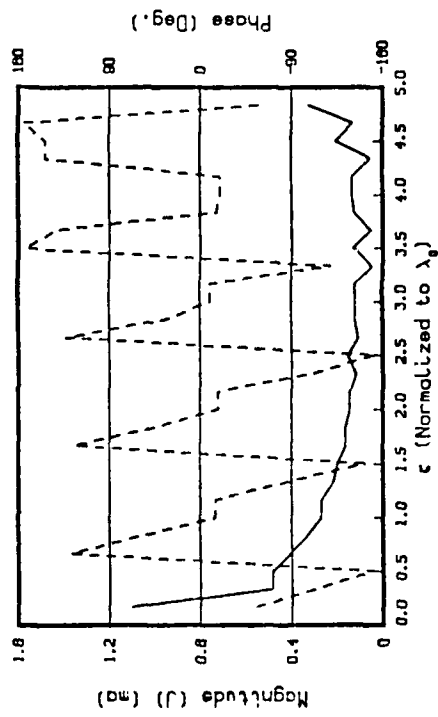


(c) JTRR Current Distributions on CUT AA

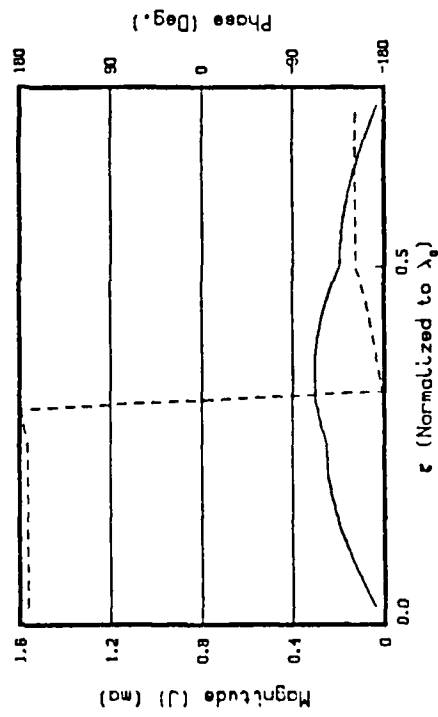


(d) JTRR Current Distributions on CUT BB

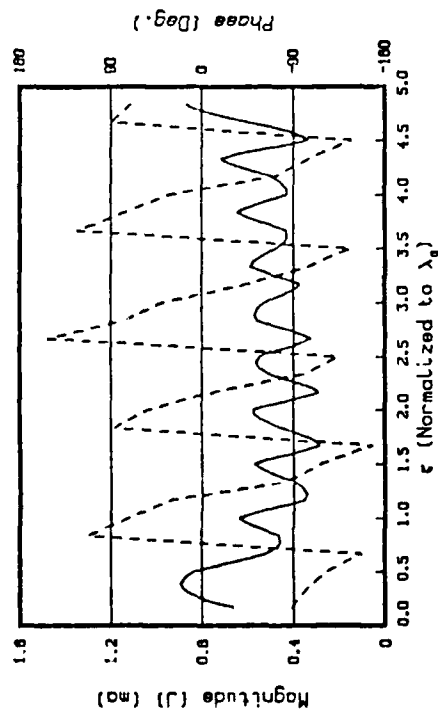
Figure C.18 Modeled Currents When Height = $0.50\lambda_0$ and Length = $5\lambda_0$.



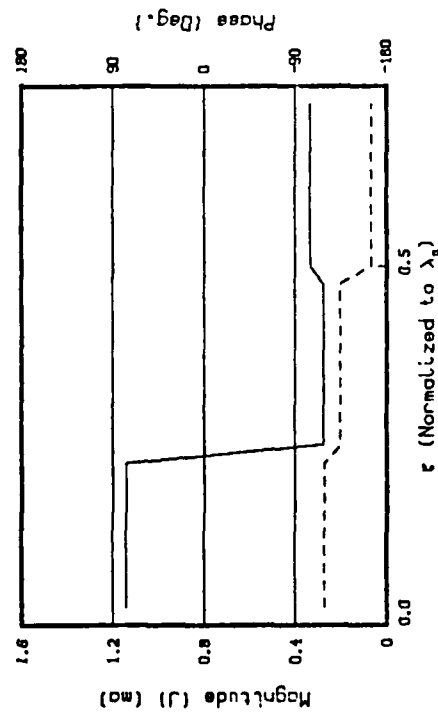
(a) JTR Current Distributions on CUT RA



(b) JTR Current Distributions on CUT BB

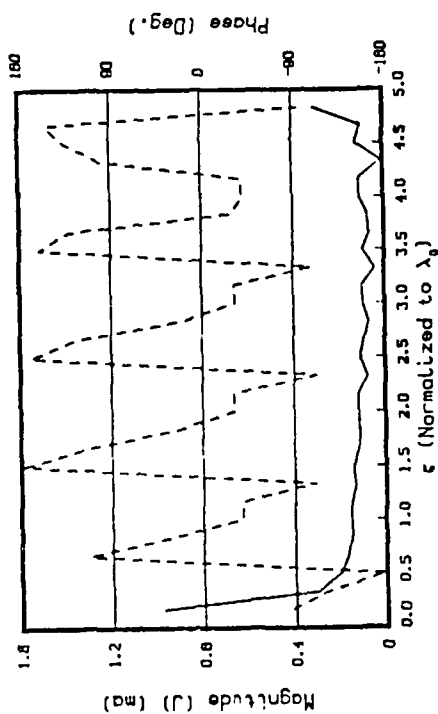


(c) JTR Current Distributions on CUT RA

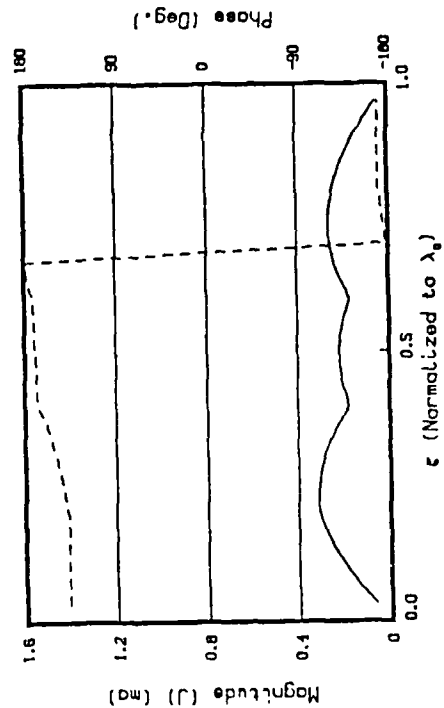


(d) JTR Current Distributions on CUT BB

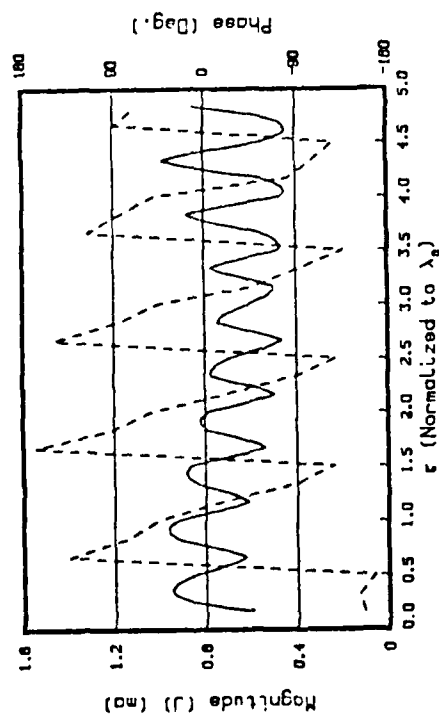
Figure C.19 Modeled Currents when Height = $0.75\lambda_0$ and Length = $5\lambda_0$.



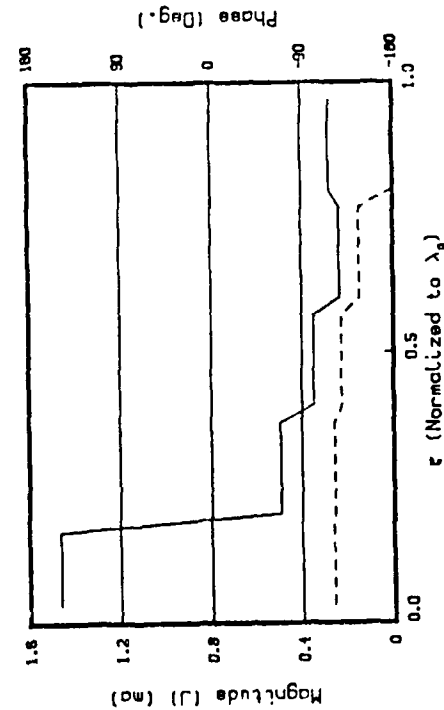
(a) JTRA Current Distributions on CUT RA



(b) JTRA Current Distributions on CUT RA

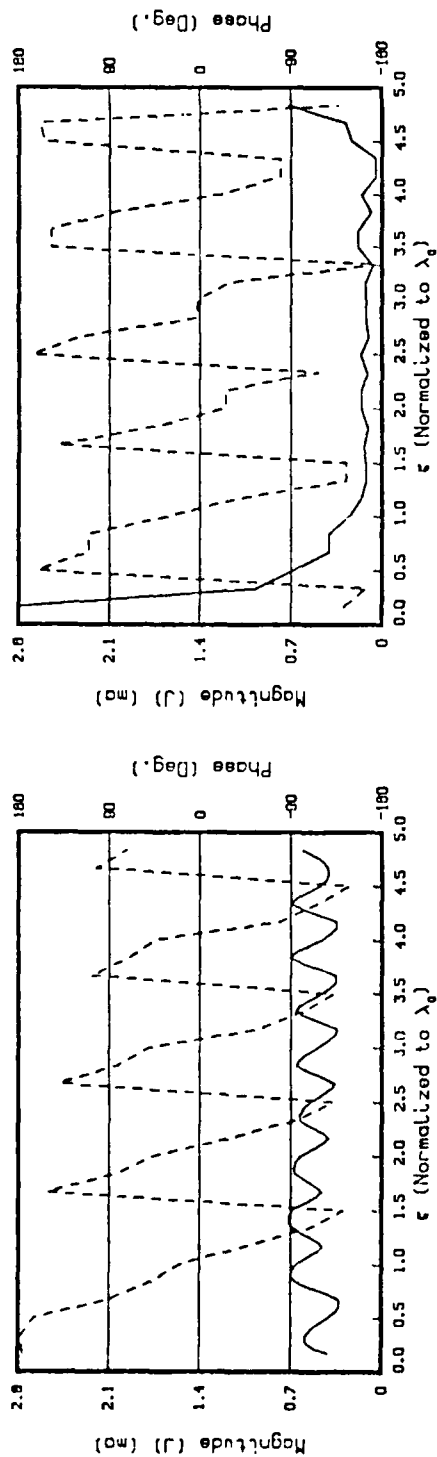


(c) JTRA Current Distributions on CUT BB

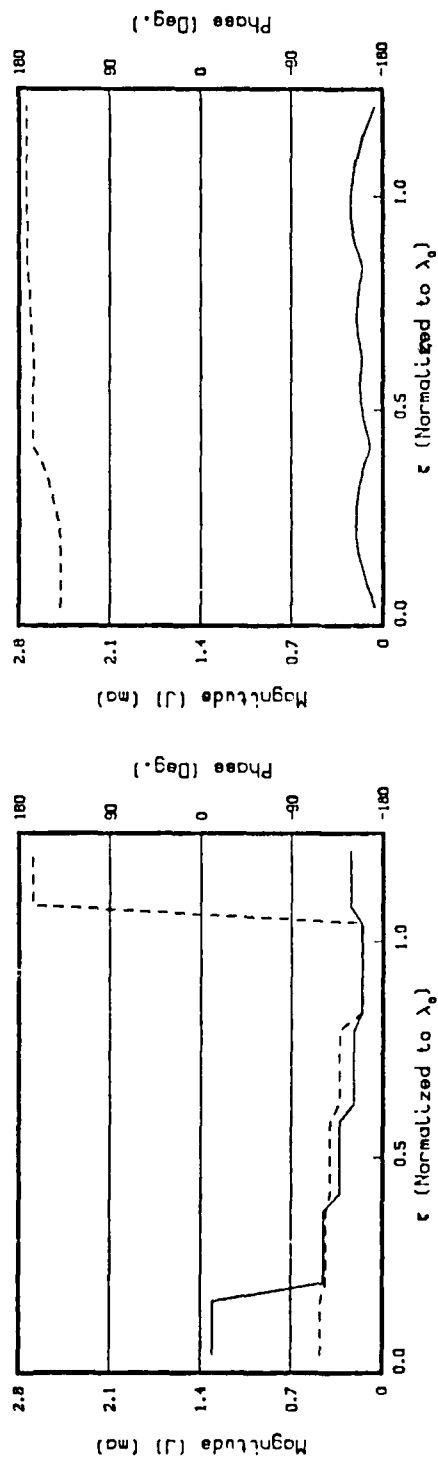


(d) JTRA Current Distributions on CUT BB

Figure C.20 Modeled Currents When Height = $1.00\lambda_0$ and Length = $5\lambda_0$.

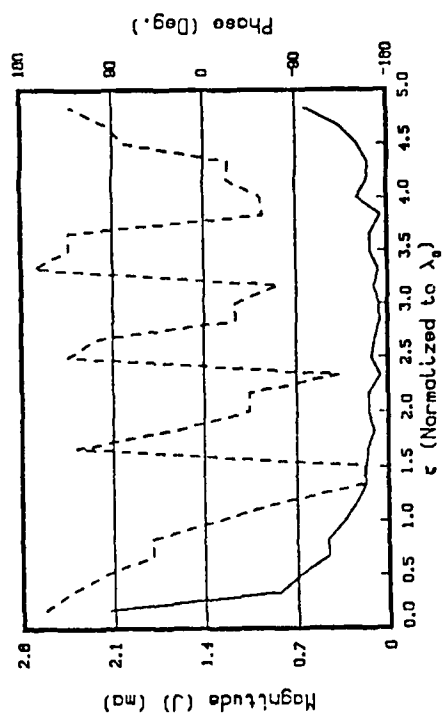


(b) J_{RAQ} Current Distributions on CUT RA

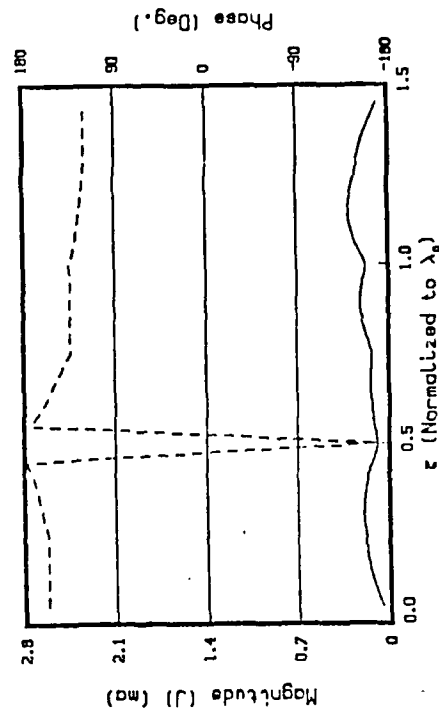


(d) J_{RAQ} Current Distributions on CUT BB

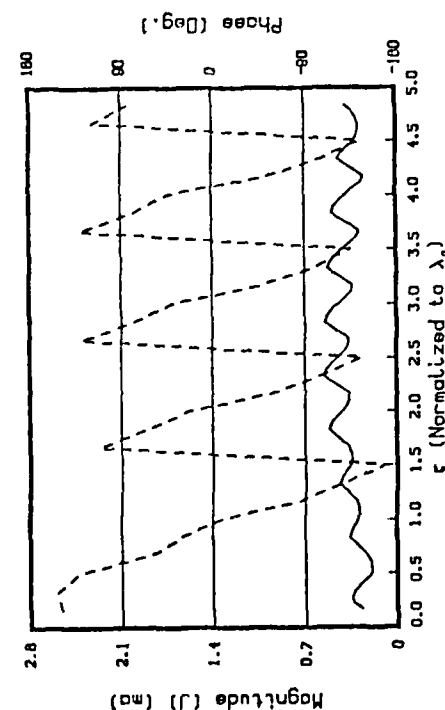
Figure C.21 Modeled Currents When Height = $1.25\lambda_0$ and Length = $5\lambda_0$.



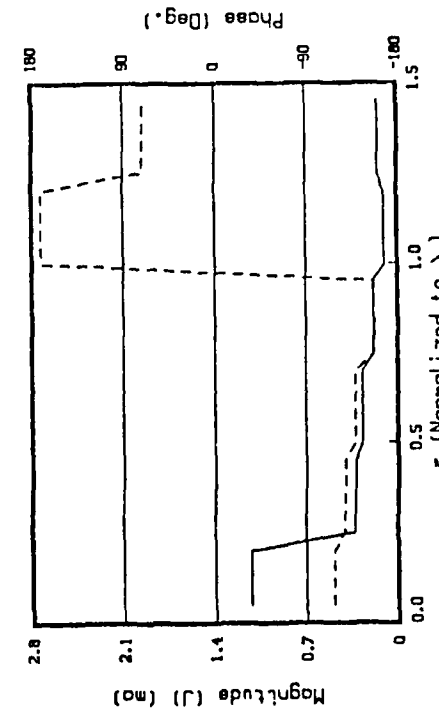
(a) JTRA Current Distributions on CUT AA



(b) JTRA Current Distributions on CUT BB

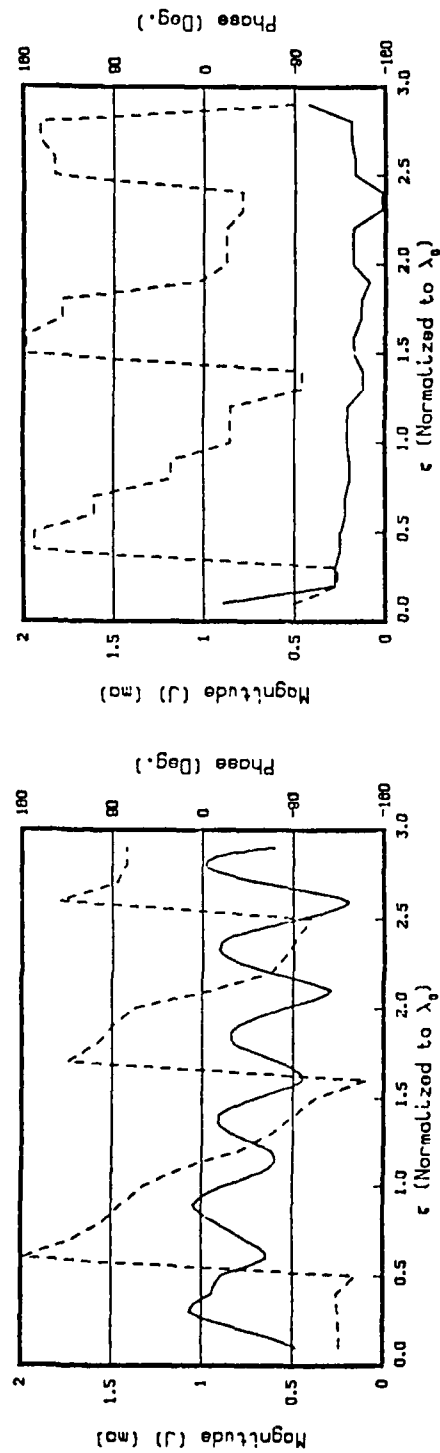


(c) JTRA Current Distributions on CUT AA

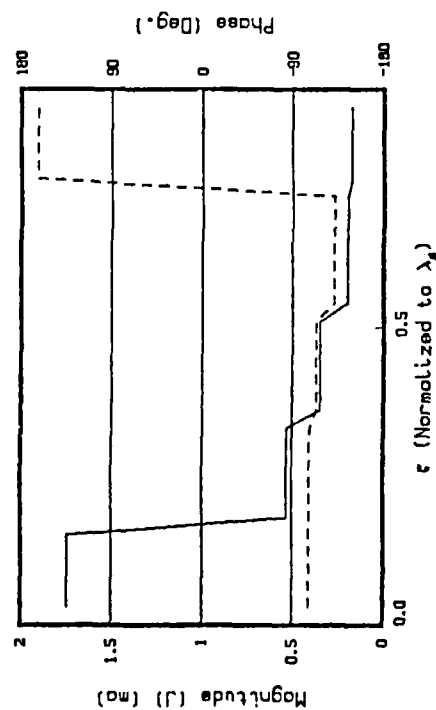


(d) JTRA Current Distributions on CUT BB

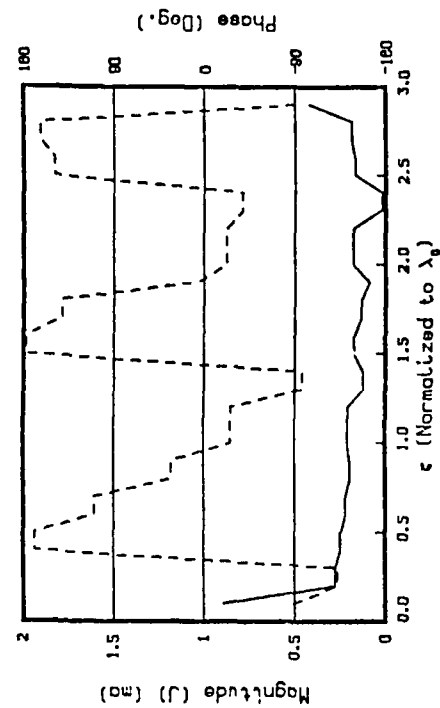
Figure C.22 Modeled Currents When Haight = $1.50\lambda_0$ and Length = $5\lambda_0$.



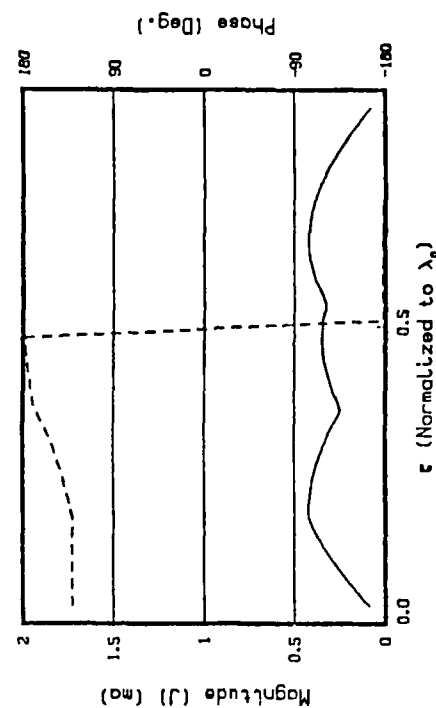
(a) JTRA Current Distributions on CUT AA



(c) JTRA Current Distributions on CUT BB

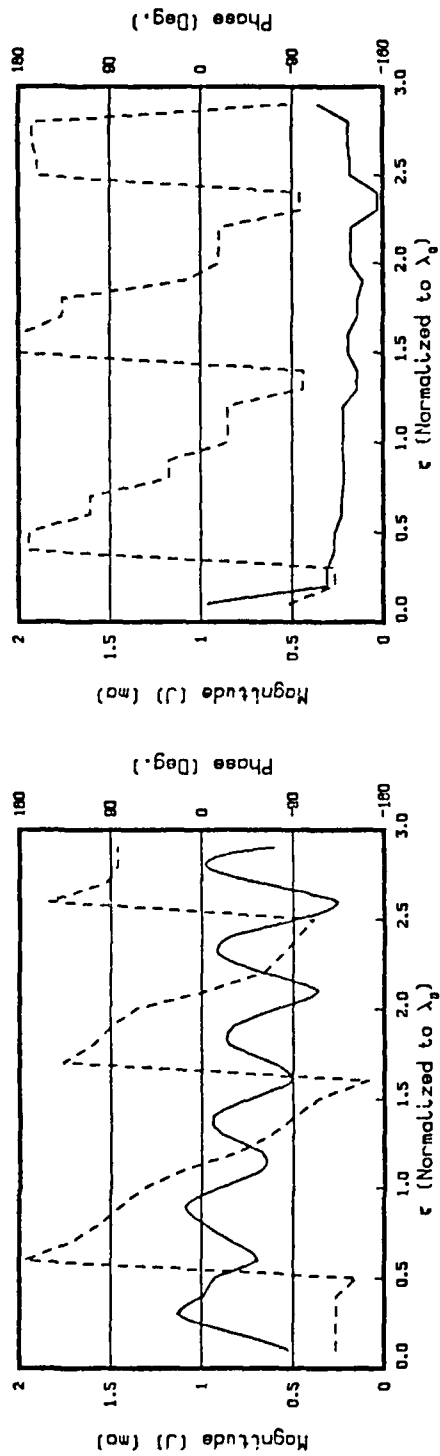


(b) JRAO Current Distributions on CUT AA

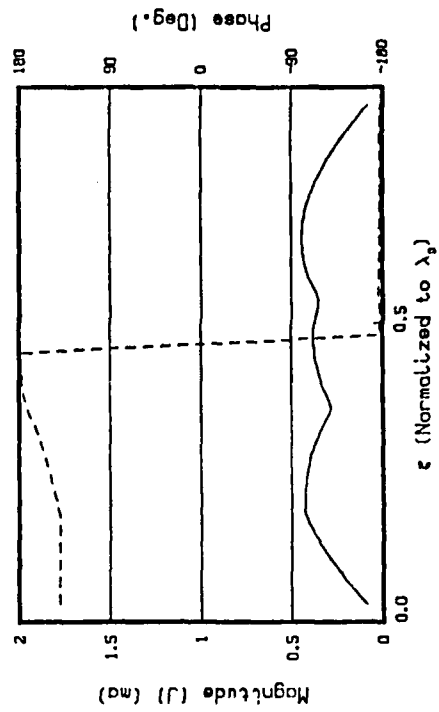


(d) JRAO Current Distributions on CUT BB

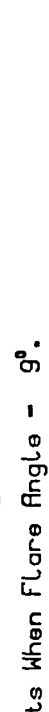
Figure C.23 Modeled Currents When Flare Angle = 6° .



(b) JRAD Current Distributions on CUT AA



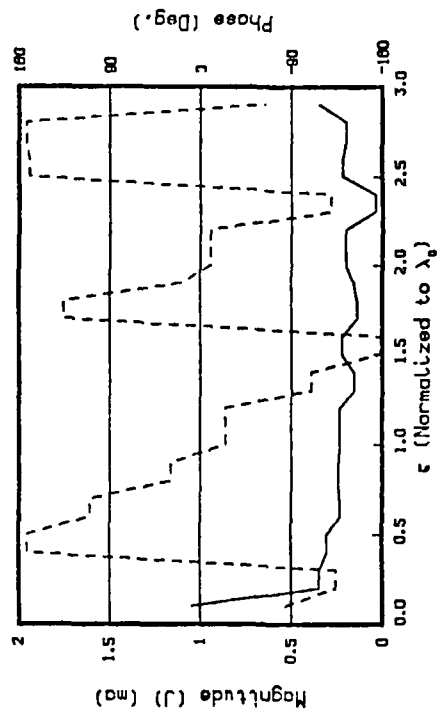
(c) JTRA Current Distributions on CUT BB



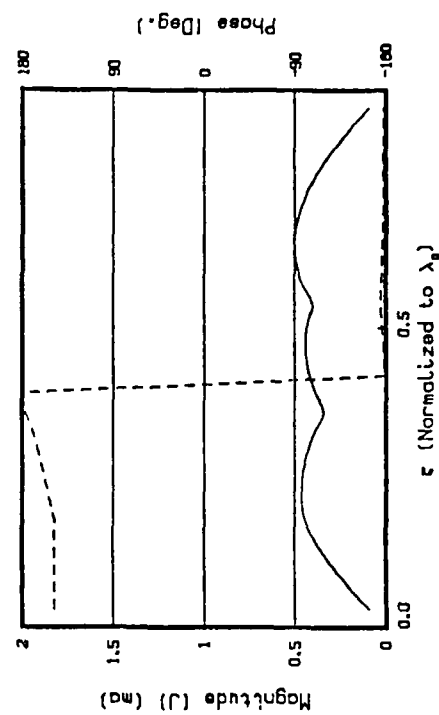
(d) JRAD Current Distributions on CUT BB



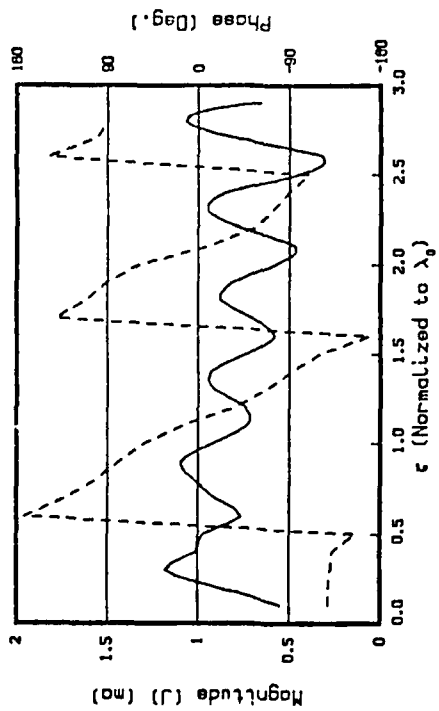
Figure C.24 Modeled Currents When Flare Angle = 9°



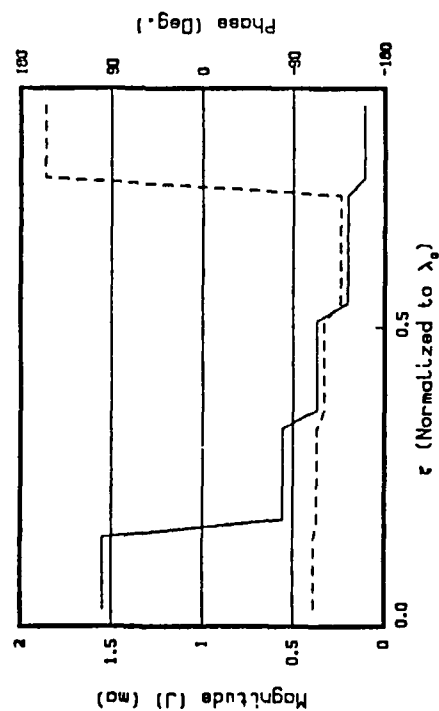
(a) JTRA Current Distributions on CUT AA



(b) JRAD Current Distributions on CUT AA

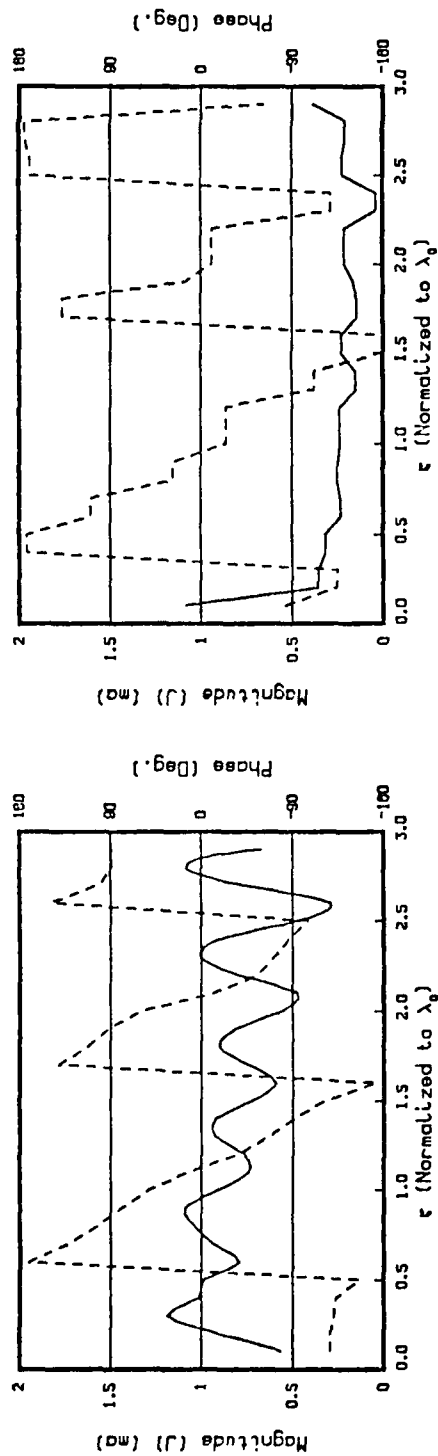


(c) JTRA Current Distributions on CUT BB

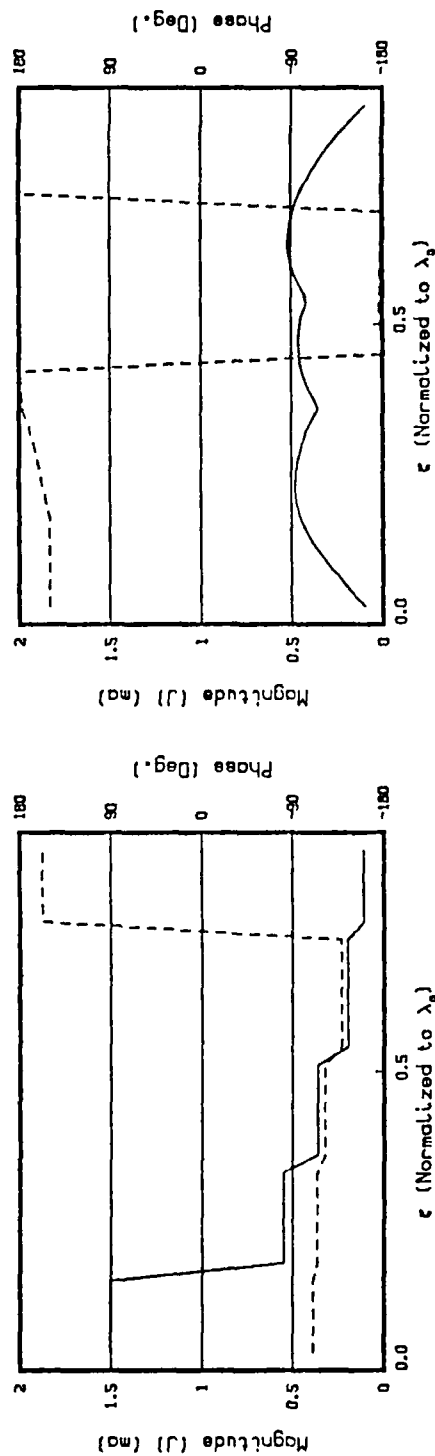


(d) JRAD Current Distributions on CUT BB

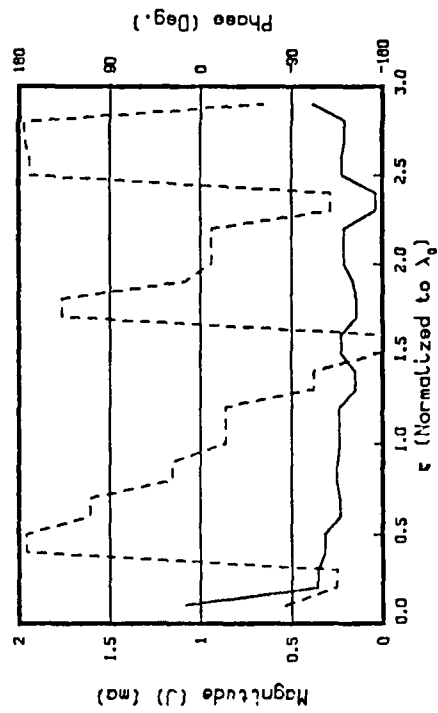
Figure C.25 Modeled Currents When Flare Angle = 15°



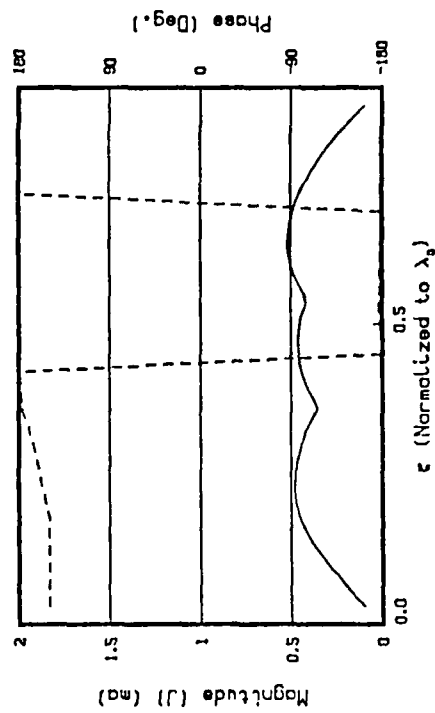
(a) JTRA Current Distributions on CUT AA



(c) JTRA Current Distributions on CUT BB

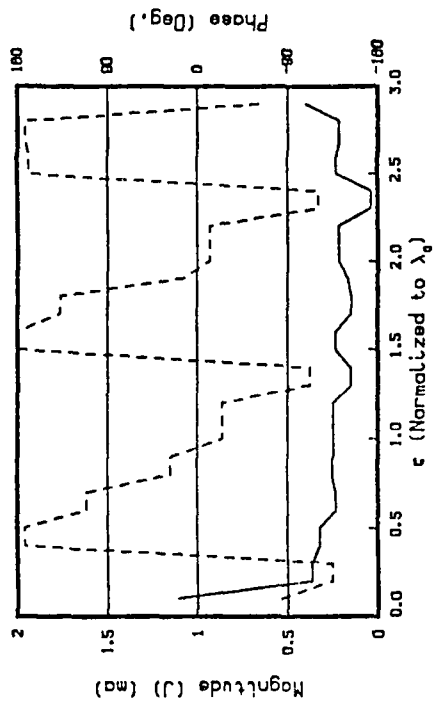


(b) JRAQ Current Distributions on CUT AA

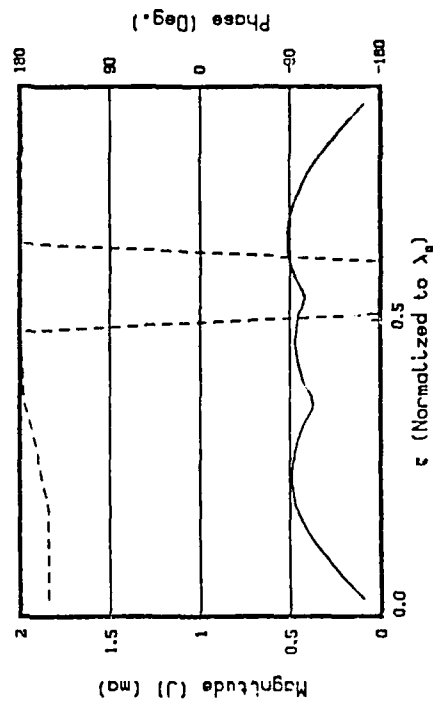


(d) JRAQ Current Distributions on CUT BB

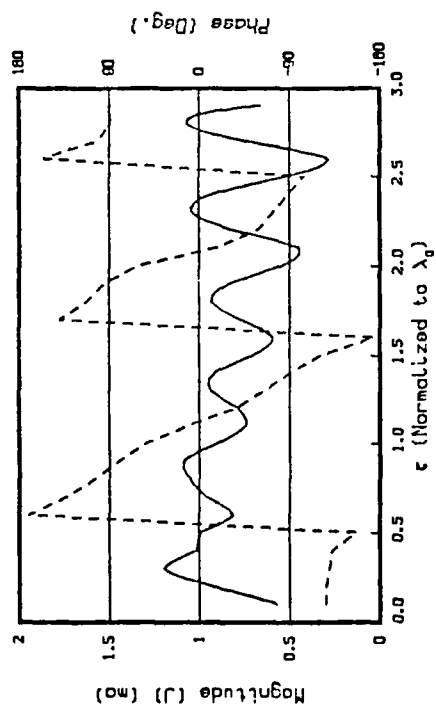
Figure C.26 Modeled Currents When Flare Angle = 18°.



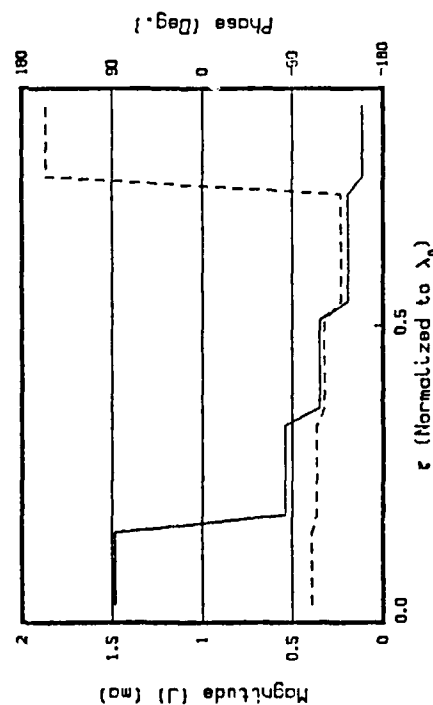
(a) JTRA Current Distributions on CUT AA



(b) JTRA Current Distributions on CUT BB

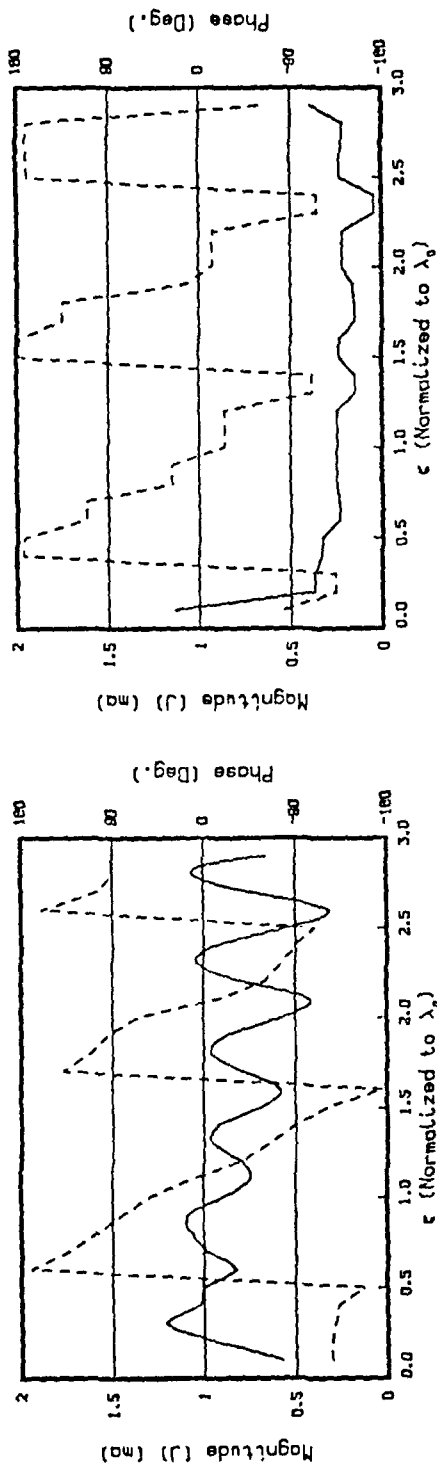


(c) JTRA Current Distributions on CUT AA

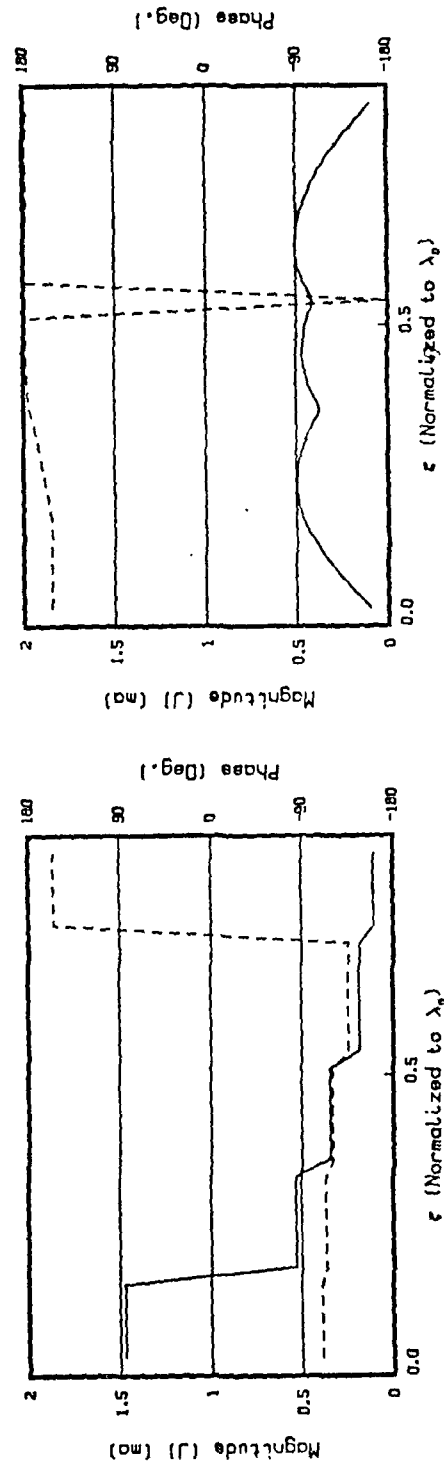


(d) JTRA Current Distributions on CUT BB

Figure C.27 Modeled Currents When Flare Angle = 21°



(a) JTRR Current Distributions on CUT RA

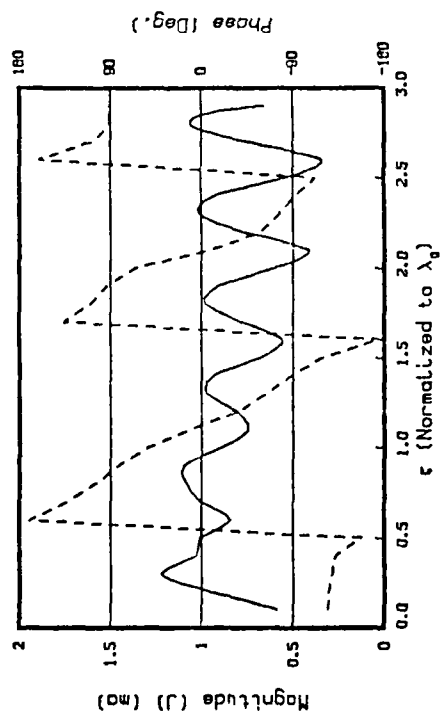


(b) JTRR Current Distributions on CUT RA

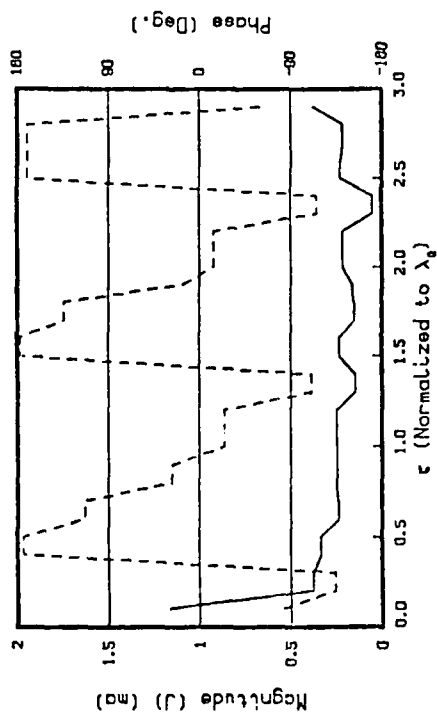
(c) JTRR Current Distributions on CUT BB

(d) JTRR Current Distributions on CUT BB

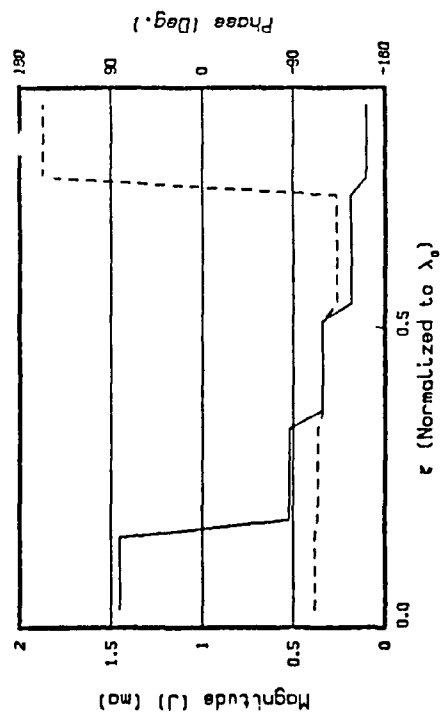
Figure C.28 Modeled Currents hen Flare Angle = 24°.



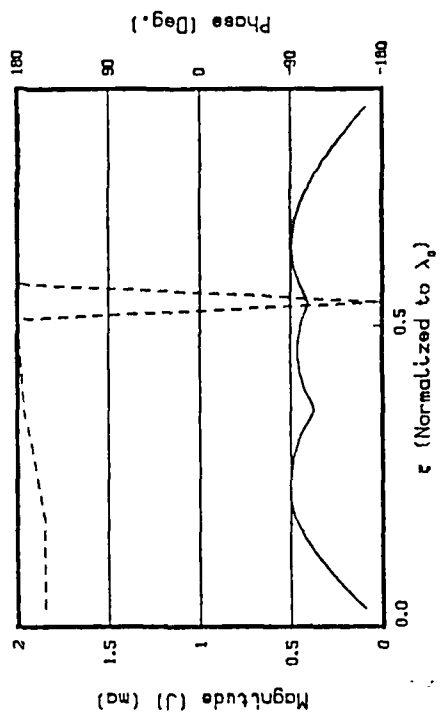
(a) JTRQ Current Distributions on CUT AA



(b) JTRQ Current Distributions on CUT AA

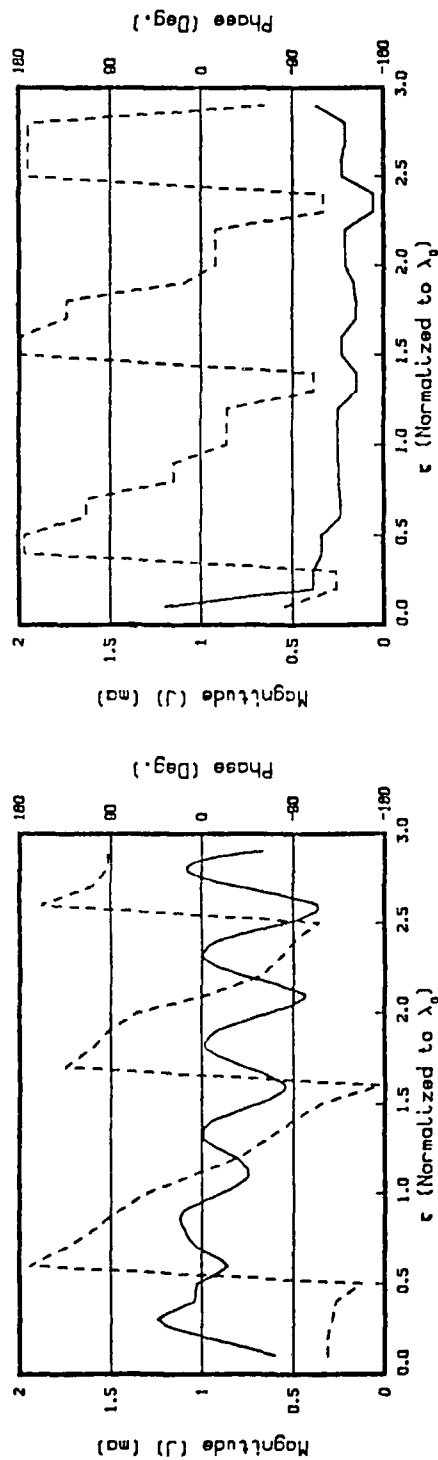


(c) JTRQ Current Distributions on CUT BB

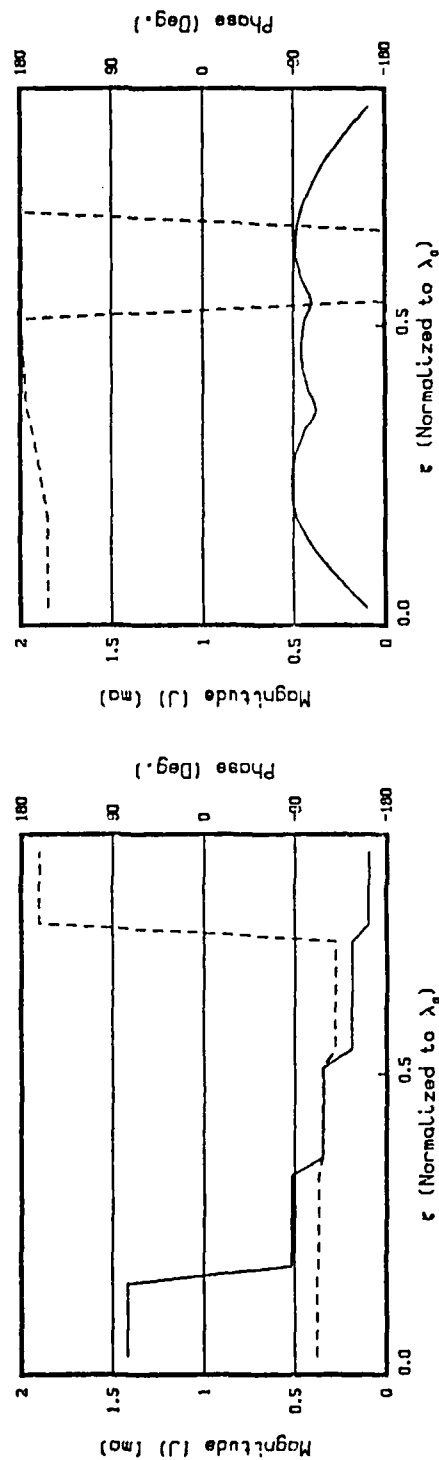


(d) JTRQ Current Distributions on CUT BB

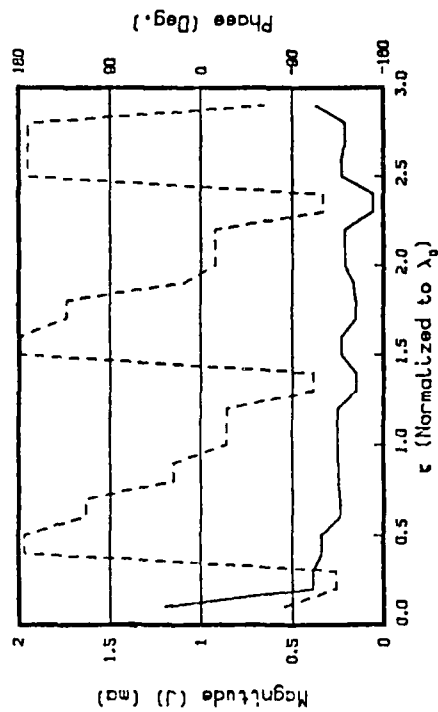
Figure C.29 Modeled Currents When Flare Angle = 27° .



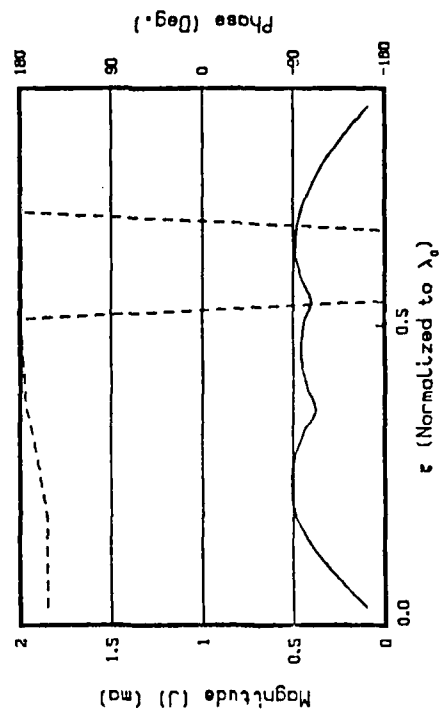
(a) JTRR Current Distributions on CUT AA



(b) JTRR Current Distributions on CUT BB

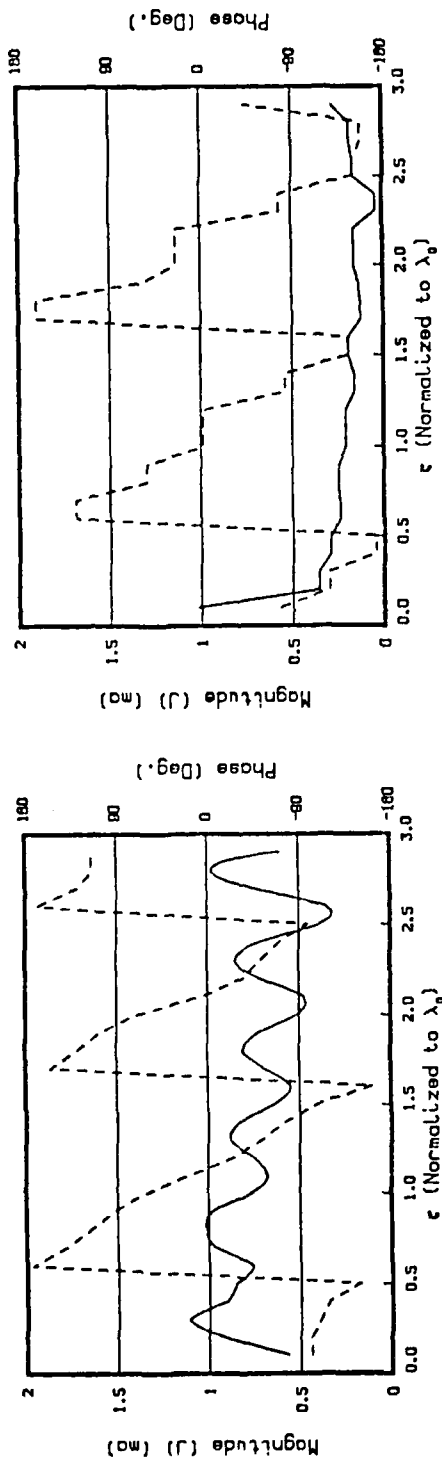


(c) JTRR Current Distributions on CUT AA

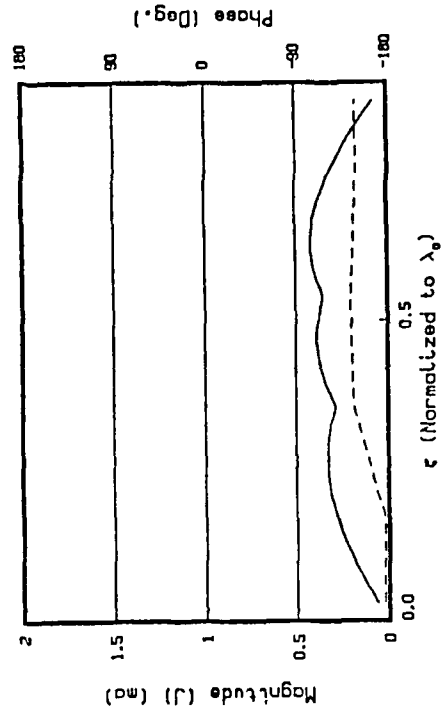


(d) JTRR Current Distributions on CUT BB

Figure C.30 Modeled Currents When Flare Angle = 30° .



(b) JRAD Current Distributions on CUT AA



(d) JRAD Current Distributions on CUT BB

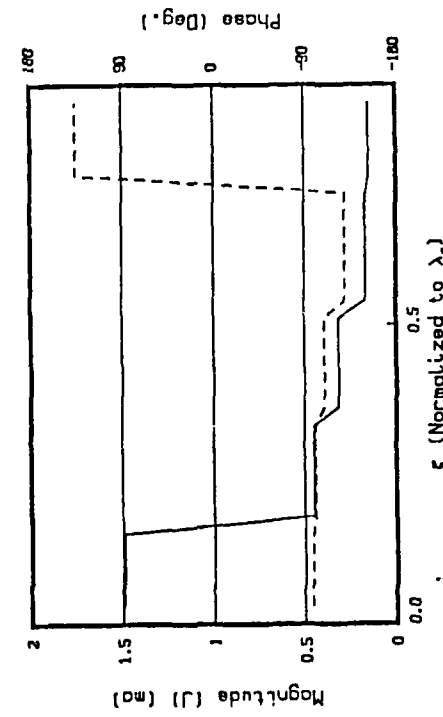
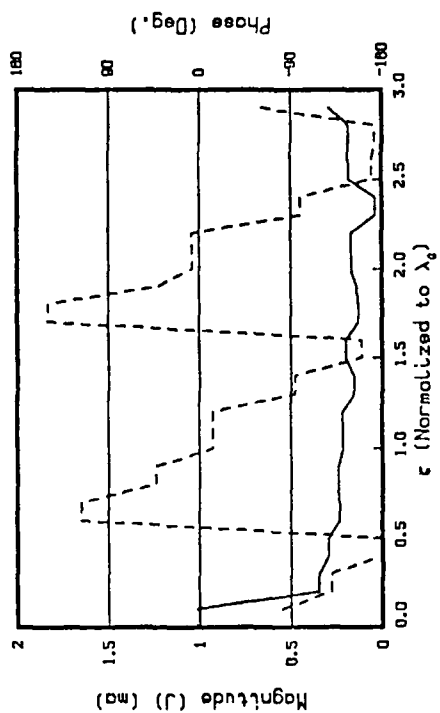
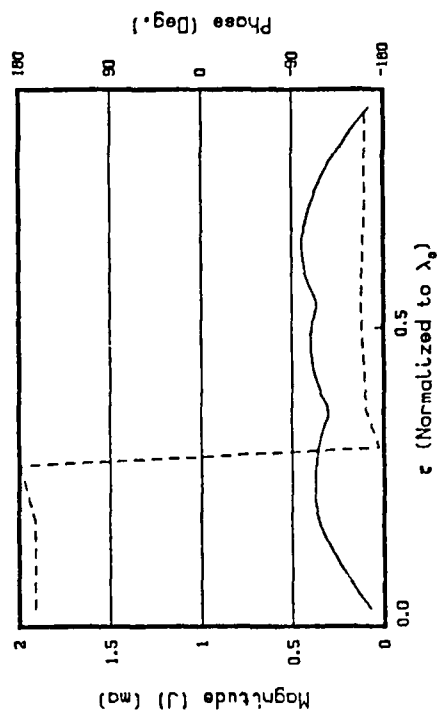


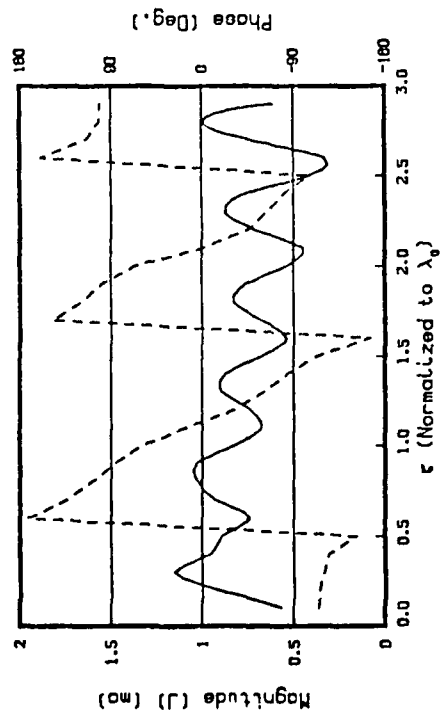
Figure C.31 Modeled Currents When Substrate Thickness = $.010\lambda_0$.



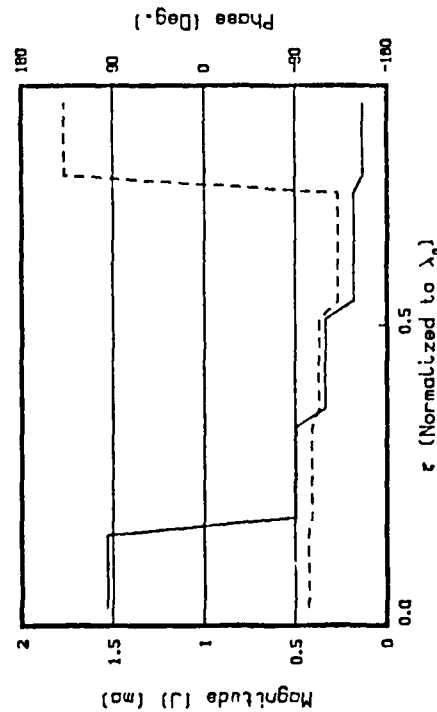
(a) JTRR Current Distributions on CUT AA



(b) JTRR Current Distributions on CUT BB

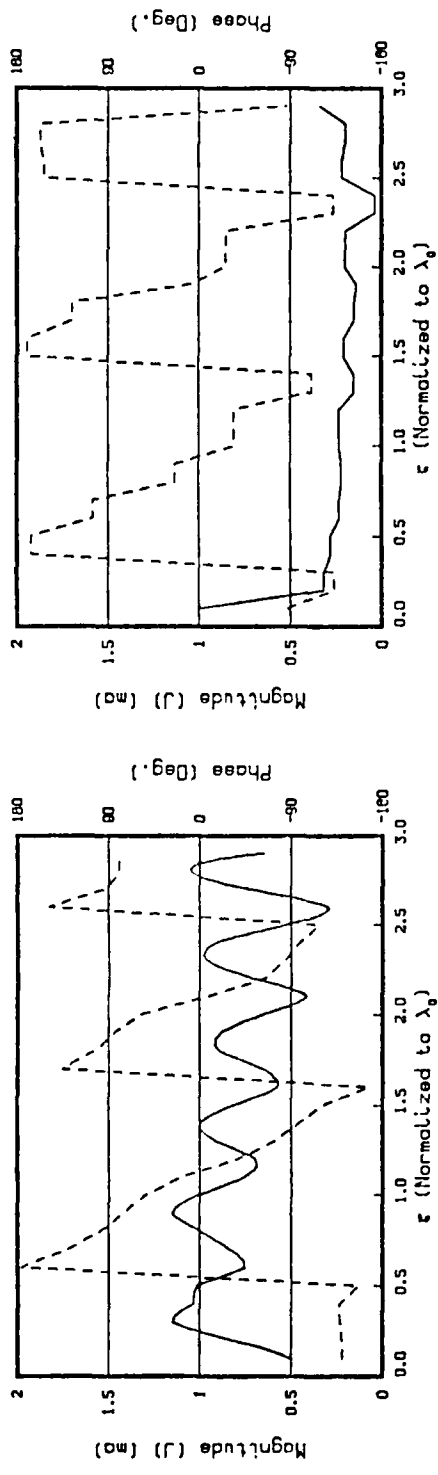


(c) JTRR Current Distributions on CUT AA

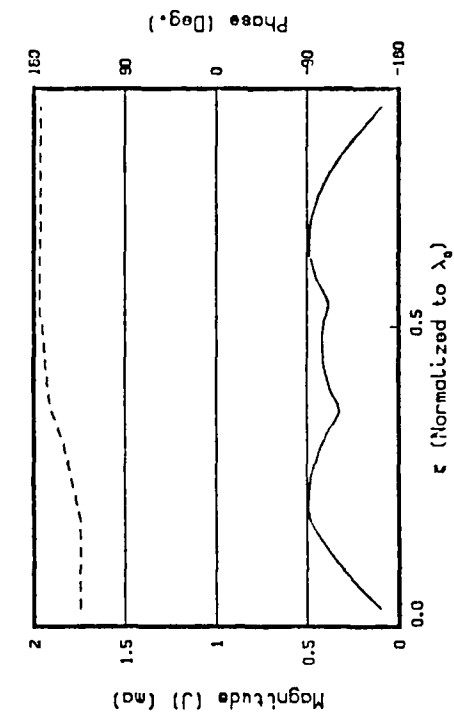


(d) JTRR Current Distributions on CUT BB

Figure C.32 Modeled Currents When Substrate Thickness = $.015\lambda_0$.



(b) JRAD Current Distributions on CUT RA



(d) JRAD Current Distributions on CUT BB

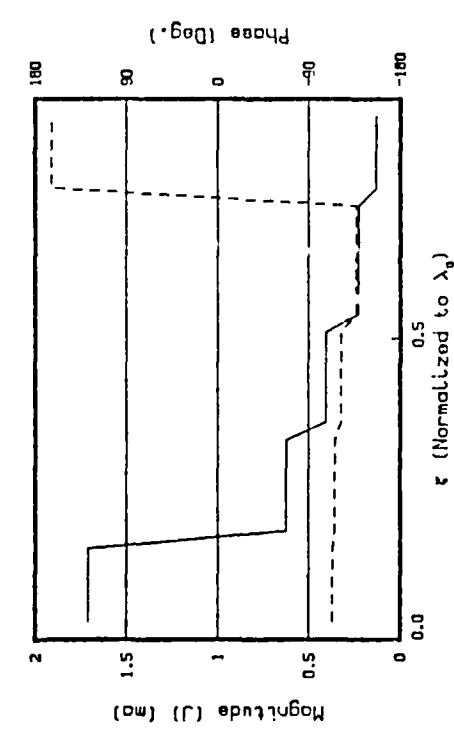
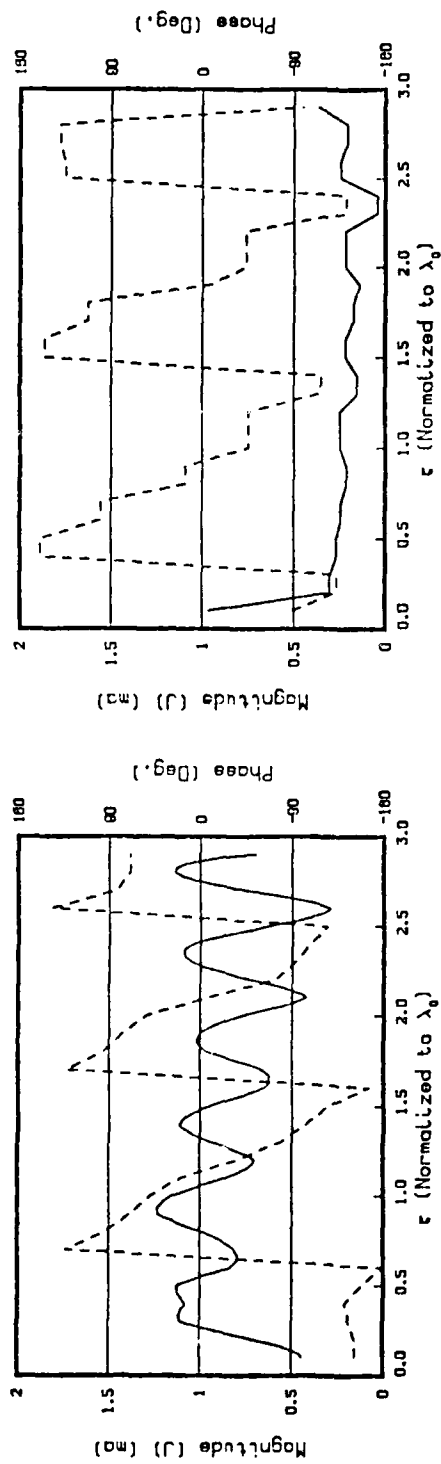
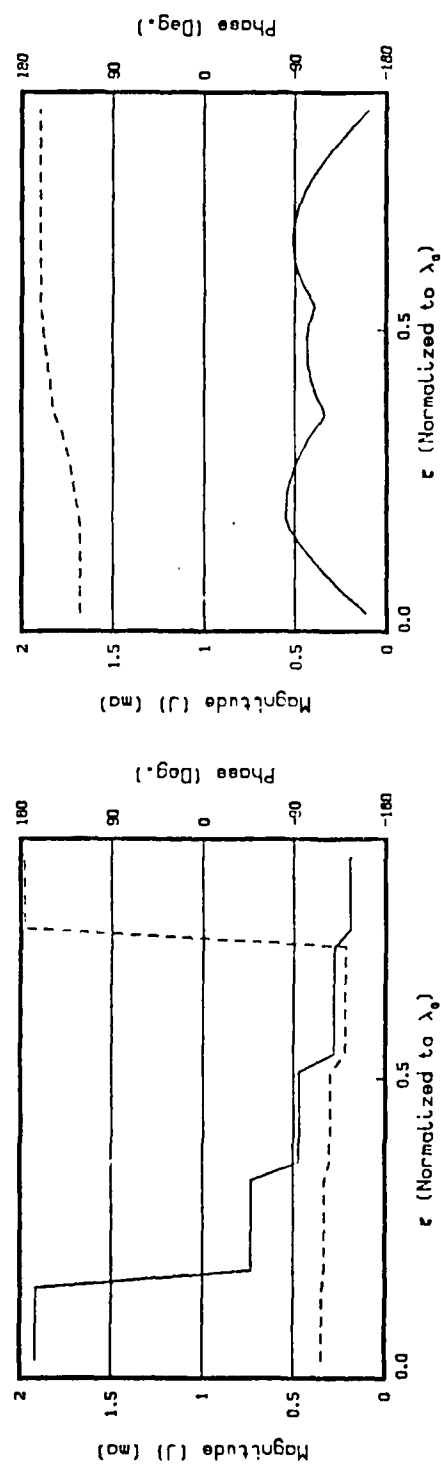


Figure C.33 Modeled Currents When Substrate Thickness = $.025\lambda_0$.

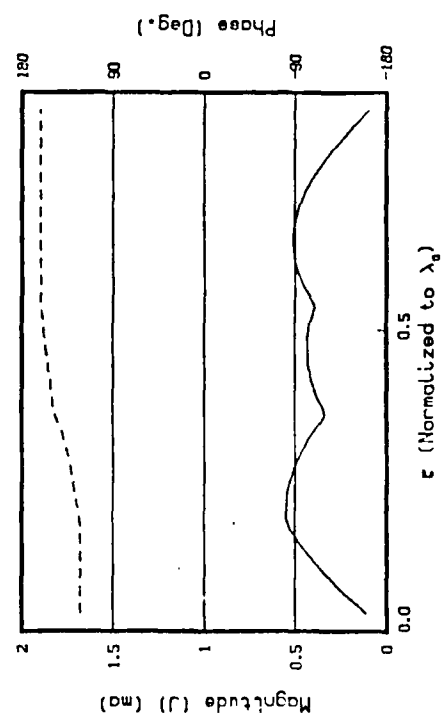


(a) JTRA Current Distributions on CUT AA

(b) JRAD Current Distributions on CUT AA

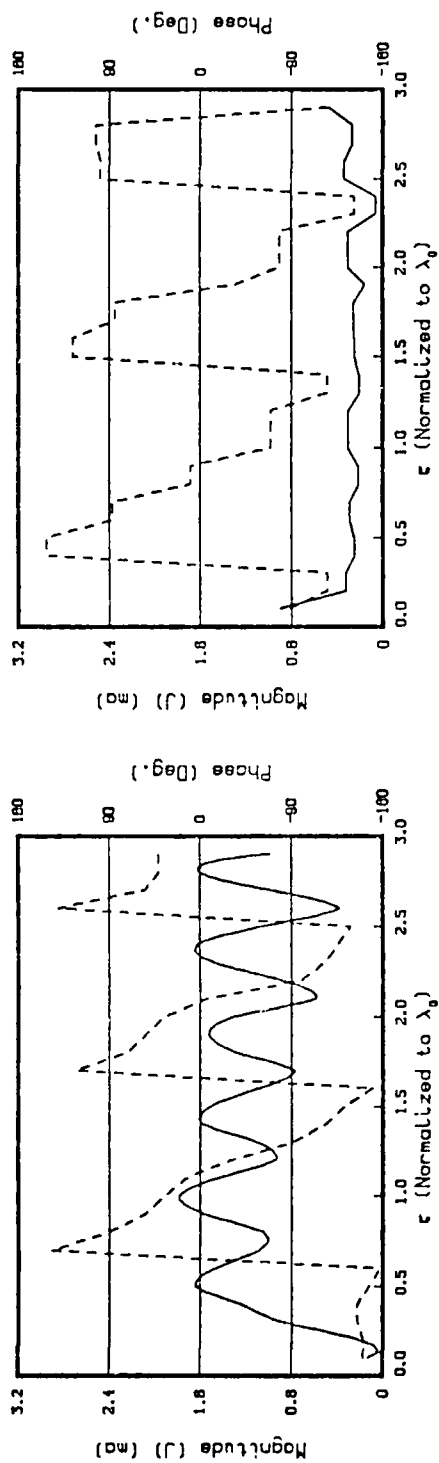


(c) JTRA Current Distributions on CUT BB

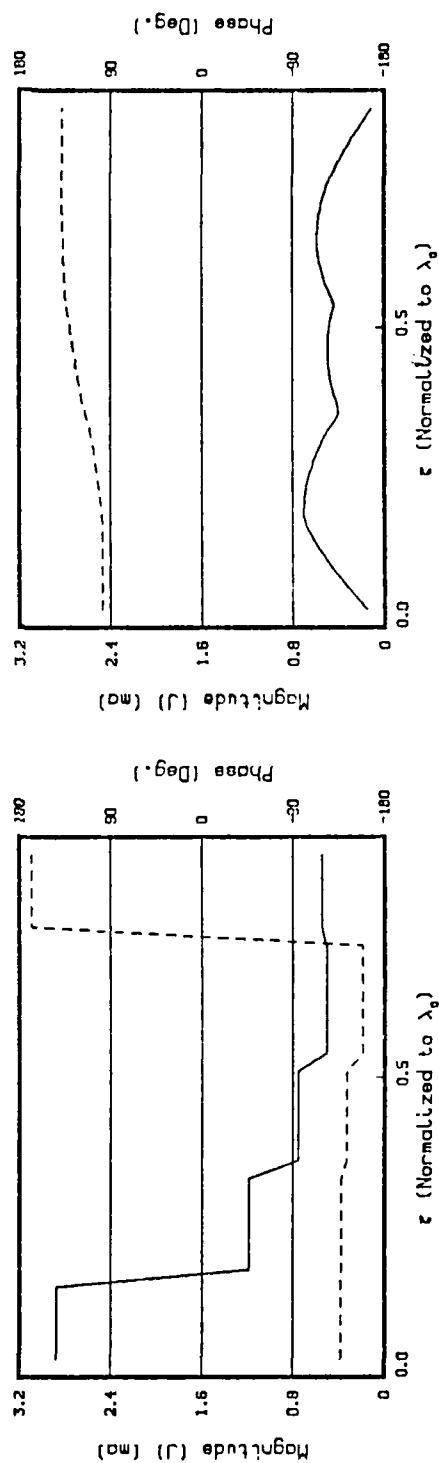


(d) JRAD Current Distributions on CUT BB

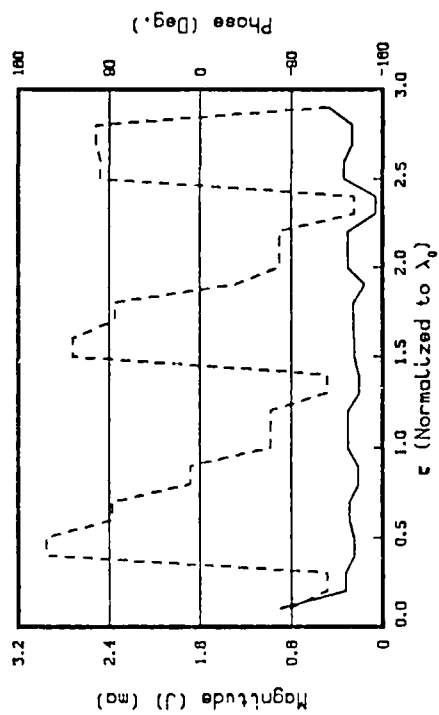
Figure C.34 Modeled Currents When Substrate Thickness = $.030\lambda_0$.



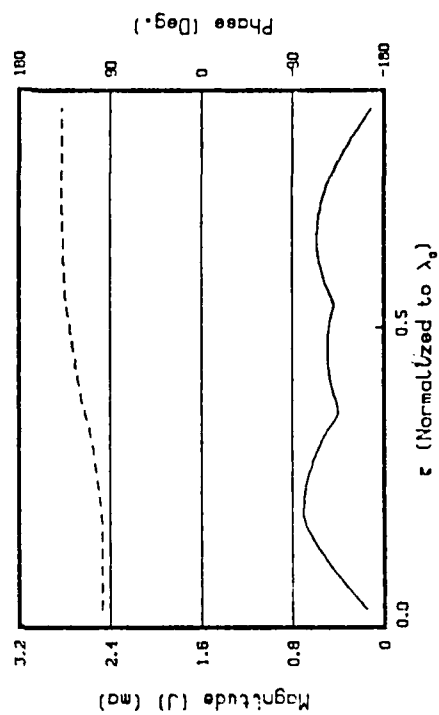
(a) JTRA Current Distributions on CUT AA



(b) JTRA Current Distributions on CUT BB

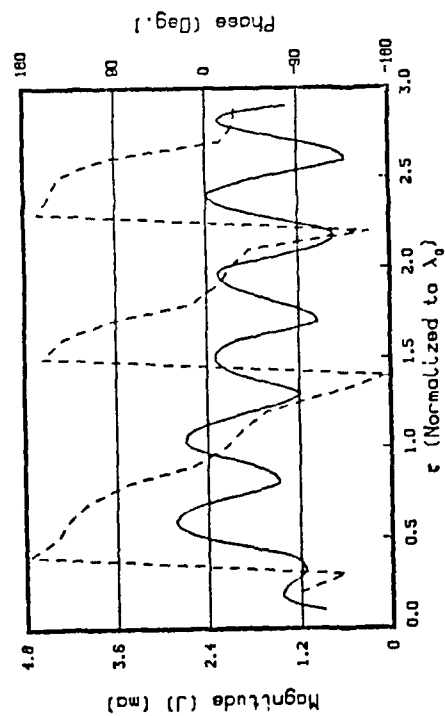


(c) JTRA Current Distributions on CUT AA

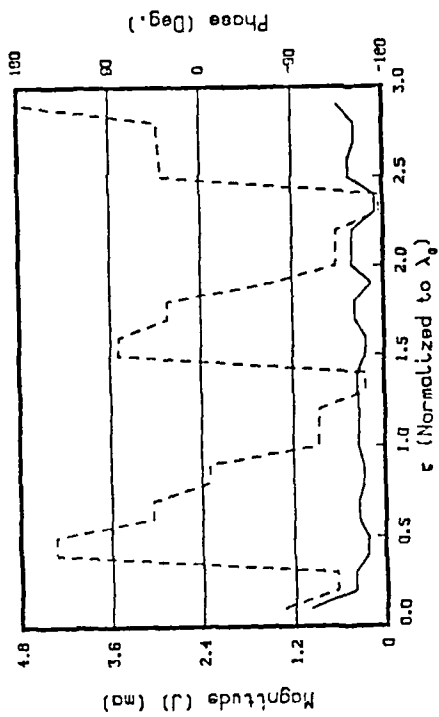


(d) JTRA Current Distributions on CUT BB

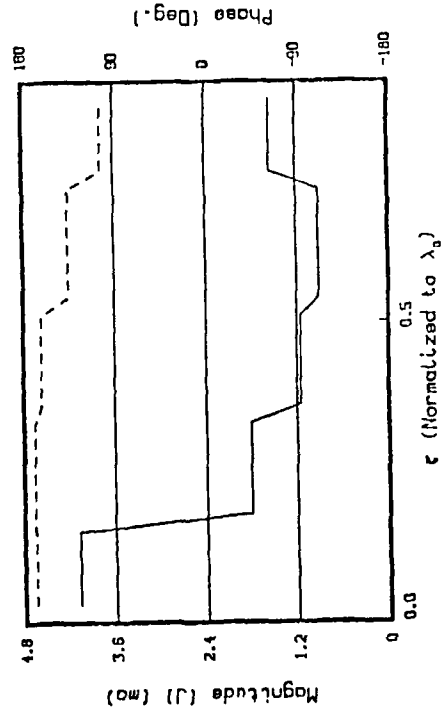
Figure C.35 Modeled Currents When Substrate Thickness = $.040\lambda_0$



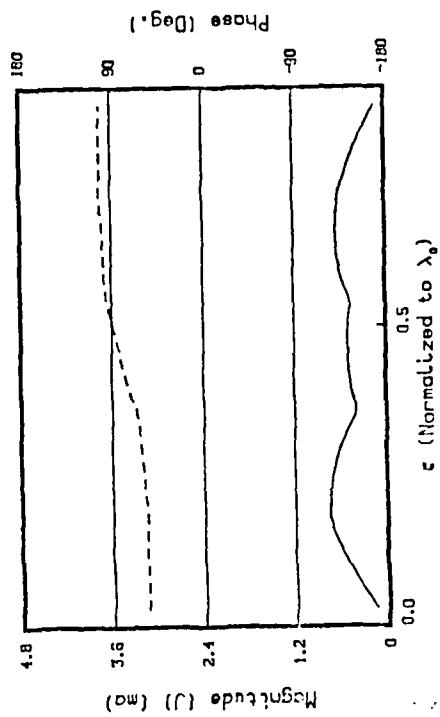
(a) JTRA Current Distributions on CUT RA



(b) JPAD Current Distributions on CUT RA

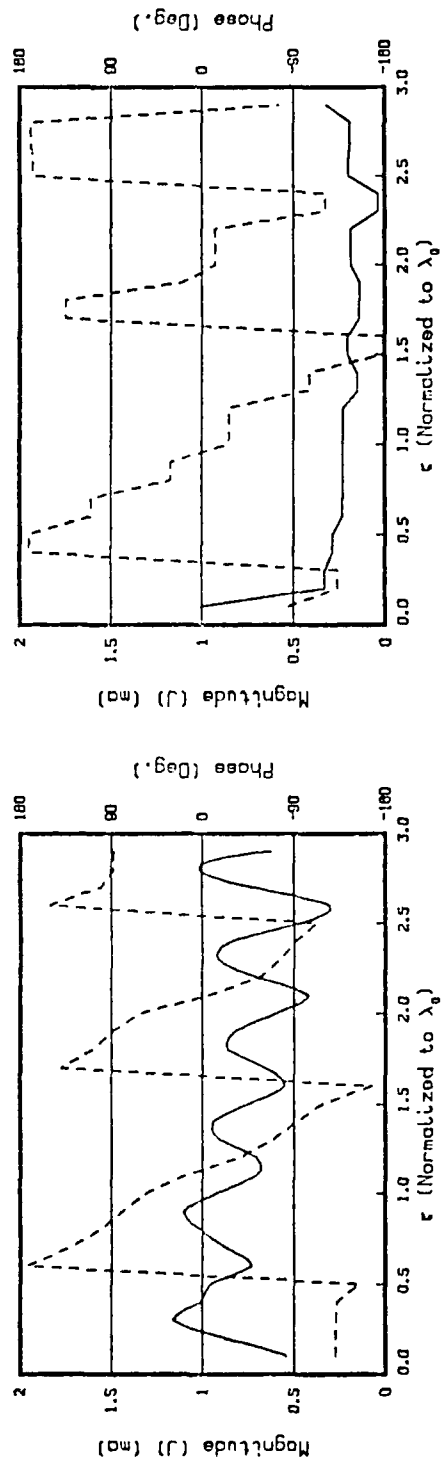


(c) JTRA Current Distributions on CUT BB

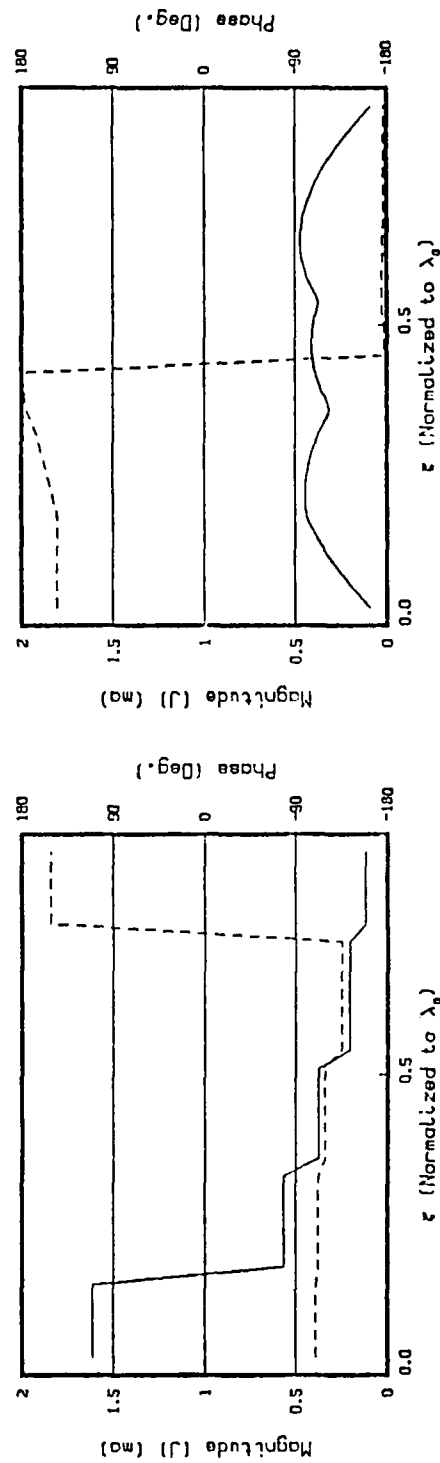


(d) JPAD Current Distributions on CUT BB

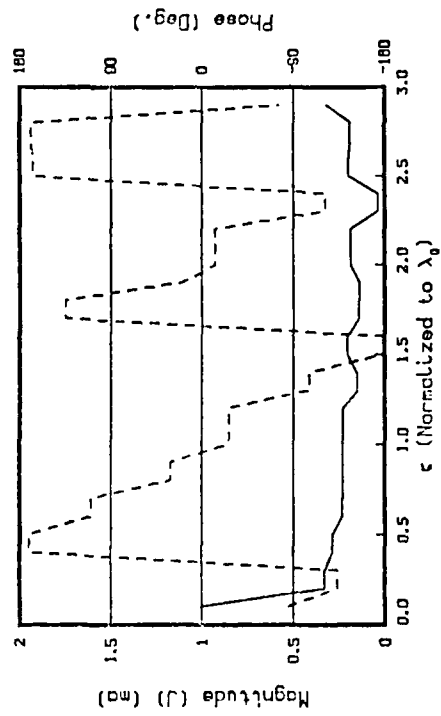
Figure C.36 Modeled Currents When Substrate Thickness = $.050\lambda_0$.



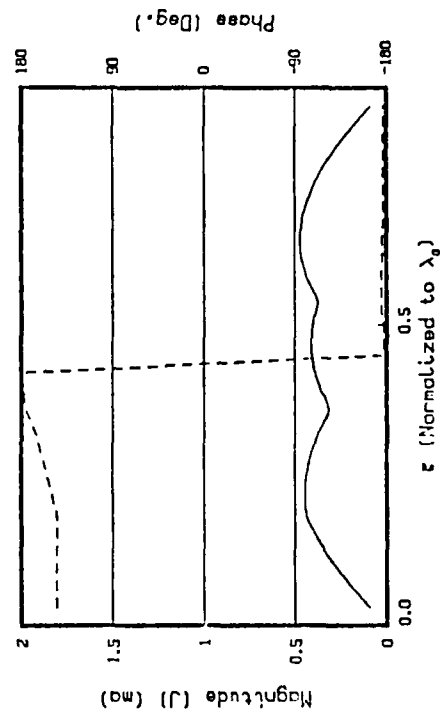
(a) JTRA Current Distributions on CUT AA



(c) JTRA Current Distributions on CUT BB

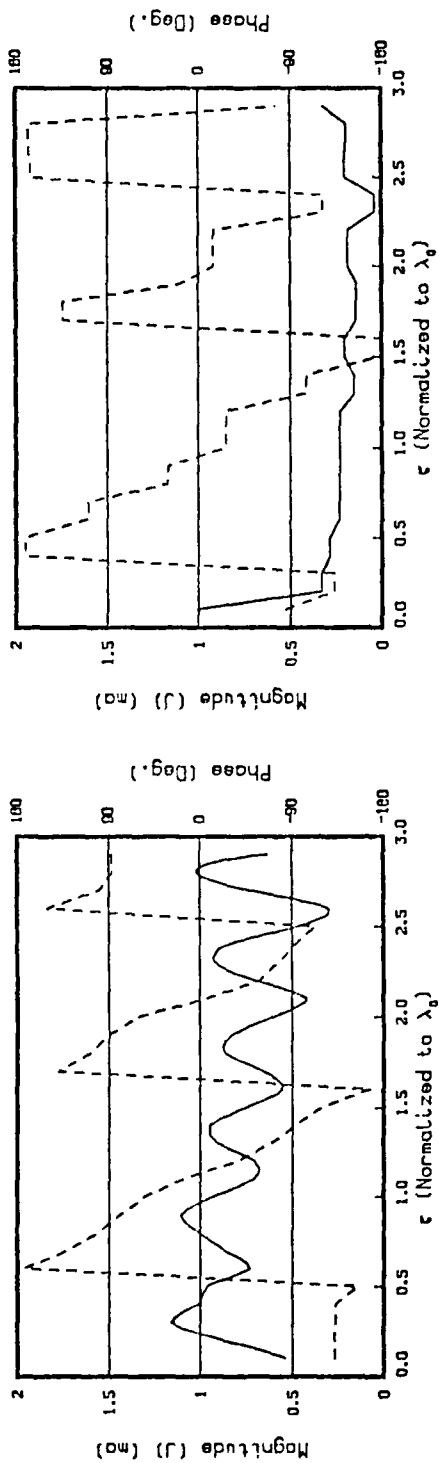


(b) JRAD Current Distributions on CUT AA

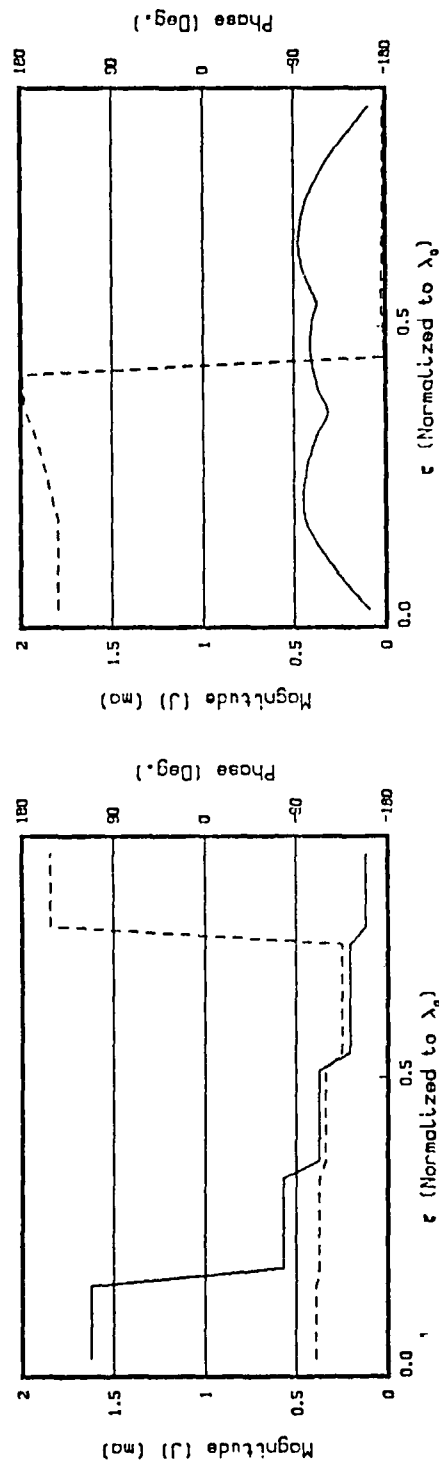


(d) JRAD Current Distributions on CUT BB

Figure C.37 Modeled Currents When Substrate Relative Dielectric Constant $\epsilon_r = 3.5$.

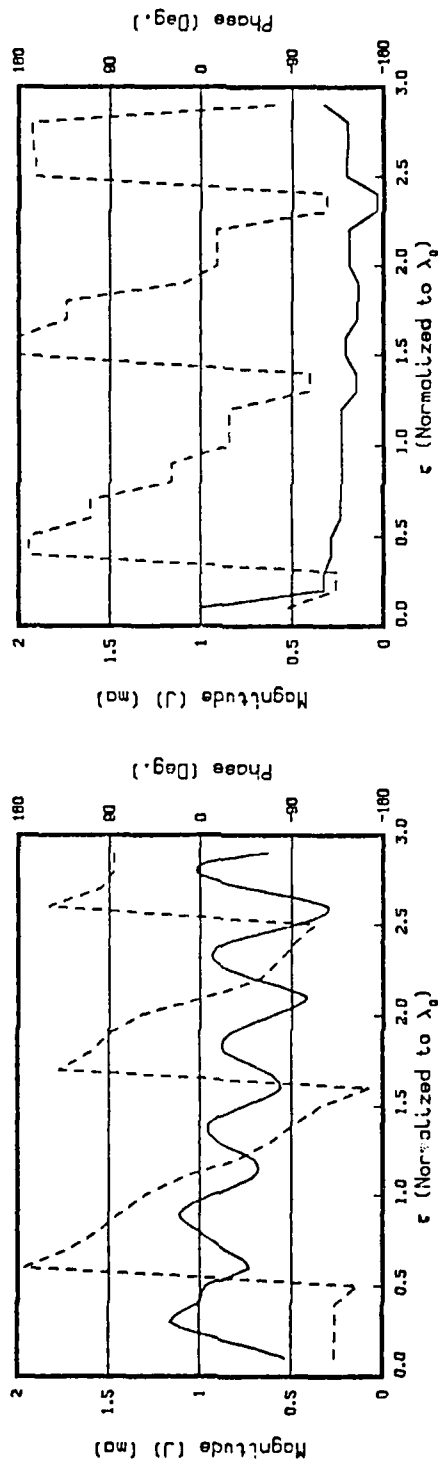


(b) JRAQ Current Distributions on CUT AA

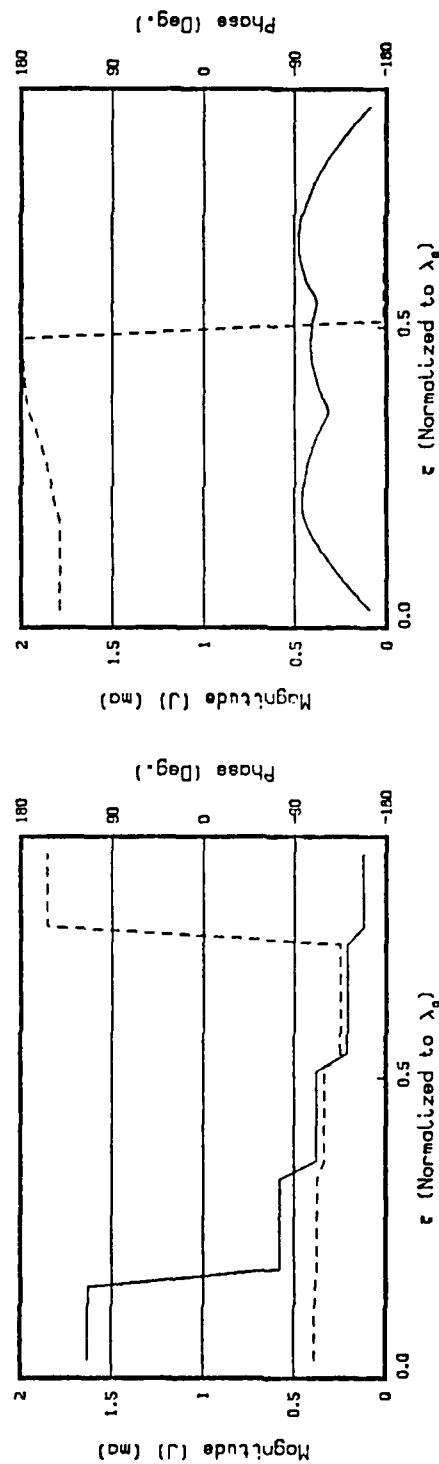


(d) JRAQ Current Distributions on CUT BB

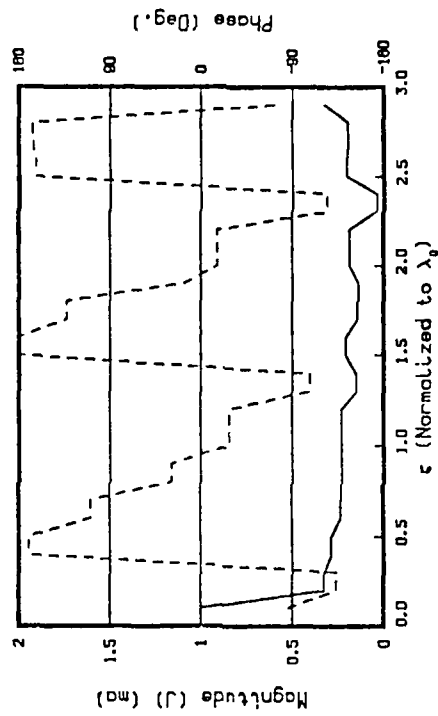
Figure C.38 Modeled Currents When Substrate Relative Dielectric Constant $\epsilon_r = 6.0$.



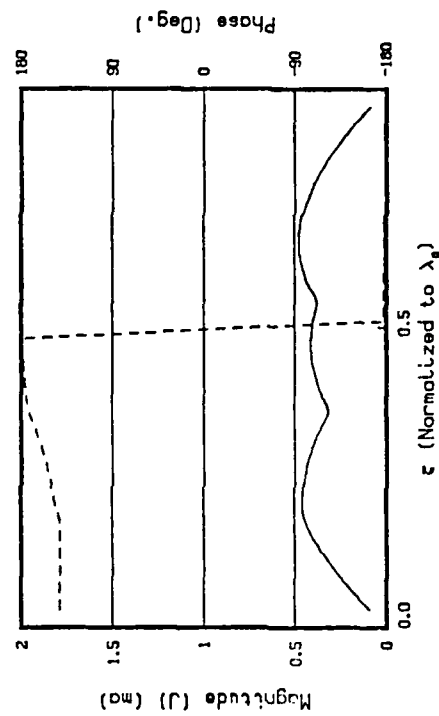
(a) JTRA Current Distributions on CUT AA



(c) JTRA Current Distributions on CUT BB



(b) JRAD Current Distributions on CUT AA



(d) JRAD Current Distributions on CUT BB

Figure C.39 Modeled Currents When Substrate Relative Dielectric Constant $\epsilon_r = 10.5$.

LIST OF REFERENCES

1. Janaswamy, R., "An Accurate Moment Method Model for the Linear Tapered Slot Antenna," paper submitted for publication, July 1988.
2. Stutzman, W. L., and Thiele, G. A., Antenna Theory and Design, Chapter 7, John Wiley & Sons, Inc., 1981.
3. Harrington, R. F., Field Computation by Moment Methods, Chapter 1, Krieger Inc., 1968.
4. Kollberg, E. L., and others, "New Results on Tapered Slot Endfire Antennas or Dielectric Substrates," paper presented at IEEE International Conference on Infrared and Millimeter Waves, 8th, Miami, Florida, December 1983.
5. Janaswamy, R., and Schaubert, D. H., "Analysis of the Tapered Slot Antenna," IEEE Transactions on Antennas and Propagation, V. AP-35, No. 9, pp. 1058-1065, September 1987.
6. Sharma, A. K., Wilson, R. M., and Rosen, A., "An Experimental Investigation of Millimeter-wave Fin Antennas," RCA Laboratories, Princeton, New Jersey, 1985.
7. Thungren, T., Kollberg, E. L., and Yngvesson, K. S., "Vivaldi Antennas for Single Beam Integrated Receivers," presented at 12th European Microwave Conference, Helsinki, Finland, 1982.

INITIAL DISTRIBUTION LIST

- | | | |
|----|---|---|
| 1. | Defense Technical Information Center
Cameron Station
Alexandria, Virginia 22304-6145 | 2 |
| 2. | Library, Code 0142
Naval Postgraduate School
Monterey, California 93943-5002 | 2 |
| 3. | Professor R. Janaswamy, Code 62RJ
Department of Electrical and Computer Engineering
Naval Postgraduate School
Monterey, California 93943 | 4 |
| 4. | Professor M. A. Morgan, Code 62MW
Department of Electrical and Computer Engineering
Naval Postgraduate School
Monterey, California 93943 | 1 |
| 5. | Chairman, Code 62
Department of Electrical and Computer Engineering
Naval Postgraduate School
Monterey, California 93943 | 1 |
| 6. | Thomas P. Kelly
11 Duval Court
Wilmington, Delaware 19808 | 2 |
| 7. | Professor Daniel H. Schaubert
Department of Electrical and Computer Engineering
University of Massachusetts
Amhurst, Massachusetts 01003 | 1 |
| 8. | Professor K. S. Yngvesson
Department of Electrical and Computer Engineering
University of Massachusetts
Amhurst, Massachusetts 01003 | 1 |
| 9. | J. B. L. Rao
Building #47, Room 202
Naval Research Laboratory
Washington, D.C. 20375 | 1 |